Numerical nonlinear analysis of alternate-bar formation under super-resonant conditions

MSc. Thesis

W. (Wilbert) Verbruggen

May 2012

Front page: Aerial view over alternate bars in the Tokachi River, Japan.

Note: This manuscript is designed for double sided full-colour printing

Numerical nonlinear analysis of alternate-bar formation under super-resonant conditions

THESIS

Submitted in partial fulfilment of the
requirements for the Degree of

MASTER OF SCIENCE

In

HYDRAULIC ENGINEERING, track River Engineering
Faculty of Civil Engineering and Geosciences
Delft University of Technology

by

Wilbert Verbruggen
w.verbruggen@student.tudelft.nl
1304305

Graduation Committee:
Prof. Dr. Ir. H.J. de Vriend (Delft University of Technology, Deltares)
Dr. Ir. E. Mosselman (Delft University of Technology, Deltares)
Dr. Ir. C.J. Sloff (Delft University of Technology, Deltares)
Dr. Ir. G. Zolezzi (University of Trento)
Dr. Ir. R.J. Labeur (Delft University of Technology)

May 2012

Delft University of Technology
P.O. Box 5048,
2600 GA, Delft
The Netherlands

Deltares
P.O. Box 177
2600 MH, Delft
The Netherlands

Abstract

Local geometrical perturbations in alluvial channels can generate a pattern of alternate bars. Each bar is accompanied by a pool at the other side of the channel. This pool can decrease the strength of the bank, which can result in bank failure. The bars also cause hindrance to navigation and can block a water intake, if a bar is deposited in front of an irrigation canal. Furthermore, non-migrating alternate bars are considered to be a possible cause of meandering. Previous linear analyses and laboratory experiments showed that these bars arise downstream of perturbations in the relatively narrow and deep channels corresponding to sub-resonant conditions, but both upstream and downstream of perturbations in the relatively wide and shallow channels corresponding to super-resonant conditions. Previous numerical computations reproduced alternate bars under sub-resonant conditions, but failed to do so under super-resonant conditions until the recent 2D depth-averaged computations by Van der Meer et al. (2011) using Delft3D.

This study is an advance on the modelling work of van der Meer et al. and has the objective to assess to what extent the numerical results agree with linear theory and experimental observations and to investigate the development of bars upstream of a bend under super-resonant conditions.
Few experiments of bar development under super-resonant conditions are available in the literature. Zolezzi et al. (2005) conducted three super-resonant experiments in a U-curved flume. Downstream of the bend, the numerical model and experimental observations clearly matched. The numerical model, however, was not able to reproduce the development of non-migrating alternate bars upstream of the bend at the experimental conditions. It appeared that the point of resonance was over-predicted by the numerical model, so the (in reality) super-resonant experiment was still sub-resonant in the numerical model. For larger width-to-depth ratios the numerical model showed that it was able to develop bars upstream of the bend. Also the observed wave lengths and bed-topography spectra complied with the literature. The numerical model matched prediction of linear theory only for small-amplitude alternate bars.

The numerical simulations were unstable for realistic values of the horizontal eddy viscosity ($O(10^{-5}\ m^2/s)$ for small-scale models). The latter was therefore increased to stabilize the simulations. This increase was the cause of overpredicting the point of resonance by the numerical model. It appeared that the resonance half-width-to-depth ratio was about 50% larger for the high viscosity than in the case of a low horizontal eddy viscosity. For the bedload transport procedure Delft3D offers two options, the ‘upwind’ procedure and the ‘central’ procedure. The former introduces numerical diffusion, whereas the latter is less stable. The shortening of bars for large width-to-depth ratios, as observed by Van der Meer et al. (2011), is probably the result of numerical diffusion. The ‘upwind’ procedure causes sediment deposits and scour to be concentrated near the banks, because the higher modes (for example the central mode) within the alternate-bar spectrum were damped. Therefore ‘upwind’ bar peaks are higher and can become inactive, because these bars run dry before they are fully developed and consequently have a smaller wave length.

The alternate-bar pattern upstream of the bend under super-resonant conditions was found to develop from downstream to upstream, in accordance with linear theory, only if no perturbation

was applied at the upstream boundary. A development from upstream to downstream dominated in case of a perturbed upstream boundary. The computed alternate bars migrated invariably downstream, under both super-resonant and sub-resonant conditions. I ascribe this to nonlinear effects, since the bars did migrate upstream under super-resonant conditions, in accordance with linear theory, as long as their amplitudes were very small. The analytical model complies with the behaviour of small-amplitude bars in the numerical model, but fails to predict the behaviour of large-amplitude bars in the numerical model due to non-linear effects.

This study has shown that alternate-bar formation cannot be solely understood from linear equations. It seems therefore recommendable to investigate the contribution of non-linear effects in a more quantitative way, for example through outputting the contribution of each non-linear term in the equation for flow and sediment transport in Delft3D. The strength of gravitational pull on transverse slopes has large consequences on the direction of sediment transport and therefore also on alternate-bar properties. Mismatches in bar amplitude and the bed topography in bends are probably caused by errors in the prediction of transverse slope effects. For these reasons it is recommendable to improve the prediction of transverse bed-slope effects. This can be established by applying the particle-approach of (Nabi, 2012).

Preface

This document constitutes the final thesis report to accomplish the Master of Science degree in Hydraulic Engineering at Delft University of Technology, Faculty of Civil Engineering and Geosciences. It is the result of a study I carried out from September 2011 till May 2012. The subject of the study was to investigate the numerical modelling of alternate bars. The study was carried out under the supervision of Erik Mosselman and Kees Sloff at Deltares.

First of all, I would like to thank Erik Mosselman and Kees Sloff for their support and willingness to enhance my research. I want to thank Erik mainly for the overall support and discussions we had about my findings and Kees for his support to help me with applying Delft3D (the numerical model I used). I also want to thank Guido Zolezzi for his support during the skype-meetings we had and for the experimental details he supplied. I furthermore would like to thank Huib de Vriend, my graduation professor, for his ideas and enthusiasm during the meetings we had and Robert-Jan Labeur for the constructive comments.

Secondly, I would like to thank Deltares for supplying me a workspace, so that experts were within a short distance. Besides my supervisors I want to thank Dirk-Jan Walstra and Bert Jagers for their help on specific problems. I would also like to thank my fellow graduates at Deltares. During my stay at Deltares I met a lot of graduates from different countries. During the lunch and coffee breaks we helped and motivated each other. Besides the advantages for my research I also want to thank them for the pleasant time it created.

Thirdly, I would like to thank my family and friends for their interest and encouragements. Special thanks go out to my parents, who made my Master of Science degree financially possible. Lastly, I would like to thank my fiancé for her support and for checking my report on the use of English.

I hope you will enjoy reading it!

Wilbert Verbruggen
Delft, May 2012

Table of contents

List of Figures

List of Tables

List of symbols

A	Spiral flow coefficient	[-]
A_{sh}	Calibration coefficient for the Koch and Flokstra formula	[-]
$A^{(m,n)}$	Area of computational cell at location (m,n)	[m^2]
B	Channel width	[m^1]
b	Degree of non-linearity in dependence of sediment transport capacity on flow velocity	[-]
b_1	Non-linear bar coefficient	[-]
b_2	Non-Linear bar coefficient	[-]
C	Chézy coefficient	[$m^{1/2}s^{-1}$]
$\tilde{C}$	Dimensionless Chézy coefficient	[-]
C_D	Degree of non-linearity in dependence of roughness on water depth	[-]
C_T	Degree of non-linearity in dependence of roughness on Shields parameter	[-]
c_f	Roughness coefficient	[-]
$c_{f,0}$	Zero-order dimensionless roughness coefficient	[-]
D	Water depth	[m^1]
DPS	Procedure in Delft3D to specify the bottom depth in the cell centre	[-]
DPU	Procedure in Delft3D to specify the bottom depth in the cell face	[-]
$\tilde{D}$	Dimensionless water depth (D/D_0)	[-]
D_0	Zero-order water depth	[m^1]
D_{50}	Median grain size	[m^1]
d_s	Relative roughness (D_{50}/D)	[-]
E_s	Calibration coefficient for spiral flow in Delft3D	[-]
F	Froude number	[-]
F_0	Zero-order Froude number	[-]
$F(u)$	Fourier Transform at frequency variable u	[-]
$f(\theta)$	Shape factor of grains	[-]
f_{Morfac}	Morphological acceleration factor	[-]
f_s	Sample frequency	[-]
g	Gravitational acceleration	[m^1s^{-2}]
H_B	Bar height (difference between maxima in cross-section with lowest point)	[m^1]

H_{BM}	Bar height (difference between maxima in the entire bar unit)	[m^1]
h	Bar amplitude	[m^1]
h_{eq}	Equilibrium bar amplitude	[m^1]
h_0	Initially imposed bar amplitude	[m^1]
i	Longitudinal slope	[-]
k	Dimensional wavenumber in the longitudinal direction	[m^{-1}]
k_r	Dimensional real wavenumber ($2\pi/L_L$)	[m^{-1}]
k_s	Nikuradse roughness height	[m^1]
$\tilde{k}_s$	Dimensionless Nikuradse roughness height (k_s/D)	[-]
k_w	Dimensional transverse wavenumber	[m^{-1}]
L_D	Damping length	[m^1]
L_L	Longitudinal bar wave length	[m^1]
L_T	Transverse bar wave length	[m^1]
L_{eq}	Equilibrium longitudinal bar wave length	[m^1]
m	Harmonic mode	[-]
N	Number of samples	[-]
Q	Discharge	[m^3s^{-1}]
Q_p	Perturbed discharge	[m^3s^{-1}]
$Q_{p,cell}$	Perturbed discharge per cell	[m^3s^{-1}]
Re	Reynolds number	[-]
s	Bed-load transport per unit width	[$m^3s^{-1}m^{-1}$]
$\hat{s}$	Amplitude of bed-load transport per m width	[$m^3s^{-1}m^{-1}$]
s_x	Bed-load transport in x-direction	[m^3s^{-1}]
s_{x0}	Zero-order bed-load transport per unit width in x-direction	[m^3s^{-1}]
s_{x1}	Harmonic part of the bed-load transport per unit width in x-direction	[m^3s^{-1}]
$s_{x,0}$	Bed-load transport per unit width in x-direction at t=0	[m^3s^{-1}]
s_y	Bed-load transport per unit width in y-direction	[m^3s^{-1}]
s_{y1}	Harmonic part of the bed-load transport per unit width in y-direction	[m^3s^{-1}]
$s_{y,0}$	Bed-load transport per unit width in y-direction at t=0	[m^3s^{-1}]
$S_{b,uu}^{(m,n)}$	Computed bed-load sediment transport in u-direction, held at u-point of the computational cell at location (m,n)	[$kg^1s^{-1}m^{-1}$]
$S_{b,vv}^{(m,n)}$	Computed bed-load sediment transport in v-direction, held at v-	[$kg^1s^{-1}m^{-1}$]

	point of the computational cell at location (m,n)	
$S_{b,v}^{(m,n)}$	Computed bed-load sediment transport in v-direction, held at centre of the computational cell at location (m,n)	[$kg^1s^{-1}m^{-1}$]
$S_{b,u}^{(m,n)}$	Computed bed-load sediment transport in u-direction, held at centre of the computational cell at location (m,n)	[$kg^1s^{-1}m^{-1}$]
t	Time	[s^1]
u	Velocity in the longitudinal direction	[m^1s^{-1}]
u'	Perturbation of velocity in the longitudinal direction	[m^1s^{-1}]
u_f	Resolution variable in the longitudinal direction	[-]
u_0	Zero-order velocity in the longitudinal direction	[m^1s^{-1}]
U	Length of frequency variable vector	[-]
v	Velocity in transverse direction	[m^1s^{-1}]
v_f	Resolution variable in the transverse direction	[-]
WL	Water level boundary condition	[m^1]
x	longitudinal coordinate	[m^1]
y	transverse coordinate	[m^1]
z_b	Bed level	[m^1]
$\hat{z}_b$	Amplitude of bed level perturbation	[m^1]
$z_b^{'}$	Perturbation of bed level	[m^1]
$z_{b,0}$	Zero-order bed level	[m^1]
α	Calibration coefficient for the Meyer-Peter Müller formula	[-]
α_{bs}	Streamwise bed gradient factor for bed-load transport	[-]
β	Half-width-to-depth ratio (B/(2D))	[-]
β_c	Critical half-width-to-depth ratio	[-]
β_{res}	Resonant half-width-to-depth ratio	[-]
Δ	Relative density ($(\rho_s - \rho_w)/\rho_w$)	[kg^1m^{-2}]
$\Delta_{SED}^{(m,n)}$	Change in quantity of bottom sediment at location (m,n)	[kg^1m^{-2}]
Δt	Computational time step	[s^1]
Δx	Grid size in x-direction	[m^1]
Δy	Grid size in y-direction	[m^1]
δ_{upw}	Phase lag between bed topography and bed-load transport, due to upwinding	[rad^1]
δ_1	Phase lag between bed topography and bed-load transport in the longitudinal direction	[rad^1]
δ_2	Phase lag between bed topography and bed-load transport in lateral the	[rad^1]

ε	Perturbation	[-]
φ_s	Direction of sediment transport (including transverse bed slope effect)	[rad^1]
φ_T	Direction of sediment transport (excluding transverse bed slope effect)	[rad^1]
γ	Coefficient in Struiksma model in dependency of the flume width and the adaptation length for flow	[-]
λ	Dimensionless longitudinal wavenumber ($\pi B / L_L$)	[-]
λ_c	Dimensionless wavenumber corresponding with critical conditions	[-]
λ_s	Adaptation length for morphology	[m^1]
λ_w	Adaptation length for flow	[m^1]
λ_1	Dimensionless wavenumber perturbation	[-]
υ_H	Horizontal eddy viscosity	[m^{2}s^{-1}]
μ	Ripple factor	[-]
ρ_s	Density of solids	[kg^{1}m^{-3}]
ρ_w	Density of water	[kg^{1}m^{-3}]
θ	Shields number	[-]
θ_{cr}	Critical Shields number	[-]
θ_0	Zero-order Shields number	[-]
Φ	Dimensionless transport parameter $s / \left(D_{50} \sqrt{\Delta g D_{50}} \right)$	[-]
Φ_D	Degree of non-linearity in dependence of sediment transport on water depth	[-]
Φ_T	Degree of non-linearity in dependence of sediment transport on Shields parameter	[-]
ω	Angular frequency	[rad^{1}s^{-1}]
Ω	Amplification rate	[s^{-1}]

1 Introduction

1.1 Context

Alluvial river beds display different kinds of bed forms. One of these possible bed forms is called 'alternate bars'. Alternate bars have adopted their name from the fact that the bar and pool occur alternately at the left and the right bank, see Figure 1-1.
In an alternate-bar pattern, a bar is always accompanied with a pool on the other side of the channel. The pool depth can become large and reduces the strength of the bank against shear failure, which can lead to bank failure as often observed (Ikeda, 1982, Fujita and Muramoto, 1985). As shown in Figure 1-1, during certain discharges the alternate bar can become dry, or just submerged. This can be a hindrance for navigation. A non-migrating bar can also be an obstacle for water intake if the bar is located in front of an irrigation canal. Non-migrating bars are also a possible explanation for the start of meandering (Olesen, 1983, Blondeaux and Seminara, 1985, Rhoads and Welford, 1991). For these reasons, it is important to gather knowledge about alternate bars and how they can be modelled.

Figure 1-1: Alternate bars in the Tokachi River, Japan

In the past decades, several scientists have tried to explain the processes that are responsible for the formation of non-migrating alternate bars. In the 1960s, it was suspected that the occurrence of alternate bars can be explained by a stability analysis of the mathematical equations for flow and sediment transport. In 1985, two important linear theories were published, which are the base for the present theories. One of these theories, Blondeaux and Seminara (1985), assumes that migrating alternate bars in a straight channel, without geometrical perturbations, become non-migrating under resonant conditions. Resonance in this respect is related to the condition (characterised by the half-width-to-depth ratio, β) in which the damping in space is zero. In that condition, the bars are non-amplifying and non-migrating. They associated the occurrence of non-migrating alternate

bars with the occurrence of maximal bend amplification. The other classical linear theory was presented by Struiksma et al. (1985). That paper assumes that non-migrating alternate bars are generated by a geometrical perturbation, for instance a groyne, change in channel curvature, etc.
Subsequent theoretical research of Zolezzi and Seminara (2001a) points out that, in deep or narrow rivers, non-migrating alternate bars are found downstream of the geometrical perturbation. They introduced the term sub-resonant for this condition, because β in that case is lower than β_{res}. For shallow or wide rivers ($\beta > \beta_{res}$, thus in super-resonance conditions), the expectation was that only upstream of the bend non-migrating alternate bars would occur.
Laboratory experiments by Zolezzi et al. (2005) show that, indeed, only downstream of the bend non-migrating alternate bars occur under sub-resonant conditions, but under super-resonant conditions the non-migrating alternate bars appear both upstream and downstream.

Van der Meer et al. (2011)
Previous numerical computations reproduced alternate bars under sub-resonant conditions, but failed to do so under super-resonant conditions until the recent 2D depth-averaged computations by Van der Meer et al. (2011) using Delft3D. The domain of the model of van der Meer et al. (2011) was made on laboratory scale. The width of the modelled flume was 0.6 m and the length of the flume 32 m. The domain consists of a bend and two straight parts, 12 m upstream and 12 m downstream of the bend. The equilibrium bed topography of a sub- and super-resonant simulation can be seen in Figure 1-2.

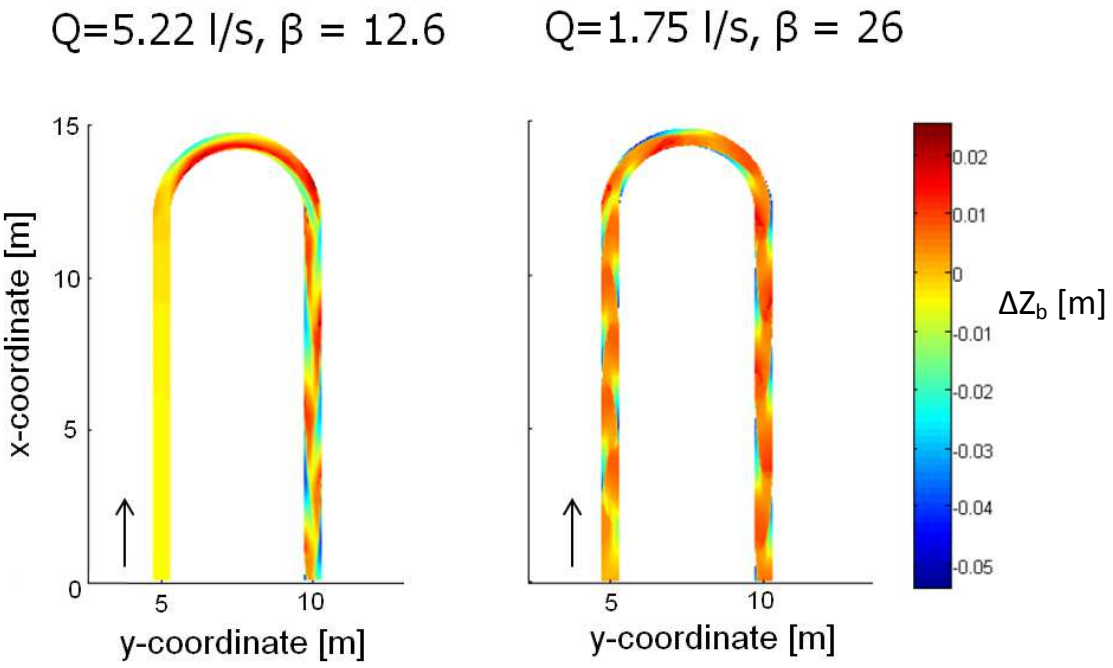

Figure 1-2: Bed topography (sedimentation and erosion plots) under sub-resonant (left) and super-resonant conditions (Van der Meer et al., 2011), edited

Van der Meer et al. (2011) observed that the point of resonance in the numerical model ($\beta_{res} \approx 15$) is larger than predicted by linear theory $\beta_{res} \approx 10$. Another mismatch between the numerical and analytical model was the wave length of alternate bars for $\beta > 13$. The numerical model predicted them to be much shorter than linear theory did.

1.2 Problem description

Despite all the scientific work in the past decades, a lot of questions arise in relation to alternate bars. Those questions can mainly be separated into two groups:

- *Uncertainty in relation to the differences between the solutions of the numerical model and the analytical solution:*
  As explained in section 1.1, the model of van der Meer et al. (2011) predicted β_{res} to be significantly larger than linear theory. The wave length in the numerical model was significantly shorter than predicted by linear theory for $\beta > 13$. Van der Meer et al. suggested that numerical diffusion could have contributed to the mismatch. Research on the influence of numerical diffusion and other numerical parameters on alternate-bar properties had not been carried out.

- *Uncertainty in relation to the development of upstream (upstream of the bend) alternate bars:*
  Zolezzi and Seminara (2001a) pointed out that upstream development of alternate bars is possible under super-resonant conditions. This was explained by the fact that only in these conditions it is possible for sufficiently-long small-amplitude free bars to travel in the upstream direction. Although the numerical simulations of Van der Meer et al. (2011) show alternate bars upstream of the bend, it is unclear how these bars are build up and how the bend influences the development of bars.

1.3 Objectives

The main objectives of this research are:

- Improving and validating the numerical model of van der Meer et al. (2011) (chapter 4).
- Studying the effects of some typical numerical factors (typical schemes for the morphological updating procedure, horizontal eddy viscosity, grid resolution) on alternate-bar characteristics (chapter 5).
- Acquiring a better understanding of the development process of alternate bars, upstream of a bend under super-resonant conditions (chapter 6).

1.4 Research outline

For those who are not fully into the subject of alternate bars, a brief overview of the necessary theory is given in chapter 2. Below I will provide a brief overview of chapters 3 to 6 of this report. Each chapter has the same structure, first the objective of the chapter is given, secondly the methodology to fulfil the objective is presented, and finally the results are given and discussed.

To be able to validate the numerical model, the analytical model, provided by the literature, is adjusted such that it uses the same roughness definition, transport formula, etc. (see chapter 3).
The numerical model is based on 2D equations and uses Delft3D, see chapter 4. The validation of the numerical model is based on experimental data of Zolezzi et al. (2005), comparison with linear theory and general observations in the literature. The validation shows that the model is able to reproduce alternate-bar patterns, but quantitatively some mismatches with experiments and theory are observed, especially for the prediction of the point of resonance, like observed by Van der Meer et al. (2011).
Some numerical parameters had been supposed to have a large influence on the quantitative prediction of the model. This numerical analysis can be found in chapter 5. It appears that especially the horizontal eddy viscosity has a large influence on the point of resonance and that numerical diffusion causes bars to be shorter for large width-to-depth ratios.
In chapter 6, the development of bars upstream of a bend is discussed. Analysis shows that alternate bars, located upstream of the bend, are build up from downstream to upstream, in accordance with linear theory. If a perturbed discharge is used at the inflow boundary, the pattern is build up from upstream to downstream. The disturbance-driven pattern development is therefore supposed to be dominant over the bend-driven pattern development. Another observation is that all individual bars invariably migrate in the downstream direction, contrary to the prediction of linear theory. I show that this can be explained by non-linear effects.

2 Background theory

This chapter gives a brief overview of the background theory for this research. First, the generally used classification of bars is discussed. Then a brief summary is provided of some available models to predict alternate-bar properties. A more complete elaboration can be found in Appendix A.

2.1 Bar classification

In this section I discuss the bar classifications that are used in this research.

Bar modes

In this research I have schematized bars as sinusoidal bed topographies. In the lateral direction (perpendicular to the flow) the bar can be represented with the following expression:

$$z_b = h \cdot \cos(k_w y) \quad (2\text{-}1)$$

$$k_w = \frac{m \cdot \pi}{B} \quad (2\text{-}2)$$

Z_b is the bed level, h is the bar amplitude, k_w the lateral wavenumber, y the lateral direction, m the harmonic mode and B the width of the channel. A 'mode one bar', or 'first-mode bar', has a lateral wave length which is twice the channel width. Figure 2-1 shows the bed level variations of a first and second-mode bar. In linear theory an alternate bar is schematized as a first-mode bar, because the bar and pool of the alternate-bar pattern alternate between the river banks. In nature, an alternate bar is a superposition of different modes and does not solely consist of first-mode bars, see section 4.3.2.

Another definition that is used in this research is for example a 1-1 bar mode. The first number represents the longitudinal bar mode and the second number the transverse bar mode. The wave length related to the first mode in the longitudinal direction is defined as the wave length of the alternate-bar pattern. The second longitudinal mode has a wave length that is half the alternate-bar wave length, etc.

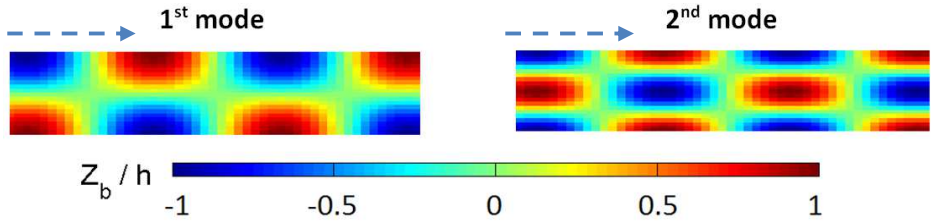

Figure 2-1: Typical planforms of first and second bar modes

Free or forced

This classification is related to the origin of the bar. 'Free' bars spontaneously develop because of an instability of the flow-bed system (Seminara and Tubino, 1989). Bars are called 'forced' when they are caused by a physical disturbance or constraint that may be introduced by obstacles (for example

bridge piers, groynes) or a distributed forcing effect (gradual change in channel curvature). Because the origin of forcing is static, the forced bars will also become static.

Migration

In the literature, the term 'steady bar' is sometimes used to describe a bar that does not migrate. This term, however, is ambiguous, because it can also refer to a bar which does not amplify. Therefore I use the term 'non-migrating' instead of 'steady'.

Non-migrating bars are generally longer than migrating bars. Dimensionless wavenumbers ($\pi*B/L_L$, in which B is the channel width and L_L is the length of the bar) of non-migrating bars under common conditions are in the order of 0.15, whereas the wavenumber of the most-unstable mode (with the largest growth rate) of migrating bars ranges from about 0.40 to 0.50. This means that the wavelength of non-migrating bars is generally about three times as large as the wave length of migrating bars.

Migrating and non-migrating bars might interact. The wave length of the resulting bar pattern might be influenced by the presence of migrating bars. Vanzo et al. (2011) made an effort to investigate this interaction, and discovered that for larger width-to-depth ratios (β), the wave length of the final bar pattern tends towards the wave length of the most-unstable free-bar mode. On the contrary, when the β ratio decreases (narrower, deeper channels), the wavelength of the resulting bar pattern tends to that of the non-migrating bars according to linear theory.

For a long time it was common thought that non-migrating bars were the result of forced circumstances. Crosato et al. (2010) discovered that non-migrating bars can also be the result of morphodynamic instability, like free bars. They mention that these non-migrating bars in unforced experiments were possibly not observed up till now because the growth rates of steady bars are much smaller than those of migrating bars.

Amplification and instability

If the bar amplitude is constant over time, the bar is said to be 'non-amplifying'. In this report I sometimes refer to 'unstable bars', these are bars which are amplifying. The initial flat bed is in that case unstable for these wave lengths. The 'most-unstable' bar refers to the bar with the largest amplification rate. This bar is thought to prevail over other bar modes, because it has a dominant growth rate.

2.2 Physics of bar behaviour

The behaviour of bars can be understood by considering the interaction between the bed topography and the bed-load transport. The bed topography of an ideal harmonic bed topography can be represented with the following expression:

$$z_b = z_{b,0} \cdot e^{\Omega t} \cdot \cos(kx - \omega t) \cdot \cos(\frac{m \cdot \pi}{B} y) \qquad (2\text{-}3)$$

In which $z_{b,0}$ is the bed level at t=0, Ω is the amplification rate [1/s], k is the longitudinal wavenumber ($2\pi/L_L$), ω the angular frequency [rad/s] and m the harmonic mode. The exponential term represents the exponential growth of the bar amplitude, the first cosine factor represents the longitudinal

structure and migration of the bar pattern and the second cosine factor represents the lateral structure of the bar pattern.
The migration rate and amplification rate of the bed topography depends on the phase lag between the bed-load transport and the bed topography. Therefore I need to derive the expression for the bed-load transport. Let us, for simplicity, first only consider the bed-load transport in the longitudinal direction. The longitudinal bed-load transport per unit width is defined as:

$$s_x = s_{x0} + s_{x1}(x,y,t) \tag{2-4}$$

In which s_x is the sediment transport in the longitudinal direction per unit width, s_{x0} the average longitudinal sediment transport per unit width and s_{x1} the space and time dependent longitudinal sediment transport variation per unit width.

In analogy to the expression for z_b, the varying longitudinal sediment transport can be expressed as:

$$s_{x1} = s_{x,0} \cdot e^{\Omega t} \cdot \cos(kx - \omega t - \delta_1) \cdot \cos\left(\frac{m \cdot \pi}{B} y\right) \tag{2-5}$$

In which $s_{x,0}$ is the sediment transport perturbations at t=0 in the longitudinal direction per unit width and δ_1 is the phase lag between the bed-load transport and the bed topography in the longitudinal direction.

Continuity (1D) states that the time derivative of the bed topography is dependent on the spatial derivative of the longitudinal transport:

$$\frac{\delta z_b}{\delta t} + \frac{\delta s_x}{\delta x} = 0 \quad \rightarrow \quad \frac{\delta z_b}{\delta t} = -\frac{\delta s_x}{\delta x} \tag{2-6}$$

$$\rightarrow \quad \frac{\delta z_b}{\delta t} = k \cdot s_{x,0} \cdot e^{\Omega t} \cdot \sin(kx - \omega t - \delta_1) \cdot \cos\left(\frac{m \cdot \pi}{B} y\right) \tag{2-7}$$

Now I will only focus on the behaviour of a bar top, by considering a moving coordinate system that moves with the celerity of the bar (y = 0, c = x/t = ω/k). The time derivative of the bed level reduces to:

$$\frac{\delta z_b}{\delta t} = k \cdot s_{x,0} \cdot \sin(-\delta_1) \tag{2-8}$$

Whether the top of the bar is growing or decaying is determined by the phase lag δ_1. Migration is controlled by the location of the peak of dz_b/dt. If the dz_b/dt peak is within half a wavelength downstream of the bar peak, the bar will migrate in the downstream direction, whereas it will migrate in the upstream direction in the opposite case. Table 2-1 shows the values of δ_1 for which the bar is growing, decaying, migrating in the downstream direction and in the upstream direction.

Table 2-1: Bar behaviour dependency on δ_1

Growing bar	$\pi < \delta_1 < 2\pi$
Decaying bar	$0 < \delta_1 < \pi$
Downstream migration	$0 < \delta_1 < 0.5\pi$ or $1.5\pi < \delta_1 < 2\pi$
Upstream migration	$0.5\pi < \delta_1 < 1.5\pi$

The phase lag δ_1 is dependent on the length of the bar, width-to-depth ratio and numerous other characteristics, see Figure 2-2 from Zolezzi and Seminara (2001a). The figure shows the theoretical dependence of δ_1 on the dimensionless wavenumber ($\pi B/L_L$) and on β. It shows that δ_1 leads to migration in the upstream direction for long bars and to migration in the downstream direction for short bars. The phase lag δ_1 leads, theoretically, to unstable bars for all possible wave lengths, but observations in chapter 5 show that for very short bars δ_1 can be larger than 2π, which leads to the decaying of very short bars.

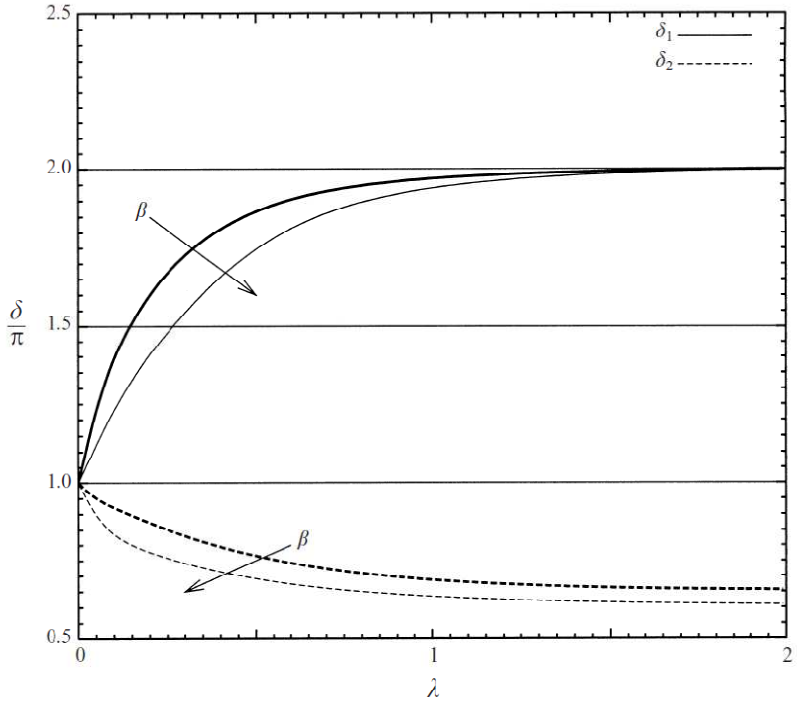

Figure 2-2: The phase lags δ_1 and δ_2 are plotted versus the dimensionless wavenumber ($\pi B/L_L$) for $\beta = 10 < \beta_{res}$ and $\beta = 20 > \beta_{res}$ (plane bed, $\vartheta = 0.1$, $d_s = 0.01$ and $\beta_{res} = 16.5$) (Zolezzi and Seminara, 2001a)

Figure 2-2 also shows the relation between δ_2 and λ. The variable δ_2 is defined as the phase lag in longitudinal direction between the bed topography and the bed-load transport in lateral direction, which can be found in the following expression:

$$s_y = s_{y,0} \cdot e^{\Omega t} \cdot \cos(kx - \omega t - \delta_2) \cdot \sin\left(\frac{m \cdot \pi}{B} y\right) \qquad (2\text{-}9)$$

In which s_y is the bed-load transport in lateral direction per unit width and $s_{y,0}$ the sediment transport perturbations at t=0 in the lateral direction per unit width. Zolezzi and Seminara (2001a) derived the following relation between the migration rate and the phase lags δ_1 and δ_2:

$$\frac{\omega}{s} = \frac{\lambda s_{x,0}}{z_{b,0}} \cos(\delta_1) + \frac{m\pi s_{y,0}}{2 z_{b,0}} \sin(\delta_2) \qquad (2\text{-}10)$$

In which s is the total bed-load transport per unit width. Figure 2-2 shows that δ_2 is between 0.5π and π for all possible wave lengths. The second term of equation (2-10) is therefore always positive, which yields that δ_2 always has a contribution to migration in the downstream direction. For small values of β the second term prevails over the first term, which means that all possible bars will migrate in downstream direction. For sufficiently large β values, the first term prevails over the second term, which leads to migration in the upstream direction for sufficiently-long bars. The β value which is on the transition between these two 'regimes' is the resonant half-width-to-depth ratio.

Upstream influence
As described in chapter 1, the experiments of Zolezzi et al. (2005) discovered that under super-resonant conditions both upstream and downstream of the bend non-migrating bars develop. The bend was said to have an influence in downstream and upstream direction. The presence of downstream influence could be easily explained with an analysis of characteristics. Upstream influence, however, was less straightforward to explain. Zolezzi and Seminara (2001a) explained upstream influence under super-resonant conditions by the fact that only in these conditions it is possible for sufficiently-long small-amplitude bars to travel in the upstream direction. In chapter 6 I investigate the way the bend has an upstream influence under super-resonant conditions. The results in that chapter support the theoretical prediction of Zolezzi and Seminara (2001a), because an alternate pattern, starting at the upstream bend entrance, is observed to propagate in the upstream direction.

2.3 Analytical models

In the 1960s it was proposed that alternate bars can be explained by a stability analysis of the mathematical equations for flow and sediment transport. In 1985, two important linear theories were published, which are the base for the present theories. One of these theories, Blondeaux and Seminara (1985), assumes that migrating bars in a straight channel, without geometrical perturbations, become non-migrating under resonant conditions. The other classical linear theory was published by Struiksma et al. (1985). In this theory, it is assumed that non-migrating alternate bars are generated by a geometrical perturbation, for instance a groyne, change in channel curvature, etc.

In this research, I mainly apply the analytical model of Colombini et al. (1987). This analytical model is based on the work of Blondeaux and Seminara (1985). Only for the discussion in section 5.3.3 the

model of Struiksma et al. (1985) is used. In this section, I only discuss the theory of Blondeaux and Seminara (1985) briefly, for it is the base of the model I have used. The formulas of Colombini et al. (1987) will not be given in this report, I refer to their paper for those details.

2.3.1 Blondeaux and Seminara (1985)

In the paper of Blondeaux and Seminara (1985) a bend theory is presented. This theory not only investigates the stability of bars, but also the stability of a bend separately. In the paper, it is assumed that under certain conditions the meander amplification rate is maximal. These conditions are called the resonance conditions. In order to investigate the range of resonance conditions for various river characteristics, the walls of this model are erodible. Like many other linear bar theories, this model is based on the equations for flow (momentum and continuity) and sediment transport. The water depth, velocity, sediment transport, etc. are assumed to consist of a zero-order (average) value and a small harmonic perturbation. For the velocity in the longitudinal direction this approach is shown in equation (2-11).

$$\frac{u}{u_0} = 1 + \varepsilon \cdot u' e^{i(kx - \Omega t)} \qquad (2\text{-}11)$$

In which u is the longitudinal velocity, u_0 the zero-order velocity in longitudinal direction, ε a small perturbation, u' the perturbation of the longitudinal velocity, k is wavenumber of the developing bar in longitudinal direction and $-i\Omega$ is a complex number, the real part represents the amplification rate of the developing bar and the imaginary part defines its angular velocity

The most-unstable meander wave length was associated with non-migrating alternate, non-amplifying bars, see Figure 2-3.

Therefore, it is thought that meander development is associated with non-migrating and non-amplifying alternate bars. In straight channels, without any sinuosity, the selected alternate-bar wavenumber will be the one which has the maximum amplification rate. However, as sinuosity develops, the alternate flow pattern, induced by the sinuosity, will reinforce the alternate bars with wavenumbers near the resonant wavenumber. When these non-migrating alternate bars are growing, the forces on the banks will also increase, so the meander will be reinforced, and so on. The problem with this theory is that it is not clear how non-migrating bars are formed in rivers above or below resonance conditions.

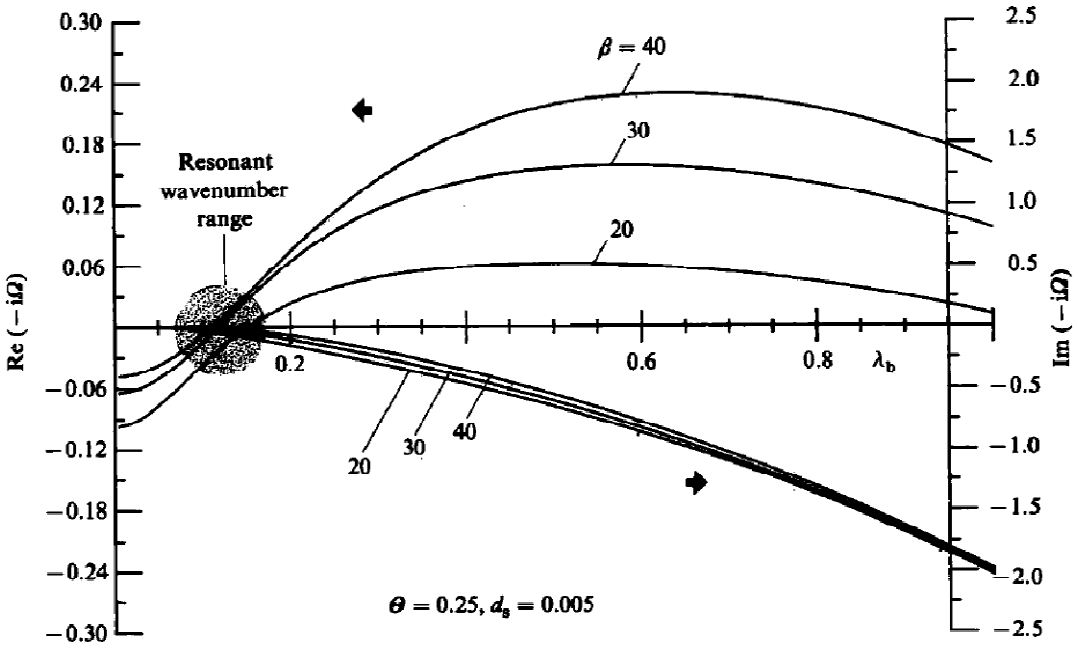

Figure 2-3: The growth rate and propagation frequency of bar perturbations is plotted versus the bar wavenumber (Blondeaux and Seminara, 1985)

2.3.2 Colombini et al. (1987)

The model of Colombini et al. (1987), which continued from the model of Blondeaux and Seminara, can be used to calculate the following bar characteristics:

- The wave length of forced bars
- The wave length of the most-unstable free bar
- The migration rate and amplification rate of free bars
- The half-width-to-depth ratio associated with resonance, β_{res}. For larger β values the conditions are called super-resonant, whereas lower β values correspond to sub-resonant conditions.

The disadvantage of linear theories is that they are based on small-amplitude perturbations, and are therefore only valid for small-amplitude bars (see section 4.2.2.3). Linear theory assumes the amplification rate and migration rate of the bars not to be dependent on the bar height. It is shown that bar height does influence the amplification rate (Figure 4-3) and migration rate and direction (Figure 6-8). The influence of the bar height is called a non-linear effect. Despite these disadvantages, linear theory still provides a reasonable prediction of the wave length of the bars and a reasonable prediction of the half-width-to-depth ratio associated with resonance. This can be concluded by reading the work of Zolezzi et al. (2005), in which they compare experimentally observed bar properties in both sub- and super-resonant conditions with the predictions of linear theory.

3 Analytical model

3.1 Objective

This research applies the analytical model for forced and free bars, based on research by Colombini et al. (1987). This analytical model is used to compare the numerical results with theory. The objective of this chapter is:

"Deriving the analytical model for the specific settings of the present research"

3.2 Methodology

A Fortran model was provided by Dr. G. Zolezzi, in which the analytical model of Colombini et al. (1987) was implemented. I converted this Fortran model into a MATLAB R2011b [version 7.13.0564, MathWorks] model, in order for it to be more user friendly.

In the paper of Colombini et al., the Einstein (1950) formula is used to predict the roughness and the Engelund and Hansen (1967) formula to predict bed-load transport. In the Delft3D model of the present study, the roughness is based on the White-Colebrook relation and the bed-load transport is computed with the formula of Meyer-Peter and Müller (1948). To be able to make a comparison between the numerical model and the analytical one, the latter is adjusted. The parameters which need to be derived to adjust the model are:

$$C_D = \frac{1}{c_{f,0}} \frac{\partial c_f}{\partial \tilde{D}}, \quad C_T = \frac{\theta_0}{c_{f,0}} \frac{\partial c_f}{\partial \theta}, \quad \Phi_D = \frac{1}{\Phi_0} \frac{\partial \Phi}{\partial \tilde{D}}, \quad \Phi_T = \frac{\theta_0}{\Phi_0} \frac{\partial \Phi}{\partial \theta} \tag{3-1}$$

In which:

$$\tilde{D} = \frac{D}{D_0} \tag{3-2}$$

In these formula's c_f denotes the friction coefficient, D the water depth, θ the Shields parameter and Φ the transport parameter. Dimensionless variables are denoted with a '~' and the subscript '0' stands for the value in the initial uniform situation. The four variables in equation (3-1) take the dependence of the roughness and the transport parameter on the water depth and the Shields stress into account. The derivation of the parameters can be found in Appendix B.
The other expressions for the analytical model can be found in Colombini et al. (1987) and are not repeated in this report.

3.3 Results

The analytical model is based on Colombini et al. (1987), and is adjusted as described in section 3.2.

In Figure 3-1 one can see the free-bar diagram, based on F_0 (zero-order Froude number) = 0.75, D_{50} (median grain size) = 1 mm and i_0 (initial longitudinal slope) = 0.011, which are the characteristics of all the numerical simulations in this research. The dotted lines represent the free-bar diagram of the original analytical model (Colombini et al., 1987), in which the Einstein formula was used to predict the roughness. The other line represents the free-bar diagram, calculated with the adjusted analytical model, with the White Colebrook relation as roughness predictor. On the horizontal axis the dimensionless wavenumber ($\pi B/L_L$) is given and on the vertical axis the half-width-to-depth ratio. The red lines are called the marginal curve, which represents free bars that are non-amplifying. The black lines represent non-migrating bars. Bars, located on the left of the black curve, migrate from downstream to upstream, whereas bars, located on the right of the black curve, migrate from upstream to downstream. The blue lines correspond to the most-unstable bars (with the largest amplification rate, for a certain β value).

The use of the diagram is shown with an example (this example is based on the adjusted model). Suppose the simulation to have a β value of 20: according to linear theory, bars with a dimensionless wavenumber between 0.17 and 1.49 will grow, whereas longer or shorter bars will decay when they are imposed. The fastest growing, and therefore dominant, bar will have a dimensionless wavenumber of 0.88. Linear theory predicts this most-unstable bar to appear first. Bars with a dimensionless wavenumber smaller than 0.47 will migrate in the upstream direction, whereas shorter bars will migrate in the downstream direction.

The difference between both diagrams is large. This shows that the solution of the analytical model is strongly influenced by the type of roughness prediction. The curve for non-migrating alternate bars and for the most-unstable alternate bars is, in the adjusted model, more shifted towards shorter bars. The difference does not show that one of the two predictions is flawed, but that it is of importance to use the same roughness prediction in the analytical as in the numerical model, if one wants to compare them.

In chapter 4 the analytical free-bar model will be used to compare the behaviour of small-amplitude bars with the theoretical behaviour. That chapter shows that the adjusted analytical model and the Delft3D model match quite well for small-amplitude bars.

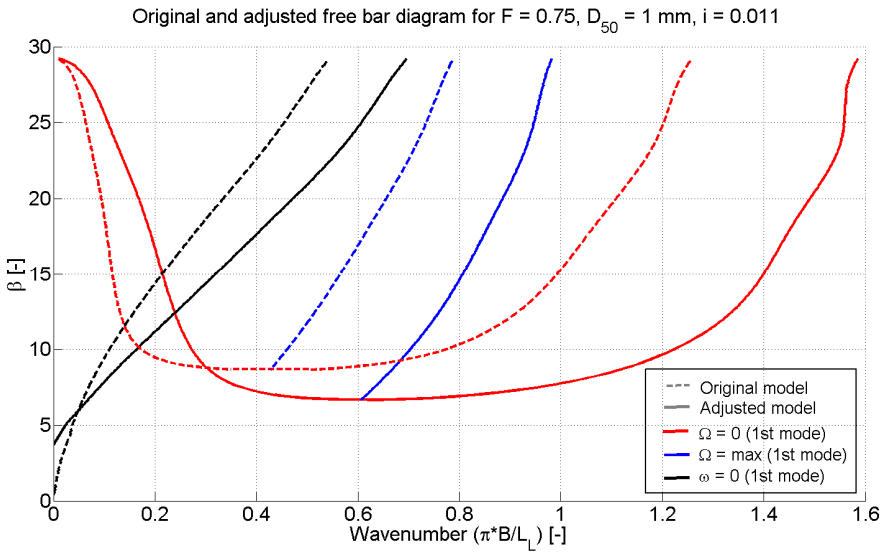

Figure 3-1: Free-bar diagram: comparison between original (Colombini et al., 1987) and adjusted model

4 Numerical model set-up and validation

In this chapter the model set-up is briefly discussed, like the domains, boundary conditions, parameters, etc. The details can be found in Appendix C. Also the settings of all the simulations can be found in Appendix C. Subsequently the model is validated.

Important: I have tried to maximize the use of the same settings through the entire research. However, some parts of this research were carried out before some new insights were found. I did not repeat the simulations if I assessed that the new insight had no significant implication on the former results. One should therefore notice that for example simulation R1, which is used in the validation, is based on the 'upwind' scheme for the morphological updating procedure (see Appendix G), whereas the 'central' scheme was later observed to represent linear theory more properly.

4.1 Objectives

The model of Van der Meer et al. (2011) gives some insight in when upstream and downstream bars develop, see chapter 1. However, it is not clear how these bars develop. Also some differences are observed between the model results and the prediction by several analytical theories. This research goes further with the model of van der Meer et al. (2011). For this continuation, the numerical model of van der Meer is improved and is therefore discussed here.

In short, the objective of this chapter is:

"Improving and validating the numerical model of Van der Meer et al. (2011)."

4.2 Methodology

In this section the numerical model set-up is described, see section 4.2.1. Subsequently, the method of validation is discussed in section 4.2.2. The results of the validation can be found in section 4.3.

4.2.1 Model set-up

4.2.1.1 Program functionality

The numerical modelling is carried out using the Delft3D-FLOW suite [version 4.00.03.565, May 2011, Deltares]. All simulations in this research are based on solving the 2D depth-averaged equations. The output is processed using Delft3D-Quickplot [version 2.16.00450, Deltares] and MATLAB R2011b.

4.2.1.2 Domains

The numerical model of Van der Meer et al. (2011) is based on a laboratory test of Zolezzi et al. (2005). Zolezzi et al. carried out experiments in a laboratory flume with a width of 0.6 m and a length of 32 m. The laboratory flume contained a 180˚ bend, with a radius of 2.5 m, and consequently a length of 8 m. The original domain of van der Meer et al. (2011) is named 'Domain 1'. For this research the original domain of van der Meer et al. is extended in the upstream direction (Domain 2, see Figure 4-1). This is mainly done for two reasons:

- Taking a possible boundary disturbance further away from the bend
- To be able to analyse the development of upstream bars

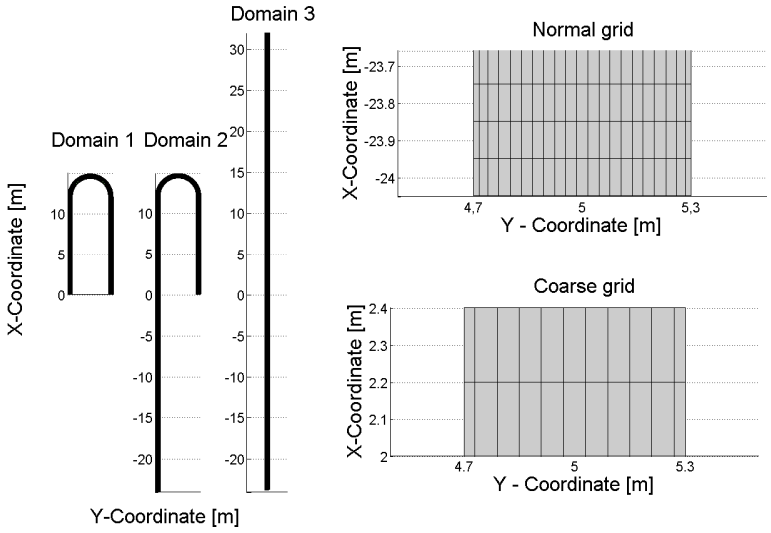

Figure 4-1: Overview of computational grids

Another domain is constructed to be able to investigate alternate-bar generation if the bend is absent and to investigate the behaviour of small-amplitude bars. In the following part, this domain is referred to as 'Domain 3'.

Three types of grid resolutions are used:

- Coarse: longitudinal grid size = 0.2 m, transverse grid size = 0.06 m (except the outer cells, which have a transverse grid size of 0.03 m).
- Normal: Longitudinal grid size = 0.1 m, transverse grid size = 0.03 m (except the outer cells, which have a transverse grid size of 0.015 m).
- Laterally fine: Longitudinal grid size = 0.1 m, transverse grid size = 0.015 m (except the outer cells, which have a transverse grid size of 0.0075 m).

The normal variant of Domain 2 is denoted as Domain 2n, the coarse variant as Domain 2c and the lateral fine variant as Domain 2l. The same procedure of referring is applied for the other domains.

The main focus of this research is on alternate bars. The transverse wave length of alternate bars is twice the channel width, 1.2 m. The coarse grid has therefore 20 grid cells per wave length in the transverse direction, the normal grid about 40 and the laterally fine grid about 80. In general, it is thought that a wave has to be represented by 20-30 grid cells to reproduce it accurately. So still the coarse grid should be able to reproduce the alternate bar. In the longitudinal direction the coarse grid should be able to represent bars with a longitudinal wave length of at least 4 m. The normal and laterally fine grid should be able to represent bars longer than about 2 m.

The grids in Figure 4-1 are displayed in a x-y coordinate system. For the output in some cases also m and n coordinates are used, in which m is the longitudinal coordinate (starting at the upstream boundary) and n is the transverse coordinate (starting at the left bank).

4.2.1.3 Boundary conditions

Open boundaries

At the upstream boundary four different types of boundary conditions are used for the simulations:

- Q: total discharge, uniform in space and time
- Q_P: total discharge, uniform in space, varying in time. The discharge is randomly perturbed with a maximum amplitude of +/- 1% of the uniform discharge
- $Q_{P,cell}$: Discharge per cell, varying in space and varying in time. The discharge is specified per cell and is perturbed with a maximum amplitude of +/- 1% of the uniform discharge
- WL: water level, uniform in space and time. The total discharge boundary always produced a small perturbation (probably due to a different numerical scheme at the boundary), therefore a water level boundary had to be specified to get rid of any boundary disturbance.

At the downstream boundary one type of condition is used:

- WL: water level, uniform in space and time.

Closed boundaries

Wall roughness locally has an influence on the hydrodynamics and morhpodynamics. But because the simulations have a large width-to-depth ratio, wall roughness seems to have an insignificant influence on the bar pattern. Therefore a free-slip (no tangential stress along the closed boundary) condition is used along the closed boundaries. Another reason for applying a free-slip condition is that a partial-slip condition destabilizes the simulation, because the Reynolds stresses at the wall are integrated explicitly.

4.2.1.4 Roughness

Van der Meer used a constant Chézy roughness of 22.5 $m^{1/2}s^{-1}$. For large-scale rivers, a constant Chézy value is reliable, but for a simulation on laboratory scale the roughness should be related to the actual water depth (Lesser et al., 2004). Otherwise the roughness height of the bottom becomes a function of the water depth, which is not realistic. Lesser et al. also observed that a constant Chézy roughness value leads to strong damping effects in the model, so less alternate bars would become visible. Therefore the White-Colebrook relation is used, which yields:

$$C = 18^{10}\log\left(\frac{12D}{k_s}\right) \qquad (4\text{-}1)$$

where k_s is the Nikuradse roughness height [m] and D the water depth. The linear model also predicts the alternate-bar behaviour to be different for both roughness definitions, see Appendix B.

Delft3D has problems with flows that are near the transition of sub- and super-critical flow. To prevent the flow from becoming super-critical, the bed had to be rough. The specified Nikuradse roughness height is defined such that the Froude number in all simulations was initially 0.75. In Figure 4-2 the theoretical values for k_s are plotted against the discharge.

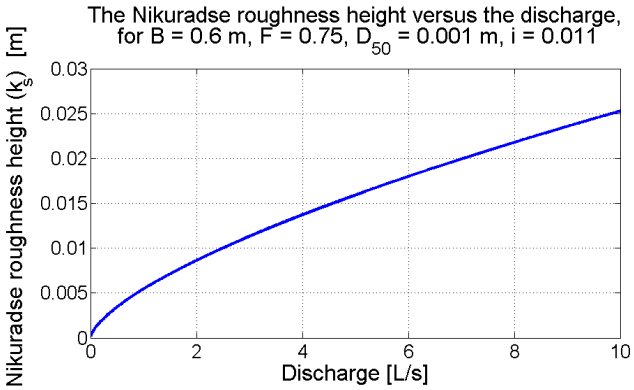

Figure 4-2: Theoretical values for the Nikuradse roughness height versus the discharge, for Froude = 0.75

4.2.1.5 Viscosity

According to an HLES simulation (Horizontal Large Eddy Simulation), the horizontal eddy viscosity in the model should be $O(10^{-5})$ m^2/s, see Appendix C. The simulations have shown to be unstable for such low eddy viscosity values. In order to get stable results the eddy viscosity in the simulations is set at 0.01 m^2/s, the same value as used by Van der Meer et al. (2011). The influence of the horizontal eddy viscosity on several alternate-bar parameters is discussed in chapter 5.

4.2.1.6 Morphology

Like in the model of Van der Meer et al. (2011), the Meyer-Peter and Müller (1948) is used to compute the bed-load transport.:

$$s = 8\alpha D_{50}\sqrt{\Delta g D_{50}}\left(\mu\theta - \theta_{cr}\right)^{\frac{3}{2}} \qquad (4\text{-}2)$$

in which s is the sediment transport per unit width, D_{50} the median grain size, θ the Shields number, θ_{cr} the critical Shields number (0.047) and μ the ripple factor. The ripple factor is set at 0.7.

Suspended transport is not taken into account. In the model of van der Meer et al., α was set at 1/8, whereas it should be in the order of one. This correction, which is applied for the model in this research, has mainly an effect on the time scale of bar development.
I have used a constant sediment size of 1 mm for all the simulations. This sediment size was also used by Zolezzi et al. (2005), whose experiments are used in the validation of the numerical model.

4.2.1.7 Simulation ID

In this research, simulations that started with a flat or randomly perturbed bed are labelled with 'R', followed by the number of the simulation. Simulations during which small-amplitude bars were imposed on the initial bed are labelled with 'S'. The two simulations that reproduce the experiments of Zolezzi et al. (2005) are called 'U3_D3D' and 'D1_D3D', for they are the Delft3D simulation of experiments U3 and D1 respectively.

4.2.2 Validation of numerical model

The method of validation is described in this section. First, an attempt is made to reproduce laboratory experiments. Very few experiments for upstream influence are available in the literature, so for the validation only two experiments of Zolezzi et al. (2005) were reproduced. One will observe in section 4.3.1 that reproducing these experiments encountered some difficulties, so the model is also tested for other width-to-depth ratios. These simulations, however, could not be compared to experiments directly. But it is still possible to compare the observations more generally with field and laboratory experiments. Then the behaviour of small-amplitude bars is tested, for it should match the prediction of linear theory. Finally the numerical prediction of the wave length of forced and free bars, for different width-to-depth ratios, is compared with linear theory.

4.2.2.1 Reproducing the experiments of Zolezzi et al. (2005)

Zolezzi et al. (2005) carried out five experiments in a U-curved flume. Three of them were in super-resonant conditions and two in sub-resonant conditions. The characteristics of the simulations can be found in Table 4-1. The uniform flow depth, D_0, the discharge, Q_0, and the bed-load transport, S_x, are the only quantities which were measured in the flume. The calculation of the other quantities is based on these measured parameters. The resonant width-to-depth ratio, β_{res}, is based on the analytical model of Colombini et al. (1987), with the Parker (1990) formula for bed-load transport.

Experiments U1 and U2 have a Froude number of 1.04. Delft3D has problems with flows that fluctuate between sub- and super-critical flow. These fluctuations cause instability. Therefore, the experiments U1 and U2 could not be reproduced. In D2, no significant non-migrating perturbations were observed. Because this report focuses on non-migrating alternate bars also D2 is not reproduced with the numerical model. 'U3' and 'D1' are therefore the only experiments which are tried to be reproduced. 'U3' will be simulated with simulation 'U3_D3D', and 'D1' will be simulated with 'D1_D3D'.

Table 4-1: Characteristics of experiments by Zolezzi et al. (2005)

Run	U1	U2	U3	D1	D2
β [-]	21.4	20	15	12	8.6
β_{res} [-]	11	11.7	14.6	17.3	22.1
d_s [-]	0.071	0.067	0.050	0.040	0.028
F_0 [-]	1.04	1.04	0.75	0.74	0.85
Θ [-]	0.093	0.1	0.133	0.167	0.233
D_0 [m]	0.014	0.015	0.020	0.025	0.035
Q [m^3s^{-1}] x 10^{-3}	3.25	3.6	4.0	5.5	10.5
S_x [m^3s^{-1}] x 10^{-6}	5.72	6.55	7.01	1.07	19.82

First, the hydrodynamic and morphodynamic calibration method is discussed and then the validation method of the model for these simulations.

Hydrodynamic calibration method for 'U3' and 'D1'

The discharge from Table 4-1 is used as input at the upstream boundary. Subsequently the water depth is calibrated by varying the Nikuradse roughness height. In both simulations the DPS (depth at grid cell centre) and the DPU (depth at velocity point) are set at 'MEAN'. Otherwise the waterdepth is over- or underpredicted by the model.

Morphodynamic calibration method for 'U3' and 'D1'

The bed-load transport at the downstream end of the flume was, during the experiments of Zolezzi et al., measured by a volumetric sampling technique. They compared their measured transport rates with the 2D predictors for bed-load transport of Meyer-Peter and Müller (1948) and Parker (1990). They discovered that the Parker predictor was more accurate in this case. In Delft3D, however, the Parker formula has not been implemented and cannot be implemented by the option 'general transport formula'. Therefore, the Meyer-Peter and Müller formula is used to reproduce the experiments.

The numerical simulations are calibrated such that the bed-load transport in the model matches the experimentally measured bed-load transport. This is done by varying the calibration coefficient of the Meyer-Peter and Müller (1948) formula, α. The formula is presented here:

$$s = 8\alpha D_{50}\sqrt{\Delta g D_{50}}\left(\mu\theta - \theta_{cr}\right)^{\frac{3}{2}} \qquad (4\text{-}3)$$

In which s is the sediment transport per unit width, D_{50} the median grain size, θ the Shields number, θ_{cr} the critical Shields number (0.047) and μ the ripple factor. The ripple factor is set at 0.7.

Subsequently, the transverse slope effect on the bed-load transport is calibrated. For bed-slope effects the formulation of Koch and Flokstra (1980), extended by Talmon et al. (1995), is used. The

effect of transverse slopes on the direction of the bed-load transport is given by the following equations:

$$\tan(\varphi_s) = \frac{\sin(\varphi_T) + \frac{1}{f(\theta)}\frac{\partial z_b}{\partial y}}{\cos(\varphi_T) + \frac{1}{f(\theta)}\frac{\partial z_b}{\partial x}} \quad (4\text{-}4)$$

$$f(\theta) = A_{sh}\sqrt{\theta} \quad (4\text{-}5)$$

In which φ_s is the direction of sediment transport, φ_T the direction of bed shear stress, f the shape factor for grains and z_b the bed level. The coefficient A_{sh} is varied such that the pool depth and bar height in the simulations are in the same order of magnitude as in the experiments.

Validation for 'U3' and 'D1'

This research focuses on non-migrating alternate bars. The validation of the numerical model is therefore focused on the non-migrating bed topography of the simulations. The non-migrating bed topography is calculated by averaging the bed level over an integral amount of wave periods. By doing so, the presence of upstream non-migrating bars can be investigated. Also the wave length of the non-migrating bars is compared to the experimental data.

4.2.2.2 Simulation with β=24.3

Although non-migrating upstream alternate bars are not observed for U3_D3D, as one will observe in section 4.3.1, it can be observed for larger β values. This will be shown for a simulation with a β value of 24.3. The characteristics of the simulation can be found in Table 4-2.

Table 4-2: Characteristics of simulation R1

Domain	β	Boundary conditions	k_s [m]	v_H [m^2/s]	A_{sh} [-]	Morphological updating scheme	Initial bed
2n	24.3	Q_P-WL	0.008	0.01	1.9	'upwind'	flat

The A_{sh} has a lower value than in the simulation U3_D3D and D1_D3D. The reason for this is that this simulation was done before the reproduction of the experiments of Zolezzi et al. (2005). So the A_{sh} could not be calibrated at that time. I asses that this difference does not have significant consequences for the validation, because the validation in this case is only qualitative and not quantitative.

Because no experiment has been done with these conditions, the results cannot be directly compared to experiments. The validation will therefore be based on qualitative assessments of the observations and quantitative comparison with analytical theories.

4.2.2.3 Small-amplitude bars

Because of a lack of experimental data, the model is also validated for small-amplitude bars. Linear theory is based on small-perturbations and should therefore match the numerical model for small-amplitude bars. A bar is subjected to linear growth if the amplification rate is not dependent on the bar height. By imposing small-amplitude bars with different amplitudes, I found that the amplification rate is not dependent on the bar height if the bar amplitude is smaller than 2% of the water depth, see Figure 4-3. The characteristics of these simulations can be found in Table 4-3.

Table 4-3: Characteristics simulation S1-S6, see Table C-4 in Appendix C for more information

Constant							Variable
Domain	**B [-]**	**v_H [m^2/s]**	**A_{sh} [-]**	**Morphological updating scheme**	**L_L [m]**	**Mode [-]**	**h_0 [m]**
3n	24.3	0.01	1.9	'upwind'	7.5	1	0.00001 - 0.002

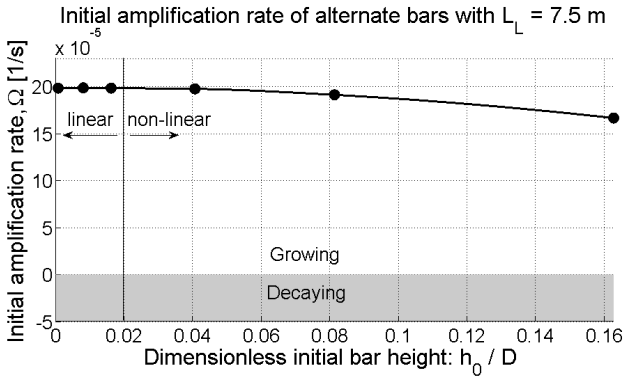

Figure 4-3: Amplification rate versus the initial bar height

By imposing alternate bars with an amplitude of 0.1 mm (about 0.8% of the initial water depth) and varying wave lengths, the amplification rate and migration rate of small amplitude bars is investigated. The numerically observed behaviour is compared to the prediction of the analytical model. The amplification rate of the small-amplitude bars is calculated by carrying out a Fourier analysis of the bar pattern with a one-minute interval. As long as the amplification rate is constant over time, the growth process is linear.

Table 4-4: Characteristics of simulation S7-S28, see Table C-4 in Appendix C for more information

Constant						Variable	
Domain	**B [-]**	**v_H [m^2/s]**	**A_{sh} [-]**	**Morphological updating scheme**	**h_0 [m]**	**L_L [m]**	**Mode [-]**
3n	24.3	0.01	1.9	'central'	0.0001	1 - 30	1-2

4.2.2.4 Observed wave length – vs – linear theory

The wave length of free and forced bars is investigated for simulations with the following half-width-to-depth ratios:

- β = 9.06, 12.05, 15.71, 18.75, 21.28

Free bars are generated by applying an undisturbed discharge over a disturbed bed level. Forced bars are generated by applying a groyne, which blocks half the channel, as shown in Figure 5-1. The characteristics of the simulations are presented in Table 4-5.

Table 4-5: Characteristics of simulations R5 – R14, see Table C-3 in Appendix C for more information

Constant						Variable	
Domain	**Boundary conditions**	**ν_H [m^2/s]**	**A_{sh} [-]**	**Morphological updating scheme**	**Initial bed**	**β**	**k_s [m]**
3n	Q-WL	0.01	1.9	'central'	Randomly perturbed +/- 0.1 mm	9.1 - 21.2	0.009 - 0.022

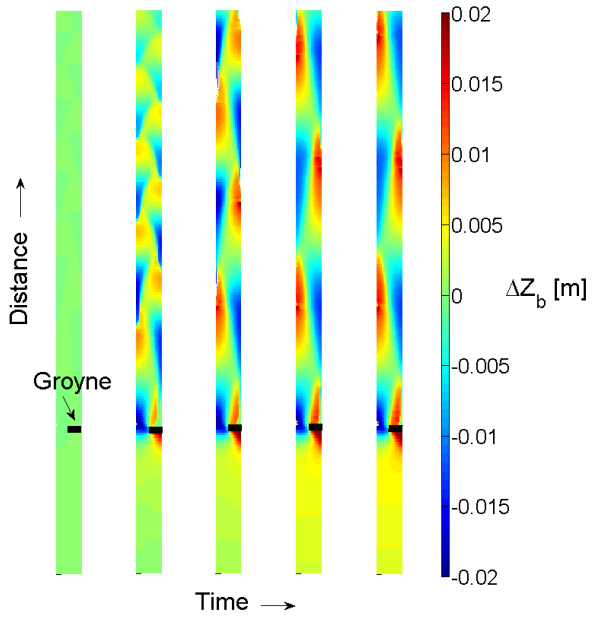

Figure 4-4: Forced-bar development by applying a groyne

4.3 Validation results

The methodology applied for the validation of the numerical model is described in section 4.2.2. In this chapter the results of the calibration and validation are presented. First, I discuss the attempt to reproduce the experiments of Zolezzi et al. (2005), then the validation is continued with a simulation with a large β value (very super-resonant). Subsequently, the behaviour of small-amplitude bars is compared with linear theory. Finally, the observed free and forced wave lengths are compared to the literature and linear theory.

4.3.1 Reproducing experiments of Zolezzi et al. (2005)

4.3.1.1 Hydrodynamic calibration for 'U3' and 'D1'

The calibrated values for the Nikuradse roughness height can be found in Table 4-6.

Table 4-6: Results of hydrodynamic calibration

Calibration parameter	U3_D3D	D1_D3D
K_s [m]	0.0123	0.0162

4.3.1.2 Morphodynamic calibration for 'U3' and 'D1'

The pool depth during the experiments was in the order of $2D_0$, whereas the top of the bars was about $0.7D_0$ above the mean bed level. For U3_D3D the influence of A_{sh} on the pool depth and bar height is shown for t = 2 h. Because D_0 is 0.020 m, the pool depth should be in the order of -0.04 m and the top of the bar should be at about 0.014. One can see that an A_{sh} of 4 represents this bar geometry the best.

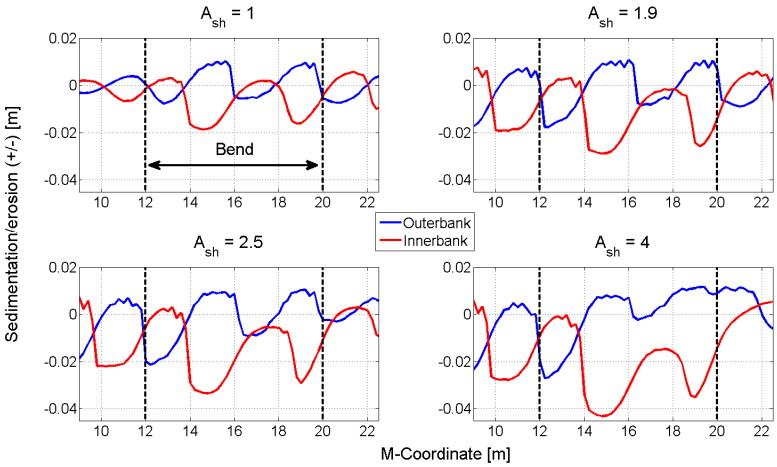

Figure 4-5: Influence of A_{sh} on pool depth and bar height for U3_D3D, t = 2 h

The values for α and A_{sh} can be found in Table 4-7.

Table 4-7: Results of morphological calibration

Calibration parameter	U3_D3D	D1_D3D
α	1.025	0.865
A_{sh}	4	4

4.3.1.3 Validation for 'U3' and 'D1'

During the physical experiments, a combination was observed of migrating and non-migrating alternate bars. The non-migrating bars were found after averaging the bed over one or more wave periods. In Figure 4-6, one can see the non-migrating bed patterns of U3 and D1, measured by Zolezzi et al. (2005). It is clear that in U3 non-migrating bars occurred both upstream and downstream of the bend, whereas in run D1 only in the bend and downstream of it alternate bars appeared. In Figure 4-7 one can see the averaged bed levels of the numerical simulations.

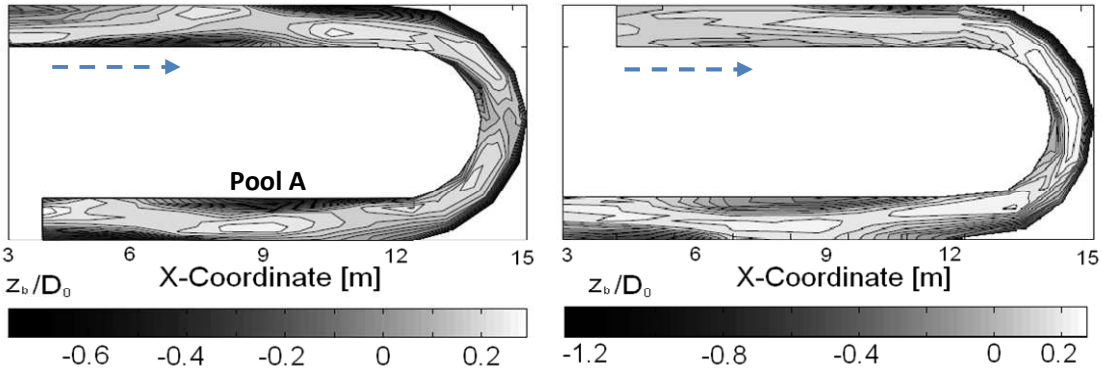

Figure 4-6: Non-migrating bed topographies, U3 (left), D1 (right). (Zolezzi et al., 2005). Note that notations are changed.

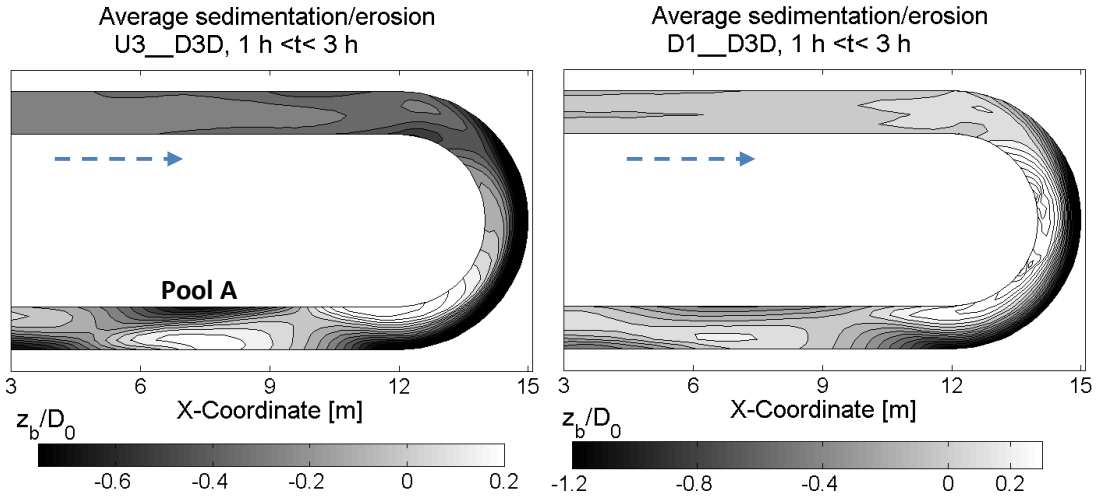

Figure 4-7: Averaged sedimentation and erosion U3_D3D (left), D1_D3D (right).

Comparison between U3 and U3_D3D

Agreement:

- The wave length is comparable for the experiment (L_L =9.0 m) and the numerical simulation (L_L = 8.5 m)
- The location of the downstream bars is quite similar, only a small shift (of about 2 m) in the downstream direction can be observed for the numerical model (compare the location of 'Pool A' in both figures).

Disagreement:

- No upstream non-migrating bars in the numerical model can be found, whereas they were observed experimentally. The numerical simulation is still sub-resonant, whereas the experiment is in a super-resonant regime.

Comparison between D1 and D1_D3D

Agreement:

- The wave length is comparable for the experiment (L_L =7.9 m) and the numerical simulation (L_L = 8.4 m).
- The pattern matches both upstream and downstream of the bend.

4.3.2 Simulation with β=24.3 (qualitative validation)

Upstream alternate bars

In Figure 4-8, one can see the equilibrium bed level of R1. Contrary to U3_D3D, this time also upstream of the bend non-migrating alternate bars occur. This pattern corresponds qualitatively with the experimental results of Zolezzi et al. (2005) under super-resonant conditions.

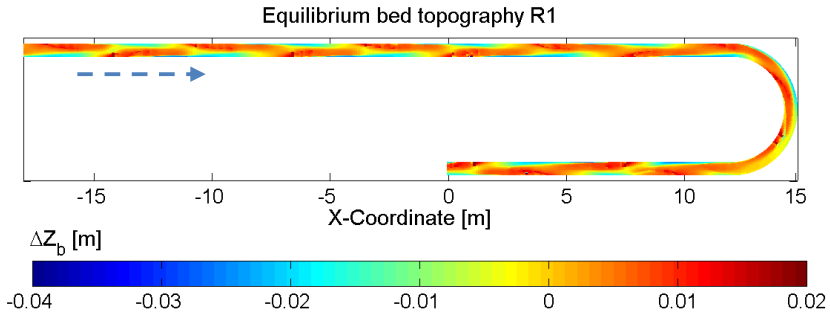

Figure 4-8: Equilibrium bed level R1

Wave length and bar amplitude development

Various authors (Fujita and Muramoto, 1985, Lanzoni, 2000) observed during experiments that the bar pattern first 'selects' the wave length of the bars and then the wave height. This has also been observed in the numerical simulation, see Figure 4-9. In this figure, the wave length, relative to the equilibrium wave length, is plotted versus the bar amplitude, relative to the equilibrium bar amplitude, for different time steps. For more information about the interaction between the wave length and the bar amplitude one is referred to Appendix I.

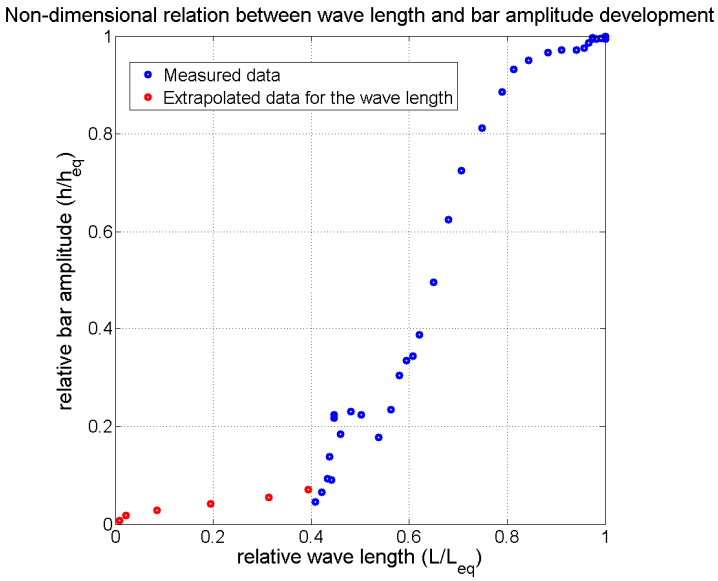

Figure 4-9: Non-dimensional relation between wave length and wave height development, R1

Spectral composition of bar pattern

Many authors have analysed the bed topography of alternate-bar patterns and discovered that all alternate-bar patterns have roughly the same spectrum. The fundamental harmonic is called the 1-1 harmonic mode, which means first mode in the longitudinal direction and first mode in the transverse direction. See section 2.1 for more information about this bar classification. Seminara and Tubino (1992) found that the fundamental harmonic represents about 15-30% of the total "energy" of the bed. Apart from the fundamental harmonic also second-mode harmonics were present in most alternate-bar patterns. This second-mode harmonic was observed by Zolezzi et al. (2005), Colombini and Tubino (1990), Seminara and Tubino (1992), and various other authors. Seminara and Tubino (1992) observed that the total "energy" of the second-mode harmonics in the axial and the radial direction (2-2, 0-2, 2-0) is in the order of one third of the "energy" represented by the fundamental harmonic.

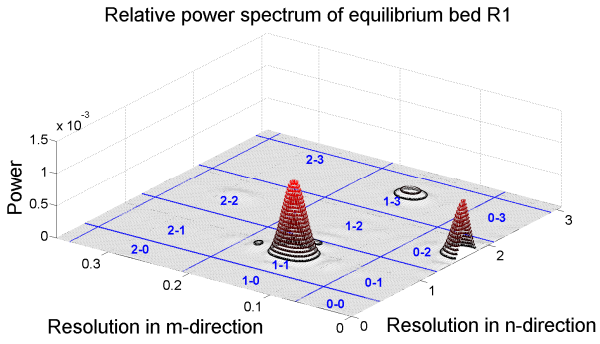

Harmonic	L_T* [m]	L_L [m]	h [mm]	Rel. "power" [%]
1-1	1.2	7.0	19.9	35
0-2	0.6	8	9.8	14
1-3	0.4	7.0	8.8	5

Figure 4-10: Power spectrum of equilibrium bed topography R1;
Table 4-8: Characteristics of the three main peaks in R1, at t=144 h
* L_T means the lateral wave length

In Figure 4-10 one can see the spectral composition of the non-migrating bars in simulation R1. It is clear that the 1-1 peak has the largest contribution, as proposed in the literature. Furthermore I can observe a 0-2 harmonic, which represents a 'central' deposit. The relative "power" of the main harmonics can be found in Table 4-8. The contributions of the 1-1 and 0-2 harmonic are a bit higher than in the literature, but still comparable. More about the development of the bed topography spectrum in simulation R1 can be found in Appendix H.

4.3.3 Small-amplitude bars

In Figure 4-11 (left), the initial amplification rate of small-amplitude (h_0 = 0.1 mm ≈ 0.008D_0) alternate bars is presented. The output of the numerical model complies with linear theory. This match was only achieved by applying the 'central' scheme for the morphological updating procedure. More about the influence of the morphological updating procedure can be found in section 5.3.1. The amplification rate of second-mode bars is not well represented by the model, see Figure 4-11 (right). Possible reasons for this discrepancy are discussed in section 5.3.1.

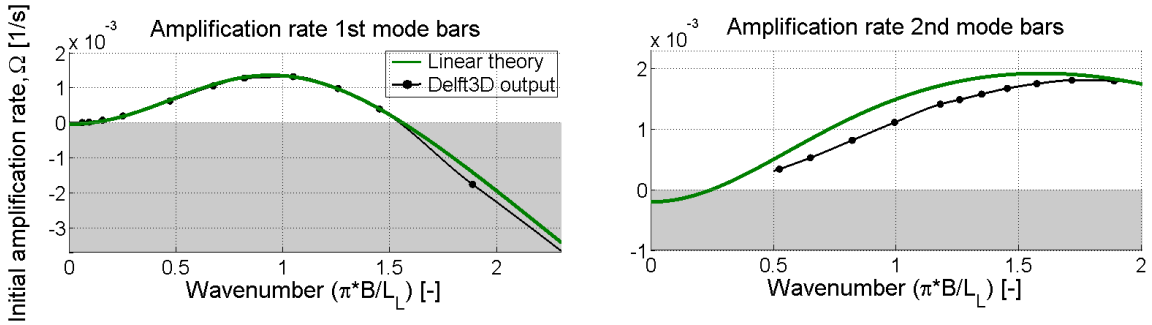

Figure 4-11: Initial amplification rate of small-amplitude first and second-mode bars, Θ =24.3

In Figure 4-12, the observed migration rate of small-amplitude bars is plotted with the linear theory prediction. For moderate wave lengths the numerically observed migration rate complies with the analytical migration rate. For very long and very short alternate bars, the migration rate in the model is less than predicted by analytical theory.

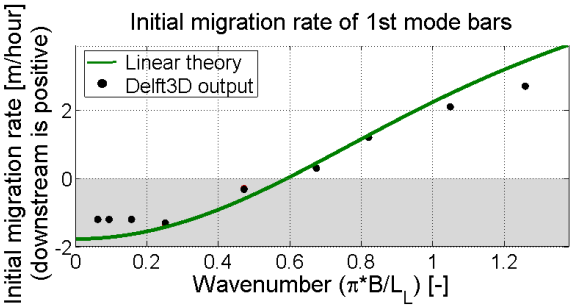

Figure 4-12: Initial migration rate of small-amplitude bars, Θ =24.3

4.3.4 Observed wave length - vs- linear theory

In Figure 4-13, one can see the observed wave length of forced and free bars, plotted together with the linear free-bar diagram.

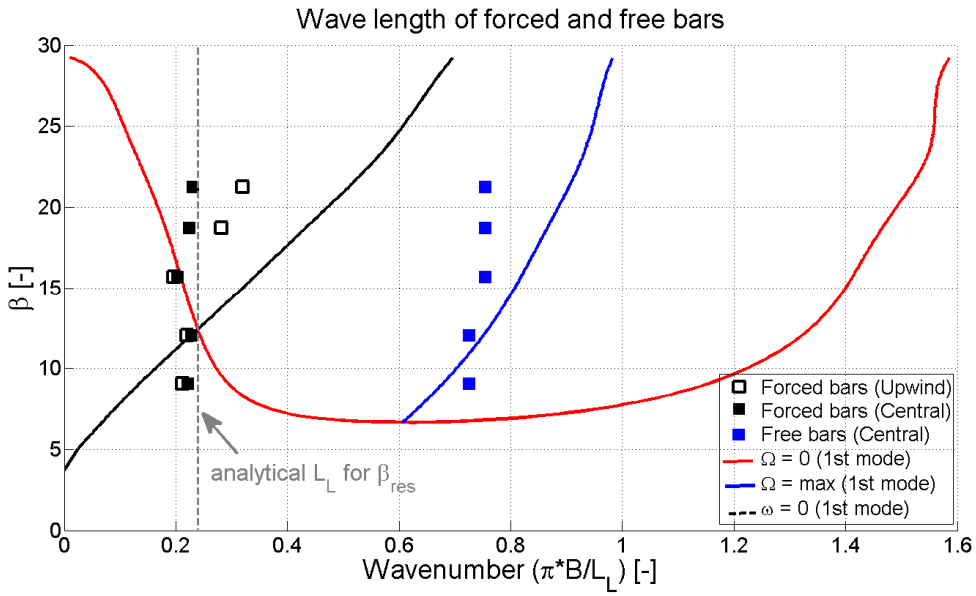

Figure 4-13: Observed wave length of forced and free bars, 'central' scheme for the morphological updating procedure

Free bars

The observed free-bar wave lengths are generally larger than the wave length corresponding with the most-unstable bar for small-amplitude bars and less dependent on β. In the first stage of free-bar development, the alternate-bar pattern has the wave length of the most-unstable bar, according to the test of small-amplitude bars. However, when the bar grows, also the wave length of the bar grows. This means that non-linear effects cause the most-unstable bar to be longer for larger amplitudes. It therefore seems that linear theory fails to predict the wave length of free bars properly. The numerical model seems to be more complete, for it includes non-linear effects. However, no assessment can be made on the accuracy of the numerically predicted free-bar wave lengths.

Forced bars

In section 4.3.1.3, it has been shown that the wave length of the downstream non-migrating bars in the numerical model agrees with the observed wave length in the experiments of Zolezzi et al. (2005).

In Figure 4-13, one can see that the wave length of forced bars (for the central method) is not really dependent on β. This complies with linear theory, which predicts the forced-bar wave length to be equal to the wave length under resonance conditions. In the figure, one can see that the observed forced-bar wave lengths are close to the analytical L_L during β_{res}.

Although the wave length of forced bars in the numerical model seems to be comparable to experimental and theoretical values, it does not coincide with the numerical observations of Vanzo et al. (2011). In that paper, they proposed that the wave length of forced bars tends towards the wave length of the most-unstable bar (becomes shorter) for larger β. Figure 4-13 shows that in case of the 'upwind' scheme for the numerical updating procedure, the observed wave length agrees with Vanzo et al. (2011). But because the 'central' scheme is thought to be more accurate, I propose those results to be less accurate. This is discussed in section 5.3.2.
The observed 'central' forced bars also do not comply with the observations of Van der Meer et al. (2011), who stated that the wave length of the non-migrating bars was much shorter than predicted by theory for β>13. In fact, they observed the same behaviour as Vanzo et al. (2011). So I also ascribe the wave-length mismatch between the numerical model and linear theory, as proposed by Van der Meer et al. (2011), to 'upwinding', see section 5.3.2.

4.3.5 Conclusion

The model is capable of simulating alternate-bar development in both super- and sub-resonant regimes. In super-resonant regimes both downstream and upstream of the bend non-migrating alternate bars occur. In sub-resonant conditions only downstream of the bend non-migrating alternate bars appear. These observations are in agreement with observations by Zolezzi et al. (2005). The wave length of forced bars is well predicted if the 'central' method is used. Also the behaviour of small-amplitude alternate bars matches linear theory. For second-mode bars, a discrepancy is found between the numerical model and the analytical theory.

However, the model is not capable of reproducing the super-resonant experiments of Zolezzi et al. (2005) directly. The reason for this is that two of the three super-resonant experiments (U1 and U2) have a Froude number of 1.04. Delft3D has problems with simulating flow near the transition between sub- and super-critical flow. The other experiment (U3) is near the transition between sub- and super-resonant conditions. The numerical model appears to overpredict the point of resonance and therefore has problems with reproducing super-resonant regimes near the point of resonance. This was also observed by Van der Meer et al. (2011). The sub-resonant experiment (D1), however, is reproduced accurately by Delft3D.

5 Analysis of numerics

5.1 Objective

During the validation of the present numerical model and the one in the paper of Van der Meer et al. (2011), discrepancies are found between some alternate-bar characteristics in the numerical model and the analytical model. The main discrepancies are found for:

- The resonance half-width-to-depth ratio β_{res}
- The wave length of alternate bars

The objective of this chapter is:

"Studying the effects of some typical numerical factors (typical schemes for the morphological updating procedure, horizontal eddy viscosity and grid resolution) on alternate-bar characteristics"

5.2 Methodology

The influence of numerical diffusion, horizontal eddy viscosity and in some cases the lateral grid resolution are investigated. In this section the methodology of this investigation is described. First, the influence of these numerical characteristics on the behaviour of small-amplitude bars is investigated, for it provides insight in the way larger-amplitude bars behave. Then the influence on the wave length is investigated and finally the influence on the point of resonance.

5.2.1 Influence on small-amplitude bar behaviour

The behaviour of small-amplitude bars can easily be tested with the numerical model. The same procedure of imposing those bars is used as described in section 4.2.2.3. The behaviour of small-amplitude bars is tested for:

- The influence of numerical diffusion
- The influence of the horizontal eddy viscosity
- The influence of lateral grid resolution (on higher-mode bars)

Numerical diffusion can be introduced by the 'upwind' scheme for the morphological updating procedure (Deltares, 2011), see Appendix G. This scheme is used to set the bed-load transport at the velocity points equal to the bed-load transport at the centre of the 'upwind' cell. The advantage of this approach is that the bed remains stable. Numerical diffusion can be avoided by using the 'central' scheme. This scheme sets the bed-load transport at the velocity points equal to the average of the bed-load transport at the centres of the cells on both sides. The difference in bed-load transport prediction by both schemes can be seen in Figure 5-1. The figure shows a longitudinal cross-section of a hand-made alternate-bar pattern (green), along with the magnitude of the bed-load transport (blue). The 'upwind' scheme (dotted line) shifts the bed-load curve in the

downstream direction. The shift is equal to half the longitudinal grid size (dx/2). More about this procedure can be found in Appendix G.

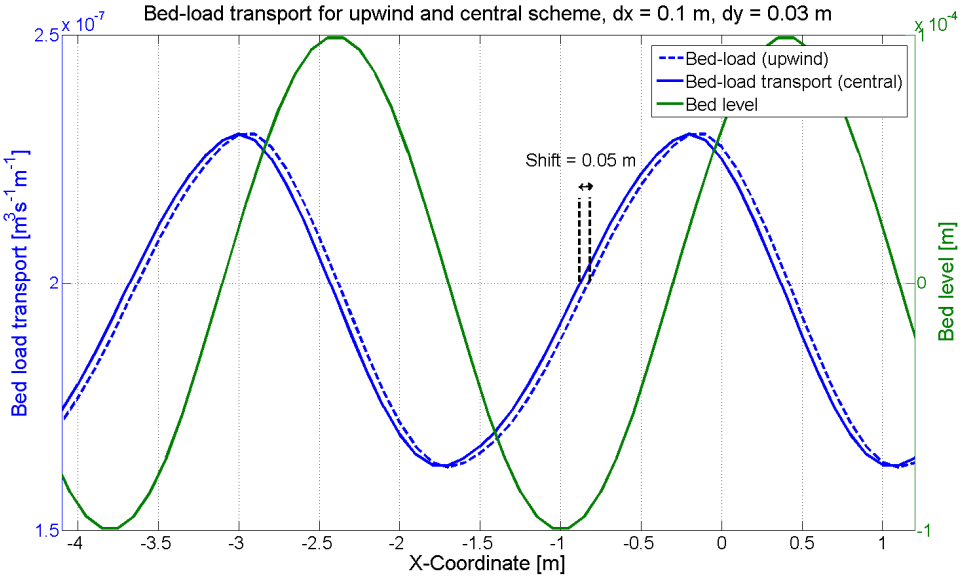

Figure 5-1: Effect of upwinding

The horizontal eddy viscosity is a measure for processes which cannot be taken into account directly by the grid. Examples are subgrid-scale turbulence and dispersion for depth-averaged simulations. Generally, one can state that the eddy viscosity has a damping effect on the simulation. During a Horizontal Large Eddy Simulation (HLES) it appeared that the horizontal eddy viscosity should be in the order of 10^{-5} m^2/s, which is a small value, but common for simulations on laboratory scale. For reasons of stability, however, the eddy viscosity had to be increased to 0.01 m^2/s. For more information about the horizontal eddy viscosity one is referred to Appendix C.

Method of analysis

The simulations for small-amplitude bars are done with the same settings as the simulations in section 4.3.3, see Table 5-1. Only the scheme for the morphological updating procedure, the value of the horizontal eddy viscosity and the lateral grid resolution are varied. The discharge and therefore also the half-width-to-depth ratio is equal in all simulations.

Table 5-1: Characteristics of simulation S7-S105, see Table C-4 in Appendix C for more information

Constant			Variable				
β [-]	**A_{sh} [-]**	**h_0 [m]**	**Domain**	**ν_H [m^2/s]**	**Morphological updating scheme**	**L_L [m]**	**Mode [-]**
24.3	1.9	0.0001	3n / 3l	$3*10^{-5}$ – 0.01	'upwind' / 'central'	0.7 - 30	1-3

5.2.2 Influence on the wave length

Possible reasons for discrepancy

Van der Meer et al. (2011) observed that the wave length of alternate bars for β>13, was much shorter than predicted by linear theory. They proposed that again numerical diffusion (Appendix G) could be the reason for the shortening of bars. The influence of the horizontal eddy viscosity is not investigated, because the results of section 5.3.1 show that the wave length of the most-unstable bar does not differ for different values of ν_H.

Finding the wave length

The influence of different contributors to the wave length is investigated for free and forced bars. It is common thought that the wave length of free bars is related to the most-unstable bar. To trigger free-bar formation, the initial bed was randomly perturbed. To trigger forced bars, a groyne, which blocked half the channel, was used to generate a non-migrating alternate-bar pattern, see Figure 4-4.

Method of analysis

The influence of numerical diffusion is investigated by varying the scheme for the morphological updating procedure ('upwind' vs 'central'). This investigation is done for different discharges, and subsequently different β values. The settings of the simulations for this analysis can be found in Table 5-2. The simulations are continued until an equilibrium bed topography has been reached.

Table 5-2: Characteristics of simulations R5-R24, see Table C-3 in Appendix C for more information

Constant					Variable		
Domain	**Boundary conditions**	**ν_H [m^2/s]**	**A_{sh} [-]**	**Initial bed**	**β**	**k_s [m]**	**Morphological updating scheme**
3n	Q-WL	0.01	1.9	Randomly perturbed +/- 0.1 mm	9.1 – 21.2	0.009 - 0.022	'upwind' / 'central'

5.2.3 Influence on the point of resonance

Possible reasons for discrepancy

The resonance half-width-to-depth ratio was both in this research and in the research of Van der Meer et al. (2011) higher than predicted by linear theory. Van der Meer et al. suggested that numerical diffusion, entered via morphological updating procedure, could have caused β_{res} to be higher than the theoretical value. I also added horizontal eddy viscosity as a possible contributor to the difference between the analytical and numerical model.

Finding the point of resonance

According to linear theory, under resonant conditions a certain alternate-bar mode is either non-migrating and non-amplifying (Vanzo et al., 2011). By imposing small-amplitude bars, this resonance point can be found.

Method of analysis

The settings for the simulations to analyse the influence of β_{res} can be found in Table 5-3.

Table 5-3: Characteristics of simulations S106 – S172, see Table C-4 in Appendix C for more information

Constant				Variable			
Domain	**A_{sh} [-]**	**h_0 [m]**	**Mode [-]**	**β [-]**	**ν_H [m^2/s]**	**Morphological updating scheme**	**L_L [m]**
3n	1.9	0.0001	1	10-19.5	$6*10^{-5}$ – 0.01	'upwind' / 'central'	8.5-10

The influence of the horizontal eddy viscosity is discovered by finding the point of resonance for different values of the horizontal eddy viscosity. Here it was possible to use horizontal eddy viscosity values up to $6x10^{-5}$ m^2/s, notwithstanding the statements in section 4.2.1.5 that a viscosity of 0.01 m^2/s is needed to ensure stability. Numerical instability only occurred when the water depth was relatively small. Because this specific research is on small-amplitude bars, the water depth is everywhere still relatively large, so no instability occurs for low viscosity.

5.3 Results

The methodology applied to analyse the influence of numerical properties of the model, is described in section 5.2. In this chapter, the results of the analysis of numerics can be found. First, I discuss the influence of numerics on the behaviour of small-amplitude bars, then on the wave length of the alternate bar and finally on the point of resonance.

5.3.1 Influence on small-amplitude bar behaviour

5.3.1.1 Influence of numerical diffusion

Amplification rate

The observed amplification rates for the 'central' and 'upwind' routine can be found in Figure 5-2. As already shown in section 4.3.3, the observation for first-mode bars complies with linear theory, in case of the 'central' routine. The curves for the 'upwind' and 'central' method start to deviate for bars shorter than 2.5 m (dimensionless wavenumber > 0.8). The consequence of 'upwinding' is that the top of the amplification curve (the wavenumber of the most-unstable bar) is shifted to the left, towards longer bars. One might therefore expect bars to be longer in case of 'upwinding', which matches the observations in section 5.3.2. The higher the mode, the shorter the most-unstable bar. Therefore, numerical diffusion has a larger effect on higher-mode bars.

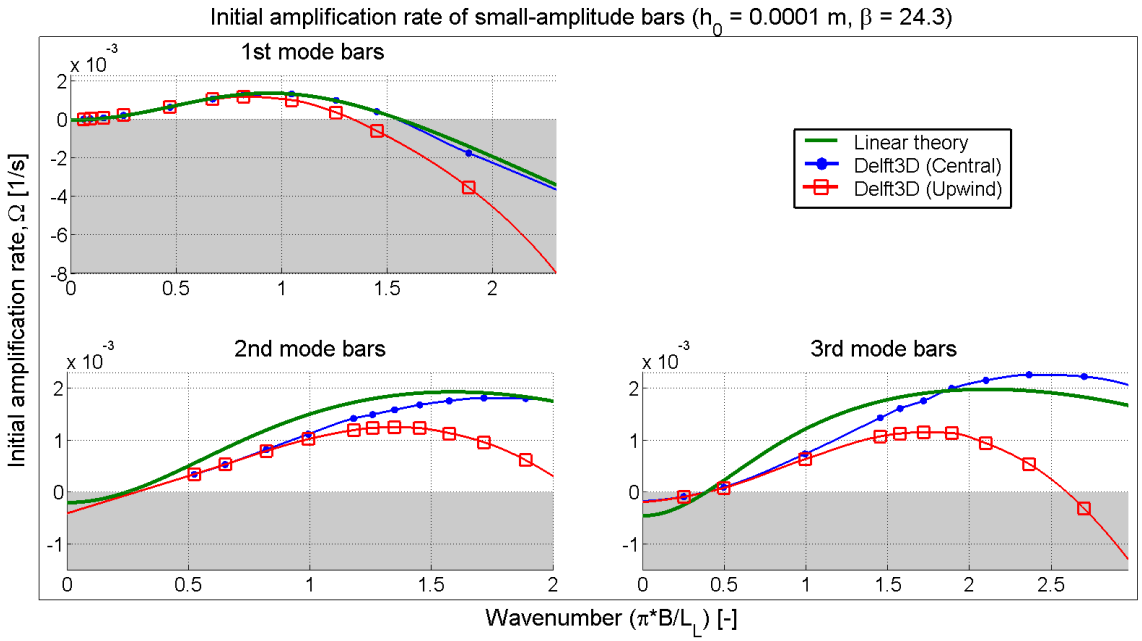

Figure 5-2: Initial amplification rate of small-amplitude bars, 'upwind' and 'central' method

Migration rate

In Figure 5-3, one can see the migration rate of first-mode bars during the simulation with the 'central' and 'upwind' methods, together with the analytical prediction. It becomes clear that the

migration rate is not really influenced by the choice for the bed-load procedure. Numerical diffusion, apparently, does not have a significant influence on the migration rate of small-amplitude bars.

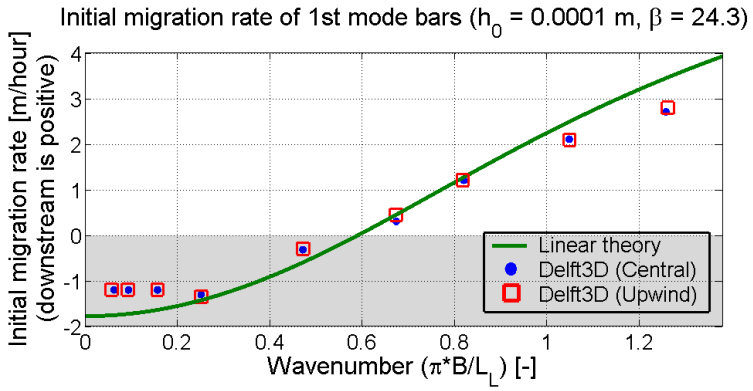

Figure 5-3: Migration rate of small-amplitude bars, 'upwind' and 'central' approach

Physical explanation

The behaviour of bars can be explained by the phase lag between the bed topography and the bed-load transport, as explained in section 2.2.

The phase lag depends on the longitudinal wave length of the alternate bar, as can be seen in Figure 5-4. This figure is based on the output of the simulations, which are used in this section. The figure also shows the difference in phase lag between the 'central' and 'upwind' method. This can be explained by the fact that the bed-load transport, predicted with the 'upwind' routine, is shifted in the downstream direction, see Figure 5-1. This shift can be seen as an added positive phase lag, later referred to as δ_{upw}. The shift of the bed-load curve, predicted with the 'upwind' routine, is always equal to dx/2. The phase lag due to the 'upwind' scheme is therefore proportional with $1/L_L$. The shorter the bar, the larger the effect of upwinding. The shift of the bed-load curves between the 'upwind' and 'central' method can be reduced by reducing the longitudinal grid size.

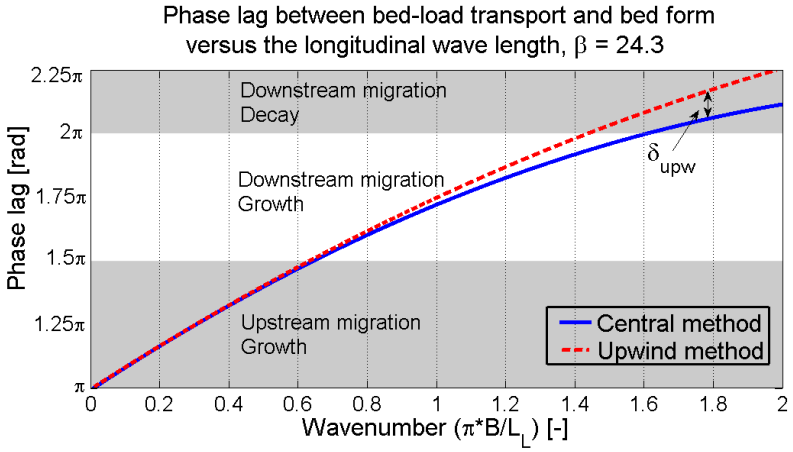

Figure 5-4: Phase lag between bed-load transport and bed topography versus L_L

5.3.1.2 Influence of horizontal eddy viscosity

In Figure 5-5, one can see the observed amplification rate of small-amplitude bars for different values of ν_H. It appears that the amplification rate of alternate bars is inversely proportional to ν_H.

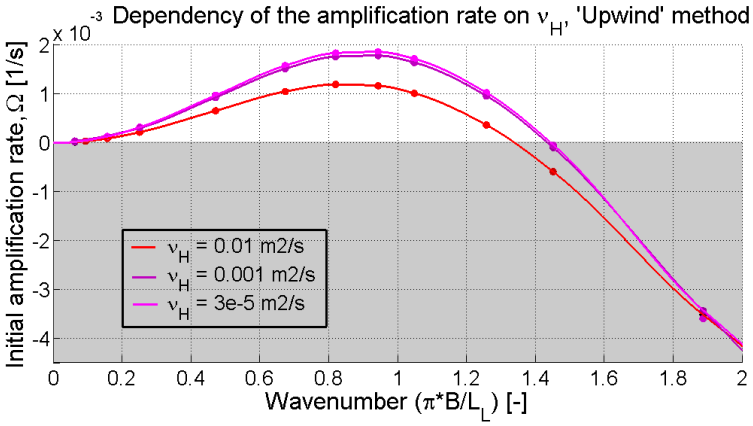

Figure 5-5: Dependency of the amplification rate on ν_H, 'upwind' method

Although the horizontal eddy viscosity has a quantitative effect on the amplification rate of small-amplitude bars, the shape of the curve is preserved. Also the wavelength, corresponding with the most-unstable bar, is equal for all values of ν_H. The eddy viscosity has therefore mainly an effect on the time scale of alternate-bar formation and not so much on the spatial properties of the small-amplitude alternate-bar pattern.

Physical explanation

An extensive explanation can be found in Appendix G.

The horizontal eddy viscosity has a damping effect on hydrodynamic perturbations. In Figure 5-6, one can see the effect on the velocity perturbation. For $\nu_H = 0.01$ m^2/s, the velocity has a smaller variation of magnitude as for $\nu_H = 3*10^{-5}$ m^2/s. Because the bed-load transport is proportional to the velocity to a certain "power", the bed-load transport variation is larger for a lower ν_H. As explained in section 2.2, the bed level change rate is dependent on the spatial derivative of the bed-load transport. A larger variation will lead to a larger ds/dx, and therefore to a larger amplification rate.

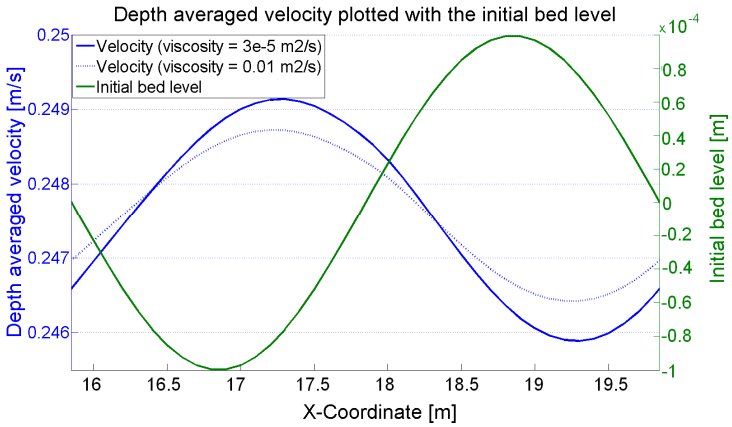

Figure 5-6: Velocity distribution over an alternate bar for different values of v_H

5.3.1.3 Influence of lateral grid resolution

In section 5.3.1.1 one can observe that the growth rate of small-amplitude first-mode bars is well predicted by linear theory. The behaviour of second- and third-mode bars in the numerical model, on the contrary, does not match linear theory. One would expect this difference to be caused by the lateral resolution, for the higher the bar mode, the less grid cells per wave length in the lateral direction. In order to investigate the influence of lateral resolution, Domain 3n was refined with a factor 2, only in the lateral direction, which resulted in Domain 3l. In Figure 5-7, one can see that the larger transverse resolution gives almost the same result as the simulations with the normal grid. Only for the third-mode bars a small difference can be seen for the very short bars (L_L < 0.9 m), but still the curve does not fit linear theory. The difference between linear theory and the numerical model for the amplification rate of higher-mode bars can therefore not be explained by a lack of lateral resolution.

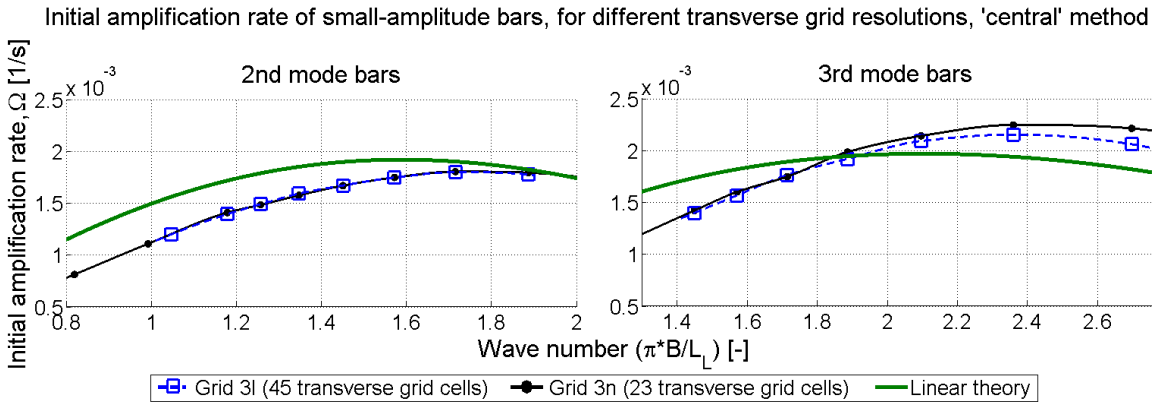

Figure 5-7: Initial amplification rate for grids with a different lateral resolution

5.3.2 Influence on the wave length

In section 5.3.1, I have already found that horizontal eddy viscosity has no effect on the wave length of the most-unstable bar. Therefore, the influence of the horizontal eddy viscosity is not investigated in this chapter. Here only the influence of numerical diffusion is tested.

Developed free bars

In Figure 5-8 (left), one can see the wave length of free bars for both the 'upwind' and 'central' scheme for the morphological updating procedure. The figure shows the observed wave length and the uncertainty, due to the grid resolution. It appears that the wave length of free bars is about 4% larger for the 'upwind' routine for bed-load transport, than for the 'central' scheme. This complies with the influence on small-amplitude bars, as discussed in section 5.3.1.

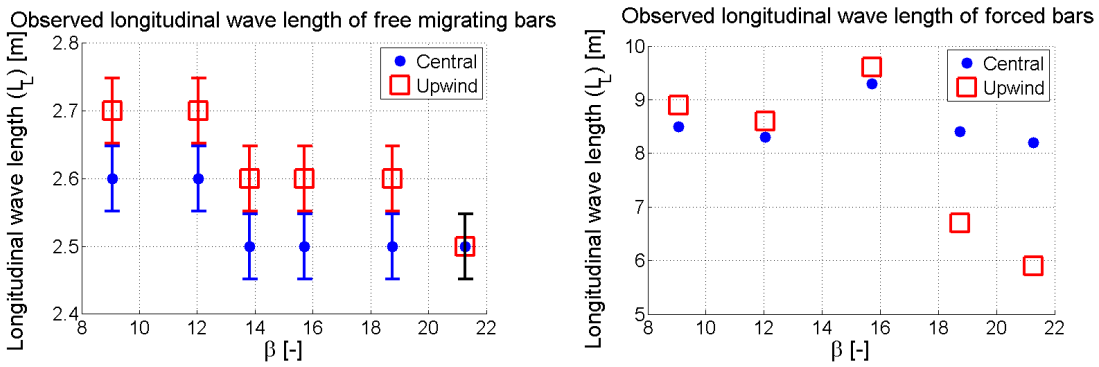

Figure 5-8: Longitudinal wave length of free migrating bars (left) and forced bars (right) versus β, for the 'upwind' and 'central' method

Forced bars

Figure 5-8 (right) shows the observed forced-bar length for both the 'upwind' and 'central' method. In this picture, the uncertainty due to the grid resolution is not shown, because it is very small relative to the scale of the vertical axis. The wave length of forced bars is quite constant for different β values for the 'central' method. The 'upwind' scheme predicts the bars to be about 3% longer for small values of β (β < 16). For larger width-to-depth ratios, the wave length of the 'upwind' forced bar shows a significant decrease. This forced-bar 'behaviour' was also observed by Vanzo et al. (2011) and Van der Meer et al. (2011).

The reason for this sudden shortening of bars is that the bar tops became inactive, due to a very small waterdepth, before it was fully developed. The result of this sudden drying was that the bar top became inactive and the bar non-migrating, whereas its wave length was still relatively short. In the simulations with the 'central' method this drying does not occur for these β values. I stress that I do not know whether the results of Vanzo et al. (2011) were also affected by 'upwinding'.

It appears that the bars in the 'upwind' simulations have a different spectral composition than in the 'central' simulations. The bars in the 'upwind' simulation consist of a relatively large first mode and relatively small higher modes. For example, Figure 5-9 shows the relative "power" spectrum of the free-bar pattern of simulation R17 (the other simulations show the same trend). Relative "power" means the absolute "power" (bed level divergence squared) of a specific mode divided by the total "power" of the bar pattern. The figure clearly shows that the contribution of the first mode is larger for the 'upwind' alternate bars and that the contribution of the higher modes is less. It is important to note that the total "power" was equal for the alternate bars compared. The second mode mainly represents a 'central' longitudinally uniform deposit. In the 'upwind' simulations the sediment is

therefore more deposited near the banks. This explains why bars in case of the ‘upwind’ method can be emerged from the waterlevel, whereas the bar top is still submerged in case of the ‘central’ method.

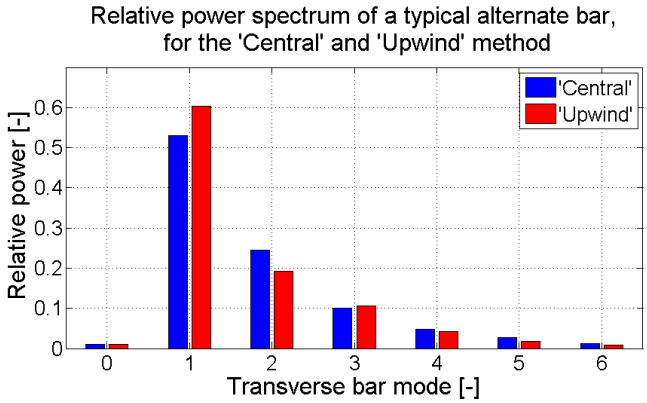

Figure 5-9: Relative “power” spectrum of a typical alternate bar; influence of ‘upwinding’

5.3.3 Influence on the point of resonance

5.3.3.1 Influence of numerical diffusion

The method to find the point of resonance is described in section 5.2.3. In Appendix F this procedure of finding the point of resonance is visualised for the ‘upwind’ and ‘central’ method separately. In Figure 5-10, one can see the observed points of resonance for different values of the horizontal eddy viscosity. The point of resonance for the ‘upwind’ method is in all cases slightly lower than the one for the ‘central’ method. So contrary to the hypothesis of Van der Meer et al. (2011), the point of resonance is not significantly sensitive to numerical diffusion. Expected was that the β_{res} should be higher for the ‘upwind’ method than for the ‘central’ method, the opposite is even shown.

Physical explanation

Because the point of resonance is associated with long alternate bars (≈ 9 m), the δ_{upw} (extra phase lag between the bed topography and the bed-load transport, due to upwinding) is relatively small. The difference between the resonance points of the ‘upwind’ and ‘central’ scheme is smaller if the grid is refined in the longitudinal direction, for the shift is proportional to the longitudinal grid size.

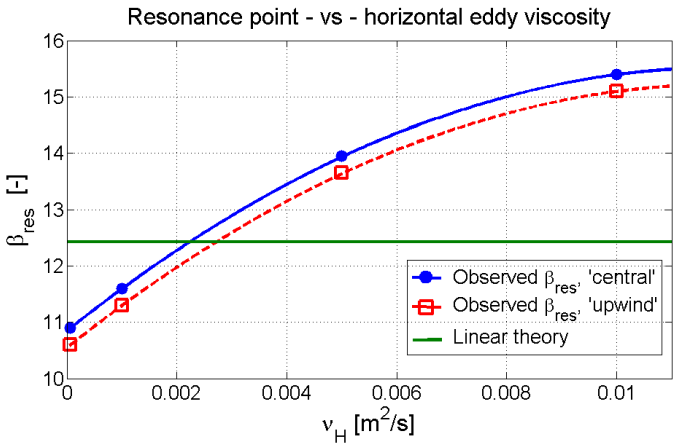

Figure 5-10: Analytical and observed numerical values for β_{res}

5.3.3.2 Influence of horizontal eddy viscosity

In Figure 5-10, one can observe the relation between the point of resonance and the horizontal eddy viscosity. It shows that the resonance point is significantly dependent on the horizontal eddy viscosity. According to the HLES simulation, see chapter C.2, the viscosity should be in the order of 10^{-5} m^2/s. For stability reasons, the viscosity applied, in the simulations to investigate the development of upstream alternate bars, is 0.01 m^2/s. This choice has a significant implication for the transition between sub- and super-resonance conditions. As expected by Van der Meer et al. (2011) and after validating the model, β_{res} is overpredicted by the model for horizontal eddy viscosity values of about 0.01 m^2/s.

Discussion

It is not clear how to explain the observed relation between the horizontal eddy viscosity and the point of resonance. On one hand, one can argue that viscosity exercises a (positive) damping on the system, as shown in 5.3.1.2. According to Mosselman et al. (2006), one can argue that super-resonant conditions correspond to negative damping coefficients and sub-resonant conditions with positive ones. Considering this reasoning, one can argue that a higher value of the viscosity leads to a more positive damped system, so to a higher β_{res} value.

On the other hand one can argue that the adaptation length for flow is inversely proportional to the horizontal eddy viscosity ($\lambda_w \sim 1/\nu_H$), the higher the viscosity, the shorter the adaptation length. Resonance occurs, according to Struiksma et al. (1985), at a certain interaction parameter λ_s/λ_w, see Figure 5-11. If this 'resonant' interaction parameter is supposed to be not dependent on ν_H, and the interaction parameter is proportional to ν_H, one would suggest that a large ν_H leads to a system that tends to super-resonant conditions. And thus to a smaller β_{res} value.

The first way of reasoning complies with the observations, whereas the second one contradicts the observations. At the moment of completing this report I have not been able to determine which reasoning is correct.

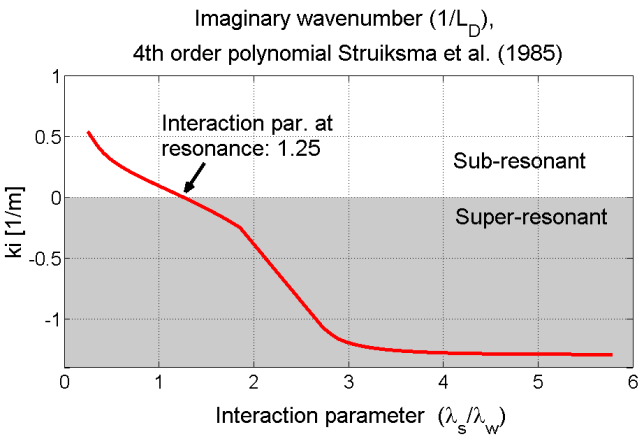

Figure 5-11: Prediction of resonance point according to fourth order polynomial Struiksma et al. (1985)

6 Analysis of upstream bar development

6.1 Objective

Previous linear analyses and laboratory experiments have shown that under super-resonant conditions both downstream and upstream of a geometrical perturbation bars will arise. However, they did not investigate in detail how these upstream alternate bars develop.

The objective of this chapter is:

"Acquiring a better understanding of the development process of alternate bars, upstream of a bend under super-resonant conditions"

6.2 Methodology

Interesting issues regarding the development of bars in super-resonant conditions are:

- Influence of the bend
- Direction of migration
- Instability of the bed

This section discusses the method of investigation.

6.2.1 Influence of the bend

Hypothesis

Zolezzi & Seminara (2001a) predicted via linear theory that in super-resonant conditions the bend will influence the bed upstream of the bend (upstream influence). Therefore, the hypothesis is that the bend will have an influence on the formation process of alternate bars upstream of the bend under super-resonant conditions ($\beta > \beta_{res}$). In that case, long bars will be generated at the bend and will migrate in the upstream direction.

Method of analysis

In the literature, in most numerical simulations alternate-bar formation is triggered by a perturbed inflow discharge, or a perturbed bed (Crosato et al., 2011, Mosselman et al., 2006). To observe the development solely caused by the presence of the bend, first a simulation without any perturbation is carried out: simulation R3.

Then a simulation is carried out, in which the upstream inflow discharge is randomly perturbed, with a maximum of 1% of the discharge, simulation R1. It is analysed whether the same development occurs with and without inflow perturbation.

Finally a comparison is made between the development of alternate bars in a straight flume and a perturbed inflow discharge, simulation R2. Through doing this comparison I find that in case of a boundary disturbance, the bend does not show an influence.

The main characteristics of the simulation, described above, are summarized in Table 6-1.

Table 6-1: Characteristics of simulation R1, R2, R3a, R3b, see Table C-3 in Appendix C for more information

RunID	Domain	β	Boundary conditions	k_s [m]	ν_H [m^2/s]	A_{sh} [-]	Morphological updating scheme	Initial bed
R1	2n	24.3	Q_P-WL	0.008	0.01	1.9	'upwind'	Flat
R2	**3n**	24.3	Q_P-WL	0.008	0.01	1.9	'upwind'	Flat
R3a	2n	24.3	**WL-WL**	0.008	0.01	1.9	'upwind'	Flat
R3b	2n	24.3	**Q-WL**	0.008	0.01	1.9	'upwind'	**End R3a ***

*Simulation R3b started with the developed bed topography of R3a, from the moment that the backwater curve reached the inflow boundary

6.2.2 Direction of migration

Definition of migration and propagation

In this section, two types of migration are discussed: the migration of individual bars and the propagation of a bar pattern. It is for example possible that an individual bar is migrating in the downstream direction, whereas the pattern is propagating in the upstream direction. The word 'migration' in this report will only refer to individual bars, whereas 'propagation' will always refer to a bar pattern.

Hypothesis

The expectation is that during super-resonant conditions immediately upstream of the bend curvature discontinuity an alternate bar will develop. Subsequently more upstream of this alternate bar a new alternate bar will be generated. The migration of (sufficiently-long) alternate bars under super-resonant condition is supposed to be in the upstream direction. Higher mode bars can be still in sub-resonant conditions, whereas the first-mode bar is in super-resonant conditions. The higher-mode bars are therefore supposed to be migrating in the downstream direction as long as they are in the sub-resonant regime.

Method of analysis

As for the analysis of the bend influence, a distinction is made between disturbance-driven and bend-driven alternate-bar development. The migration of individual bars and propagation of the bar pattern is therefore investigated in the case that no perturbation is applied (R3) and in the case that the discharge at the inflow is perturbed (R1). For the main characteristics of the simulations one can see Table 6-1. The migration direction will be shown with a migration diagram. The propagation direction of the bar pattern is analysed with Fourier transforms, see Appendix E. This is done by dividing the upstream straight reach in sections of 4 m length, see Figure 6-1. For every section the

development of the "power" and amplitude of the different bar modes is analysed with Fourier transforms.

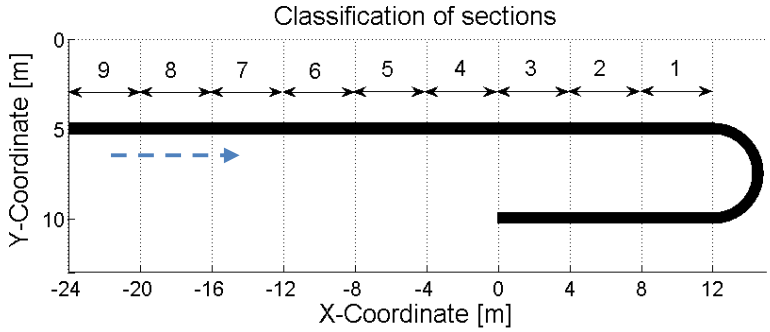

Figure 6-1: Locations of sections of upstream river reach

Non-linear effects influence the migration rate and migration direction of alternate bars. This is shown by imposing alternate bars with a wave length of 7.5 m, but different initial amplitudes, on an initially flat bed. These simulations have the following settings:

Table 6-2: Settings of simulations S173 – S174, , see Table C-4 in Appendix C for more information

RunID	Domain	β [-]	v_H [m^2/s]	A_{sh} [-]	Morphological updating scheme	L_L [m]	h_0 [m]	Mode [-]
S106	3n	24.3	0.01	1.9	'central'	7.5	**0.0001**	1
S107	3n	24.3	0.01	1.9	'central'	7.5	**0.008**	1

6.2.3 Bed instability

The focus regarding bed instability will be on the start of bar development. Which bar appears first when the bed is unstable and can this initial bar pattern be predicted with linear theory?

Instability in a numerical model needs to be triggered. This can be done by either applying a disturbed bed level, or by applying a disturbance at the upstream boundary. For this research both approaches are used.

Hypothesis

According to Blondeaux and Seminara (1985), Zolezzi and Seminara (2001b), Vanzo et al. (2011) and many others, every specific bar has its own amplification rate. The bar with the highest amplification rate is called the most-unstable bar. It is expected that if a flat bed is unstable, the most-unstable bar will become apparent first. In numerical modelling, instability of the bed should be triggered by a boundary disturbance or a bed disturbance. The hypothesis is that in case of instability of the bed, the most-unstable mode will emerge first

Method of analysis

Bed instability for this specific issue is triggered in two ways, by perturbing the discharge at the inflow boundary (R1) and by perturbing the initial bed level with a random perturbation of about 1%

of the water depth (R4). The initial bar pattern is analysed with Fourier transforms and compared to the most-unstable bar according to the analysis of small-amplitude bars, see Figure 5-2. The main characteristics of R1 can be found in Table 6-1, the characteristics of R4 can be found in Table 6-3.

Table 6-3: Characteristics of simulation with boundary disturbance (R4) , see Table C-3 in Appendix C for more information

RunID	Domain	β	Boundary conditions	k_s [m]	v_H [m^2/s]	A_{sh} [-]	Morphological updating scheme	Initial bed
R4	2n	24.3	Q_P-WL	0.008	0.01	1.9	'upwind'	**Random pert. +/- 0.1 mm**

6.3 Results

6.3.1 Influence of the bend

The goals and hypothesis for this specific section can be found in section 6.2.1. Also the way the results in this chapter were gathered and the characteristics of the simulations, can be found in that section. A description of simulations R1 and R3a can be found in Appendix D.

In this section, a distinction is made between bend-driven development and disturbance-driven development.

6.3.1.1 Bend-driven development

The influence of the bend is clearly observed if no disturbance is applied at the upstream boundary. Simulation R3a is carried out to show this influence. Immediately from the start of the simulation a scour hole develops at the inner part of the bend entrance. The bend causes the flow to be concentrated at the inner part of the bend entrance. Subsequently the flow at the outer part of the bend entrance decreased. This leads to erosion at the inner part and sedimentation in the outer part. This erosion and sedimentation pattern moves in the upstream direction. The bend clearly shows an influence on the bed upstream of the bend (upstream influence). The upstream migration of this pattern can be explained by the fact that sufficiently-long small-amplitude bars migrate in the upstream direction under super-resonant conditions. The observation complies with the explanation of upstream influence by Zolezzi and Seminara (2001a).

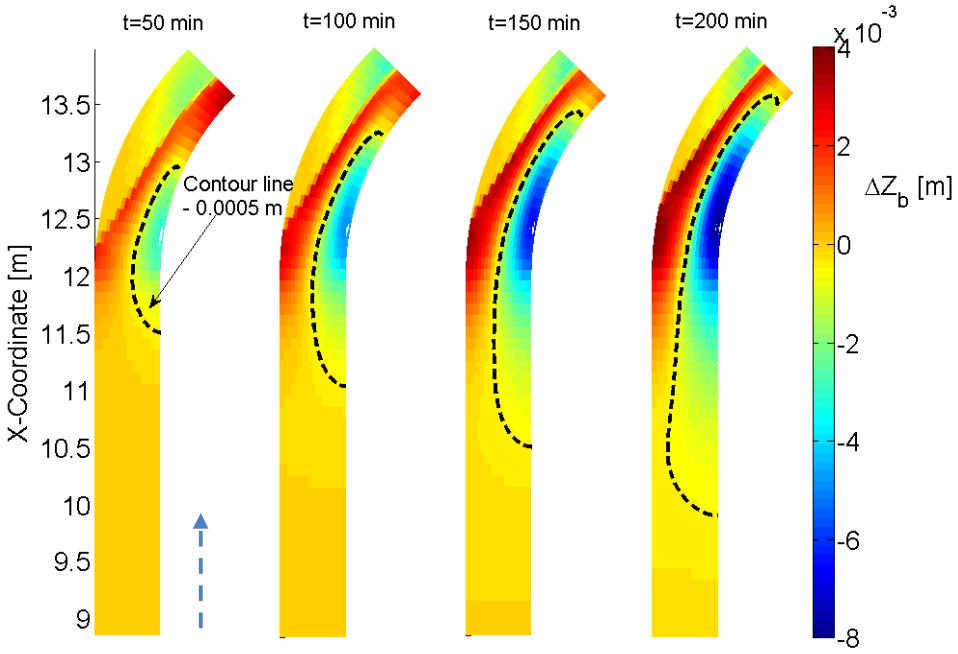

Figure 6-2: Development of alternate bar at bend entrance

In Figure 6-3, one can see the bed level change in the upstream straight reach for t =550 min to t = 950 min. During the first 600 min hardly any ripple or bar can be seen (besides the long scour hole immediately upstream of the bend). After about 600 minutes higher-mode bars start to develop at the edge of the scour hole, see Figure D-7 in Appendix D. These second-mode bars travel in the downstream direction and merge into first-mode, alternate, bars.

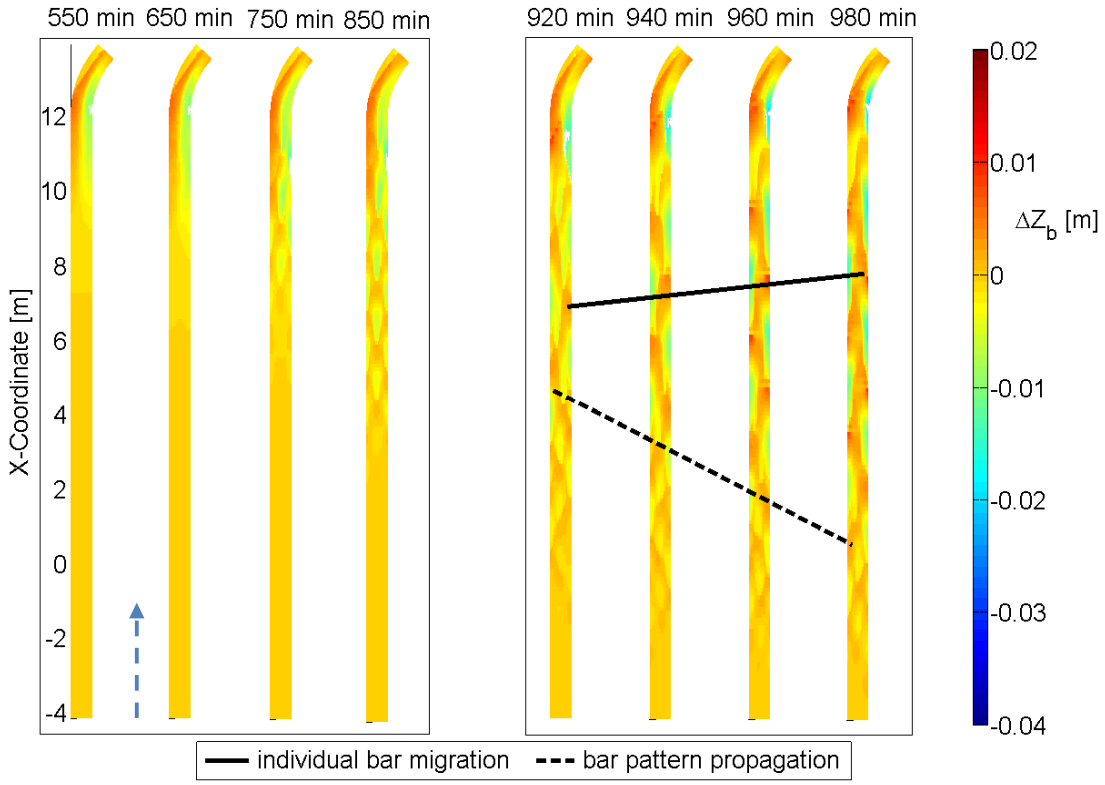

Figure 6-3: Cumulative sedimentation/erosion R3a

6.3.1.2 Disturbance-driven development

Simulation R1 has, apart from the disturbance at the upstream boundary, the same settings as simulation R3a. This simulation is analysed below and compared to simulation R2 (same settings as R1, but the bend is absent in the domain).

Initially at the bend entrance

Due to the discharge perturbation at the inflow boundary a second-mode pattern develops at the inflow boundary that migrates in the downstream direction, to the bend entrance. This disturbance-driven bar pattern reaches the bend entrance after 240 min of simulation. Before that happens, the same development at the bend entrance can be seen, as visualised in Figure 6-2.

After the disturbance-driven bar pattern reached the bend

When the second-mode bars reach the bend, alternate bars form upstream of the already formed scour hole. To judge the influence of the bend, the simulation with bend is compared to a simulation in which the bend is absent (R2). In Figure 6-4, one sees the development of bars between X = -4 m and X = 14 m. The similarity, visualized with the black ellipses, between the two different runs, show that disturbance-driven alternate bars also develop without the presence of a bend. Alternate bars between X=-4 m and X=2 m develop even earlier for the run without a bend. But apart from the time lag, the same way of development occurs in the straight model as in the model with bend. The blue ellipses show that the strongest alternate-bar development takes place in the same section.

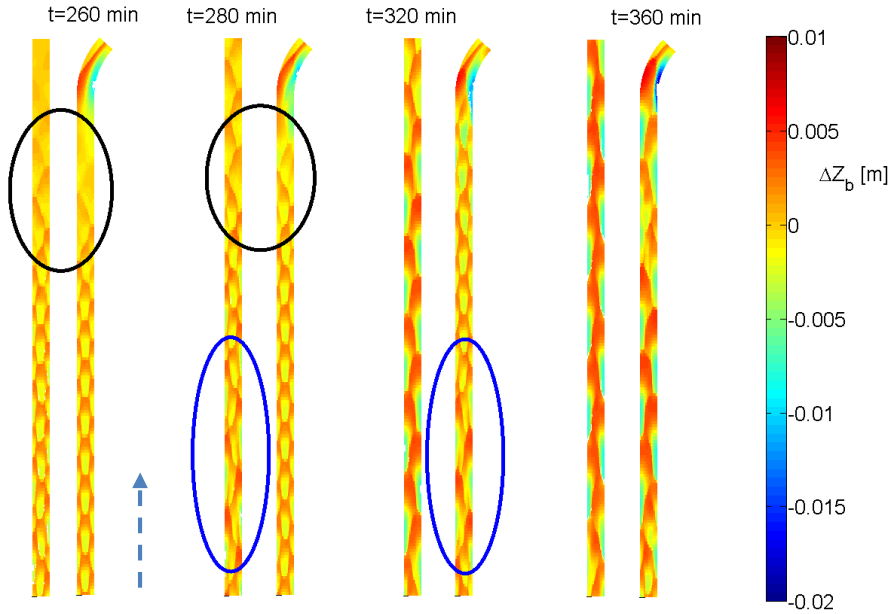

Figure 6-4: Comparison between simulation with and without bend

6.3.1.3 Comparison between equilibrium bed topographies

The equilibrium bed topographies of the three simulations are compared in this section.

Figure 6-5 shows a visual comparison. The bed topographies are also analysed with Fourier Transforms, see Appendix E. The main characteristics of the Fourier analysis can be found in Table 6-4. It can be concluded that the equilibrium topographies of R1 and R2 are very similar. Therefore one can state that in case of disturbance-driven bar formation, the bend has no significant influence.

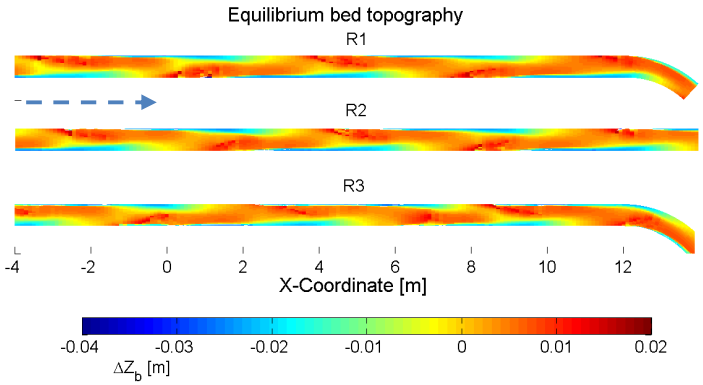

Figure 6-5: Equilibrium bed pattern after 32 hours for R1, R2 and R3

A larger difference can be observed between R1 and R3, but still the main alternate bar characteristics (wave length, amplitude of the 1-1 mode) are very similar. The largest difference between the equilibrium bed topography of both simulations is the difference in amplitude of the 0-0 mode. The 0-0 mode is a uniform displacement of the bed. The bed in R3 is uniformly lowered, the reason for this is that, during R3a, the incoming bed-load transport was less than the bed-load transport at the downstream boundary, so a net export of sediment occurred (Figure 6-6).

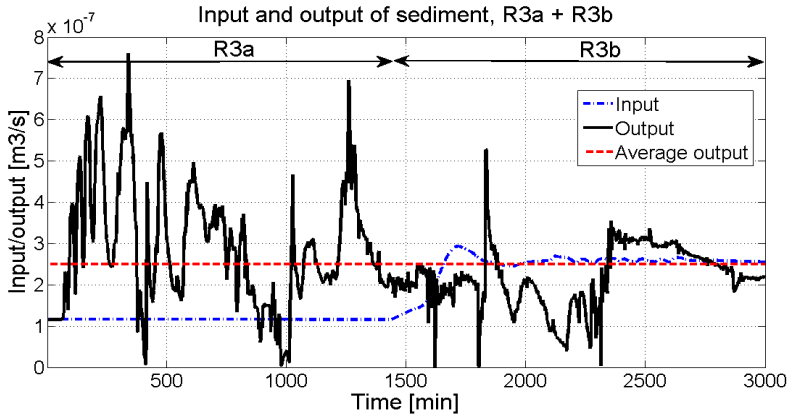

Figure 6-6: Input and output of sediment, simulation R3a and R3b

Table 6-4: Comparison between equilibrium topography of R1, R2 and R3b

	R1	***R2***	***Difference R1 – R2 [%]***	***R3***	***Difference R1 – R3 [%]***
Wave length of first-mode bar [m]	7.1	7.1	0	7.3	+3.5
Total "power"	0.223	0.228	+2.0	0.224	+0.4
Amplitude 1-1 mode [mm]	19.9	20.0	+0.8	18.3	-7.6
Amplitude 0-2 mode [mm]	9.8	10.3	+5.5	8.6	-12.2
Amplitude 1-3 mode [mm]	8.8	8.6	-1.4	6.4	-27.3
Amplitude 0-0 mode [mm]	1.3	1.3	+0.5	5.1	+304.2

6.3.1.4 Conclusions

The following conclusions can be drawn regarding to the influence of the bend:

- Disturbance-driven alternate-bar formation is dominant over bend-driven alternate-bar formation, because bend-driven alternate-bar formation takes place on a much longer timescale than boundary-driven alternate-bar formation.
- If no disturbance is applied, the bend will influence the bed upstream of the bend under super-resonant conditions. The resulting equilibrium alternate-bar pattern does not significantly differ from the equilibrium alternate-bar pattern, generated by a boundary disturbance.

6.3.2 Direction of migration

The goals and hypothesis for this specific section can be found in section 6.2.2. Also the way the results in this chapter were gathered and the characteristics of the simulations can be found in that section.

6.3.2.1 Migration of individual bars

Observations

In Figure 6-7, one can see the migration diagrams of the alternate-bar peaks of simulation R1 and R3a. The figure shows that the bar peaks migrated invariably in positive X-direction, which is in the downstream direction. So contrary to the hypothesis, no bars were observed to migrate in the upstream direction under super-resonant conditions. The left picture shows the development of alternate bars till the bars emerged from the water level, the right picture only shows the migration of bars in the initial stage of the simulation. Some strange discontinuities can be seen in the right figure (marked with red ellipses). The migration of bar tops in that simulation sometimes suddenly ceased and after some time resumed. This has to do with the fact that the flow fluctuated between sub- and super-critical in those periods. More about this can be found in Appendix D.

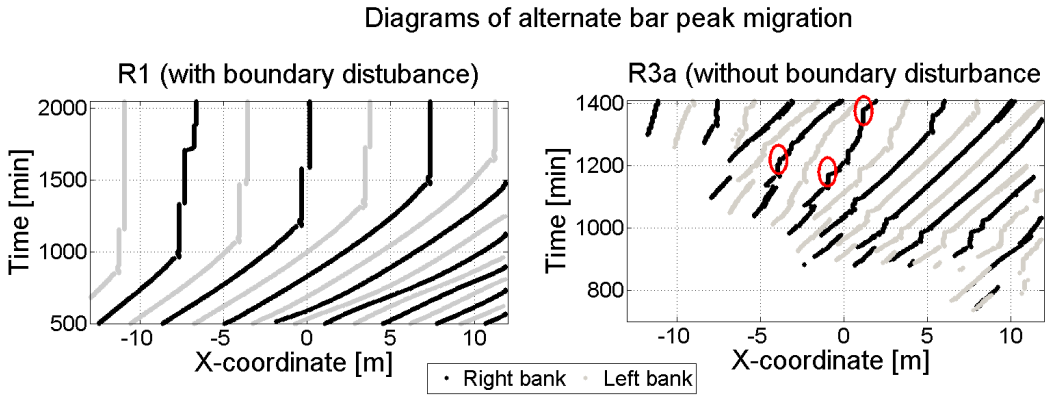

Figure 6-7: Diagrams of alternate-bar peak migration

Explanation (non-linear effects)

In Figure 6-8, one can see the migration direction of imposed alternate bars, with an initial amplitude of 0.0001 m (left), and 0.008 m (right). In linear theory, the migration rate and direction is not dependent on the bar amplitude. However, the figure shows that the migration rate and direction is dependent on the bar height. The right picture shows clear non-linear effects. This might explain the absence of bars migrating in the upstream direction in simulations R1 and R3.

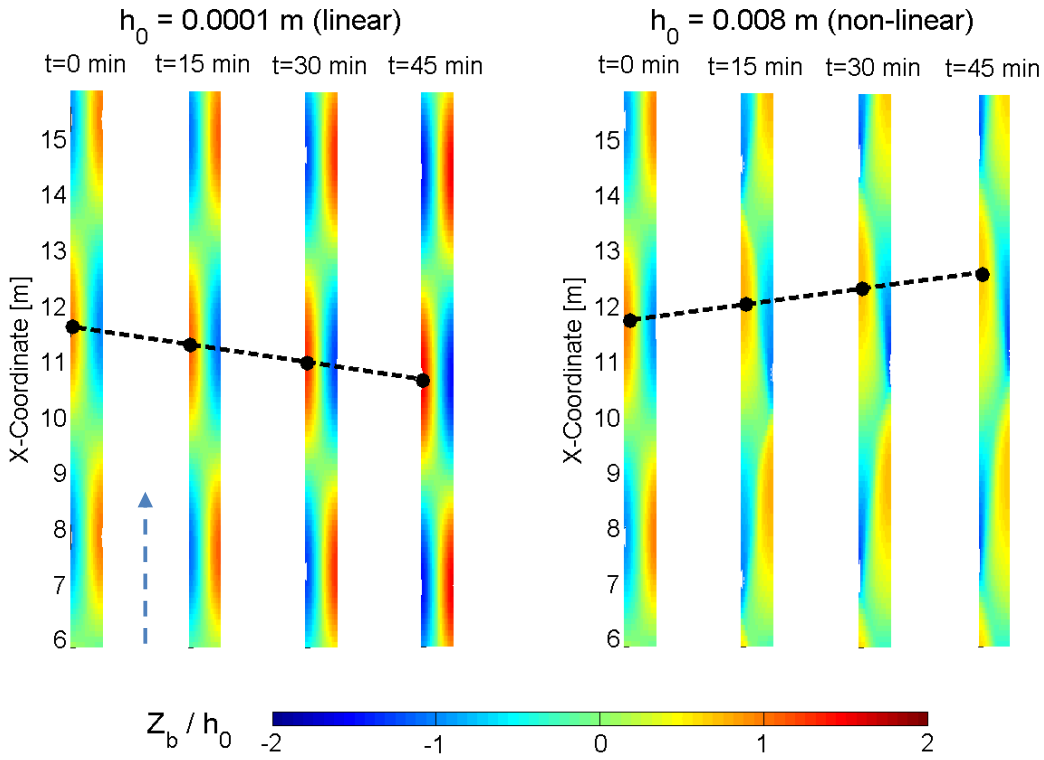

Figure 6-8: Migration direction for different initial amplitudes

6.3.2.2 Propagation of bar patterns

The direction of propagation is analysed with Fourier transforms as described in section 6.2.2. In section 6.2.1, one can see that the influence of the bend is only visible if no disturbance at the upstream boundary is applied. Otherwise the disturbance-driven development will be dominant. It also appears that the propagation direction of bar patterns is dependent on the presence of a boundary disturbance. Therefore, the propagation will be discussed for the situation that no disturbance is applied and for the situation with a boundary disturbance.

Bend-driven development

In Figure 6-9, one can see the amplitude development of the first mode in lateral direction with a longitudinal wave length between 2.9 and 14.4 m. During the first 700 minutes the growth of the alternate bar in section 1 has a quite constant growth of 0.44 mm/h. After about 700 minutes in section 2 and in section 3 alternate bars start to grow. It is clearly shown that the alternate-bar-pattern propagation initially is from section 1 to section 6, thus in the upstream direction. When the alternate bars have grown to about 0.004 m, the development propagation becomes less clear. The wiggles in the figure can be explained by the fact that the bars are migrating, whereas the section boundaries are fixed, see Appendix E.

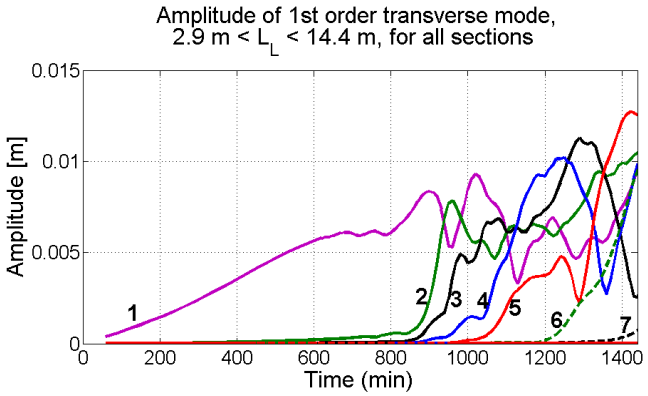

Figure 6-9: Development of amplitude of transverse mode 1, 2.9 m <L_L < 14.4 m (R3a)

Disturbance-driven development

In Figure 6-10 (left), one can see the amplitude development of the first mode in different sections. Like in the case of no disturbance, the first alternate-bar growth starts at section 1. This can be explained by the fact that the disturbance bars reach the bend after about 250 minutes, so initially one sees the bend-driven development. Due to the disturbance, alternate bars also begin to develop in the other section. The development starts in section 4 and propagates to section 3 and 2, and then a new development starts in section 7, which propagates to section 6 and 5. The disturbance triggers alternate-bar formation in section 4 after about 280 minutes. This alternate-bar pattern subsequently propagates towards section 3 and 2, thus in the downstream direction. Later also in section 7 alternate-bar development is triggered by the disturbance. Also this pattern propagates in the downstream direction.

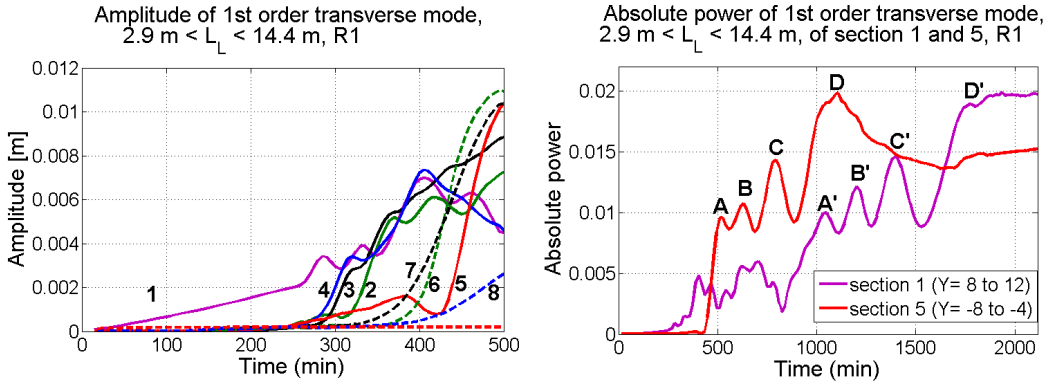

Figure 6-10: Development of amplitude of first-mode transverse harmonic initially (left), and in a later stage (right) for R1

The downstream pattern propagation is not only observed in the initial stage, but also in a later stage, see Figure 6-10 (right). The figure shows the development of the alternate-bar amplitude of section 1 (purple) and section 5 (red). The developments between points 'A' and 'D' are unique for section 1 and section 5, apart from the time lag. The time lag suggests that the pattern propagates with a constant celerity of about 1.6 m/h from section 5 to section 1, thus in the downstream

direction. Remarkable is that the propagation speed of the pattern is almost equal to the migration rate of an individual bar.

6.3.2.3 Conclusions

The following conclusions can be drawn according to the direction of migration of *individual bars*:

- In agreement to linear theory, small-amplitude long bars have been observed to migrate in the upstream direction.
- Contrary to linear theory, bars with higher amplitude, independent of their longitudinal wave length, are migrating in the downstream direction, This can be explained by non-linear effects.

The following conclusions can be drawn according to the direction of migration of *bar patterns*:

- Bar pattern development caused by boundary disturbance is dominant over bar-pattern development caused by the bend.
- Boundary-disturbance-driven bar-pattern development is in the downstream direction.
- Bend-driven bar-pattern development is in the upstream direction, in case of super-resonant conditions.

6.3.3 Bed instability

The goals and hypothesis for this specific section can be found in section 6.2.3. Also the way the results in this chapter were gathered and the characteristics of the simulations, can be found in that section.

6.3.3.1 Linear theory

In the left part of Figure 6-11, one can observe the amplification rate of the most-unstable mode versus the half-width-to-depth ratio. Linear theory predicts that for $\beta < 18.1$, the first mode is the most-unstable mode. For $\beta > 18.1$ and $\beta < 23.7$, the second mode is the most-unstable mode. For higher beta values, the third mode is the most unstable. The simulations in this section have a beta value of 24.3, so one would expect the third mode to appear first. In the right part of Figure 6-11, one sees the observed amplification rate for $\beta = 24.3$, as investigated in section 5.3.1. The figure shows that for the 'upwind' method, the second mode is the most unstable, whereas the first and third mode are slightly less unstable, which does not comply very well with linear theory. Section 5.3.1 already explained that the 'central' method represents the left picture more properly. The simulations in this section, however, are carried out with the 'upwind' scheme. For analysing whether the most-unstable bar, according to the behaviour of small-amplitude bars, becomes apparent first, it is not of importance whether the right part of Figure 6-11 agrees with linear theory.

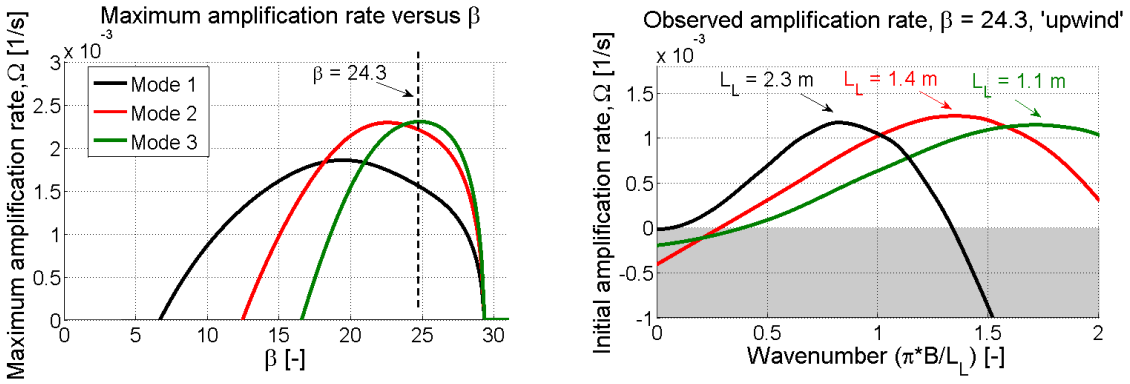

Figure 6-11: Left: maximum amplification rate of different modes, versus β. Right: Observed amplification rate for β=24.3, 'upwind' method, see section 5.3.1..

6.3.3.2 Instability due to bed perturbations

Simulation R4 is carried out to observe the initial development of bars with an initially perturbed bed. The random amplitude of the perturbation is between +/- 1% of the total water depth. The initial development of bars can be seen in Figure 6-12 (left). The bed is analysed with Fourier transforms (right figure). Although one would expect the second-mode bar to be the most unstable immediately from the start of the simulation, the third mode (with an L_L of 0.95 – 1.1 m) appears initially to be the most unstable. After 90 minutes, the second mode (with L_L = 1.4 m) becomes the most unstable. The longitudinal wave lengths, of the most-unstable third and second-mode bars in Figure 6-12, do comply with Figure 6-11 (right).

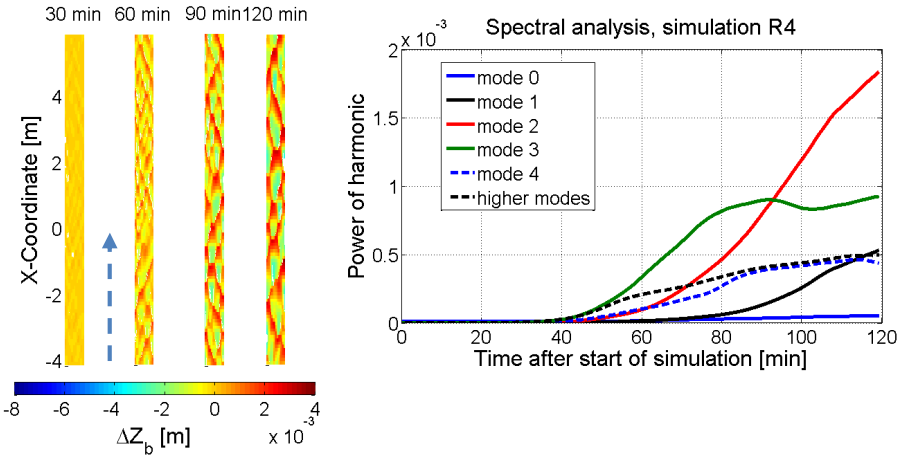

Figure 6-12: Initial bar development on a randomly perturbed bed. Bed level change plots (left). Fourier analysis (right).

6.3.3.3 Instability due to fluctuating discharge

Also the appearing of bars is tested for an inflowing discharge disturbance, which is uniform in space, but varying in time. Due to this perturbation, a second-mode bar was immediately created at the upstream boundary, see Figure 6-13. The longitudinal wave length of the second-mode bars was 1.4 m. It is remarkable that this matches the observed behaviour of small-amplitude bars, but not with the initial stage of simulation R4, see section 6.3.3.2.

A possible explanation for the difference between simulations R4 an R1 is that the asymmetrical third-mode bar in the simulation with boundary disturbance (R1) might be suppressed by the fact that the discharge perturbation is symmetric.

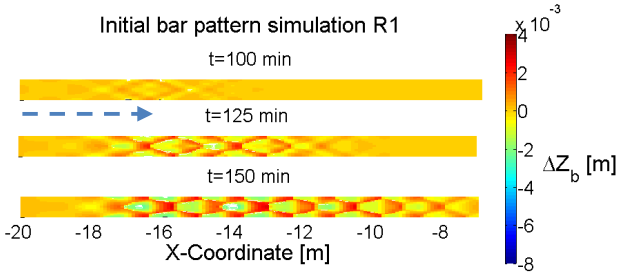

Figure 6-13: Initial second-mode bars at the upstream boundary

6.3.3.4 Conclusions

The following conclusions can be drawn according to the instability of the bed:

- In agreement with linear theory, the most-unstable bar mode (the bar mode with the largest growth rate) becomes apparent if the bed is unstable. However, it has been shown that a higher-mode pattern may initially arise.
- A symmetrical perturbation can suppress the growth of asymmetric bar modes.
- Above a certain critical width-to-depth ratio second-mode bars are the most-unstable modes, whereas below this parameter first-mode bars are the most unstable.

7 Conclusions and recommendations

7.1 Conclusions

In chapter 1, three objectives are formulated for this study. In this section, I will conclude my findings per objective.

Improving and validating the numerical model of van der Meer et al. (2011), chapter 4.

1.1 The numerical model is capable of simulating alternate-bar development under both super- and sub-resonant regimes. Under super-resonant regimes both downstream and upstream of the bend non-migrating alternate bars occur. Under sub-resonant conditions only downstream of the bend non-migrating alternate bars appear. These observations are qualitatively in agreement with observations by Zolezzi et al. (2005).

1.2 The wave length of forced bars is well predicted if the 'central' method is used.

1.3 The behaviour of small-amplitude alternate bars (bar amplitudes smaller than 2%) complies with linear theory for the 'central' method. For the second-mode bars a discrepancy is found between the numerical model and the analytical theory. This study does not have an answer on the reason for the mismatch.

1.4 The numerical model is not capable of reproducing the super-resonant experiments of Zolezzi (2005). The numerical model appears to overpredict the point of resonance and therefore has problems with reproducing super-resonant regimes near the point of resonance. This was also observed by Van der Meer et al. (2011).

Studying the effects of some typical numerical factors (typical schemes for the morphological updating procedure, horizontal eddy viscosity and grid resolution) on alternate-bar characteristics, chapter 5.

Influence of numerical diffusion (introduced via the morphological updating procedure):

2.1 Numerical diffusion, caused by the 'upwind' procedure, is introduced by the shift of the bed-load transport curve in the downstream direction. This shift is equal to half of the longitudinal grid size. The effect of numerical diffusion can therefore be decreased by increasing the grid resolution.

2.2 Numerical diffusion causes the shorter small-amplitude bars to be damped, so the 'upwind' free-bar diagram is shifted towards longer bars. This causes the wave length of free bars to be longer for the 'upwind' method than for the 'central' method.

2.3 Numerical diffusion influences the bed topography spectrum. The higher harmonics within the bar pattern are damped by the numerical diffusion, so the relative contribution of the first-mode harmonic is enlarged. The consequence is that for the 'upwind' method the deposition of sediment is more concentrated near the banks (and not so much on the channel axis, as is the case with the 'central' method), which results in higher bar peaks.

2.4 At shallow flows (large width-to-depth ratios) an 'upwind' bar peak can become inactive, whereas it is still active during a 'central' simulation, see conclusion 2.3. This causes

'upwind' alternate bars (in forced conditions) to be much shorter for large width-to-depth ratios. This explains why Van der Meer et al. (2011) observed the alternate bars for $\beta>13$ to be much shorter than predicted by linear theory, for they used the 'upwind' method.

2.5 The effect of numerical diffusion on the point of resonance is insignificant, because the point of resonance is related to long bars, which are hardly influenced by the 'upwind' shift of the bed-load transport curve, see conclusion 2.2.

Horizontal eddy viscosity

2.6 The amplification rate of small-amplitude bars is inversely proportional with the horizontal eddy viscosity. But because it influences the amplification rate of all small-amplitude bars, the effect is mainly on the time scale of bar formation, and does not have a significant effect on the wave length of bars.

2.7 The point of resonance is observed to be dependent on the horizontal eddy viscosity, a larger ν_H results in a lower β_{res}.

Lateral grid resolution

2.8 The mismatch between the observed behaviour of higher-mode bars and the prediction of linear theory cannot be explained by a lack of lateral grid resolution.

Acquiring a better understanding of the development process of alternate bars, upstream of a bend under super-resonant conditions, chapter 6.

3.1 Disturbance-driven (by applying a disturbed discharge at the inflow boundary) alternate-bar formation is dominant over bend-driven alternate-bar formation, because bend-driven alternate-bar formation takes place on a much longer timescale.

Influence of the bend

3.2 If no disturbance is used, the bend will influence the bed upstream of the bend. The resulting equilibrium alternate-bar pattern does not significantly differ from the equilibrium alternate-bar pattern, generated by a boundary disturbance. So for the equilibrium bed topography the applying of an inflow disturbance is not of importance.

Individual bar migration

3.3 In agreement to linear theory, small-amplitude long bars have been observed to migrate in the upstream direction only under super-resonant conditions.

3.4 Contrary to linear theory, bars with higher amplitude, irrespective of their longitudinal wave length, are observed to migrate in the downstream direction. This can be explained by non-linear effects.

Bar pattern propagation

3.5 Disturbance-driven bar-pattern development is in the downstream direction.

3.6 Bend-driven bar-pattern development is in the upstream direction.

Bed instability

3.7 In agreement with linear theory, the most-unstable bar mode (the bar mode with the largest growth rate) becomes immediately apparent if the bed is unstable.

3.8 A symmetrical perturbation can suppress the growth of asymmetric bar modes.

7.2 Relevance

This study contributes to both literature and modelling practice. First of all, this study shows the influence of non-linear effects. For alternate bars with an amplitude smaller than 2% of the water depth the growth process was observed to be linear, for larger bars the amplification rate and migration rate were observed to be dependent on the bar amplitude. Long bars, for example, with a developed height migrate in the downstream direction, whereas in the literature it is proposed that they should migrate in the upstream direction.
Furthermore, this study provides an idea on how the bend influences the bed upstream of it under super-resonant conditions. It seems that immediately upstream of the bend a scour hole develops at the inner bend, whereas accretion occurs at the outer bend. This scour-accretion pattern propagates in the upstream direction. This observation seems to confirm the hypothesis of Zolezzi and Seminara (2001a), in which they stated that upstream influence can be explained by the fact that sufficiently-long small-amplitude bars migrate in the upstream direction, only under super-resonant conditions.

This research is relevant for modellers, first, for it shows that Delft3D is able to represent the location and length of the alternate bars if the 'central' scheme is used for the morphological updating procedure. The 'upwind' procedure can affect the wave length of alternate bars. In deep or narrow rivers the wave length of bars is overpredicted, because shorter bars are damped by the 'upwind' scheme. In shallow or wide rivers the wave length of bars is under-predicted, because 'upwind' bars have higher peaks and can become inactive due to drying (the higher transverse modes within the bar spectrum are damped). One should therefore use the 'central' scheme if possible. The disadvantage is that this scheme can lead to bed instability, so one might be obliged to use the 'upwind' scheme. If that is the case, one should increase the grid resolution, to decrease the diffusive effect of the 'upwind' scheme and take the consequences of the 'upwind' scheme in mind.
Secondly, this study provides evidence that Delft3D is able to simulate small-scale (laboratory scale) models, even up to a water depth of about 1 cm. To stabilize these simulations, the horizontal eddy viscosity had to be increased. So far, few simulations were carried out with Delft3D on such a small scale.
Thirdly, the study shows that it is hard to simulate the occurrence of alternate bars if the conditions in the river are near resonance. This was caused by the horizontal eddy viscosity, which was too high, for stability reasons. Probably this problem will not occur for large-scale simulations, because in those simulations the horizontal eddy viscosity does not need to be enlarged for stability reasons.

7.3 Recommendations

I would recommend to continue the research with some different, and possibly more accurate, settings, but they will probably only change the results of this study quantitatively, and not so much

qualitatively. Because the conclusions in section 7.1 are rather qualitative, I propose them to be useful and accurate for further studying the behaviour of alternate bars.

Transverse slope effects
Numerous studies have been carried out to analyse the influence of transverse bed slope effects on sediment transport, but still it is a field with a large uncertainty. As described in chapter 4, the strength of gravitational pull on transverse slopes has large consequences for the bar amplitude. Although this study did not focus on the bend, I observed that the morphology in the bend did not match the experiments of Zolezzi et al. (2005). This mismatch is probably caused by errors in the prediction of transverse slope effects. For these reasons it is recommendable to improve the prediction of the transverse bed slope effect. This could be established by applying the particle-oriented approach of Nabi (2012). The present model in this research, models sediment transport on an empirical way, whereas Nabi simulated the movement of particles on a physics-based way.

Non-linear effects
In this study, non-linear effects have shown to be important for the rate and direction of bar migration, the selected wave length of free bars, etc. To get a better idea of non-linear effects, it seems recommendable to investigate the contribution of the non-linear terms in the equations for flow and sediment transport in Delft3D. Another way of investigating the non-linear effects is by modelling the linear equations numerically, and subsequently comparing the output of the linear numerical model with the non-linear Delft3D model.

Experimental focus on upstream influence
The experiments by Zolezzi et al. (2005) are one of the few available super-resonant experiments. Unfortunately, I was not able to reproduce the experiments, as explained in section 4.2.2.1. It might therefore be recommendable to carry out some super-resonant experiments that have a Froude number well below one. It might also be interesting to monitor during these experiments how the bend has an influence on the upstream straight reach. This study has shown that the influence of the bend can be observed more clearly if no disturbance is added at the inflow boundary.

Upscaling the model
In section 7.2, I already stated that the problem with the overdimensioned horizontal eddy viscosity might be absent for large-scale problems. It might therefore be recommendable to upscale the present model, to see whether the upscaled model is able to reproduce the experiments of Zolezzi et al. (2005) more properly.

Analysis of characteristics
In Mosselman et al. (2006) a simplified analysis of characteristics was carried out to show that under super-resonant conditions the bend has an influence in the downstream direction. It might be recommendable to extend the more complete analysis of characteristics by De Vriend (1987) for super-resonant conditions. This extended analysis of characteristics might explain more thoroughly why the direction of influence is both downstream and upstream under super-resonant conditions.

References

BLONDEAUX, P. & SEMINARA, G. 1985. A unified bar–bend theory of river meanders. *Journal of Fluid Mechanics,* 157**,** 449-470.

COLOMBINI, M., SEMINARA, G. & TUBINO, M. 1987. Finite-amplitude alternate bars. *Journal of Fluid Mechanics,* 181**,** 213-232.

COLOMBINI, M. & TUBINO, M. 1990. Finite amplitude free-bars: a fully nonlinear spectral solution *Sand Transport in Rivers, Estuaries and the Sea* Proc. Euromech 262 Colloquium, Wallingford, UK, 26-29 June**,** 163-169.

CROSATO, A., GETANEH, A. A., DESTA, F. B., UIJTTEWAAL, W. S. J. & LE, U. 2010. Long-duration laboratory experiment of slow development of steady alternate bars. *In A Dittrich, K Kroll, J Aberle & P Geisenhainer (Eds.), Proceedings of the International Conference on Fluvial Hydraulics (2)***,** 1035-1040.

CROSATO, A., MOSSELMAN, E., BEIDMARIAM DESTA, F. & UIJTTEWAAL, W. S. J. 2011. Experimental and numerical evidence for intrinsic nonmigrating bars in alluvial channels. *Water Resources Research,* 47.

DE VRIEND, H. J. 1987. Analysis of horizontally two-dimensional morphological evolutions in shallow water. *J. Geophys. Res. (Oceans), AGU,* 92**,** 3877-3893.

DELTARES 2011. Delft3D-FLOW: Simulation of multi-dimensional hydrodynamic flows and transport phenomena, including sediments, User Manual. Version 3.15, revision 17474.

EINSTEIN, H. A. 1950. The bedload function for sediment transport in open channel flow *US Dept. Agric. Tech. Bull. ,* 1026.

ENGELUND, F. & HANSEN, E. 1967. A Monograph on Sediment Transport in Alluvial Streams. *Danish Technical Press*.

FUJITA, Y. & MURAMOTO, Y. 1985. Studies on the process of develoment of alternate bars. *Bulleting of the Disaster Prevention Research Institute (1985),* 35(3)**,** 55-86.

IKEDA, S. 1982. Prediction of alternate bar wavelength and height. *Rep. Dept. Found. Engng & Const. Engng, Saitama Univ. ,* 12**,** 23-45.

KOCH, F. G. & FLOKSTRA, C. 1980. Bed level computations for curved alluvial channels. *Proceedings of the XIXth congress of the International Association for Hydraulic Research, 2-7 Feb. 1981, New Delhi, India,* 2**,** 357-364.

LANZONI, S. 2000. Experiments on bar formation in a straight flume: 1. Uniform sediment. *Water Resources Research* 46**,** 3337-3349.

LESSER, G. R., ROELVINK, J. A., J.A.T.M., K. & STELLING, G. S. 2004. Development and validation of a three-dimensional morphological model. *Coastal Engineering* 51**,** 883-915.

MEYER-PETER, E. & MÜLLER, R. 1948. Formulas for bed-load transport. *Proc. of the 2nd meeting of the International Association for Hydraulic Structures Research***,** 39-64.

MOSSELMAN, E., TUBINO, M. & ZOLEZZI, G. 2006. The overdeepening theory in river morphodynamics: Two decades of shifting interpretations. *Proc. River Flow 2006,* Lisbon 6-8 Sept., 2006.

NABI, M. 2012. Simulation of subaqueous Dunes using Detailed Hydrodynamic. *PhD thesis, Delft University of Technology, Delft, The Netherlands*.

OLESEN, K. W. 1983. Alternate bars in and meander of alluvial rivers. *Presented on a Specialty Conference on River Meandering, Rivers '83, ASCE, New Orleans*.

PARKER, G. 1990. Surface-based bedload transport relation for gravel rivers. *J. Hydraul. Res.,* 20**,** 417-436.

PARKER, G. & ANDERSON, A. G. 1975. Modelling of meandering and braiding in rivers. *Proc. of ASCE Modelling Symposium 1975,* San Fransisco, Calif. 1975**,** 575-591.

RHOADS, B. L. & WELFORD, M. R. 1991. Initiation of river meandering. *Progress in Physical Geogrpahy,* 15**,** 127-156.

SEMINARA, G. & TUBINO, M. 1989. Alternate bars and meandering: Free, forced and mixed interactions. *River meandering, Water Resourc. Monogr. Ser. ,* 12**,** 267-320.

SEMINARA, G. & TUBINO, M. 1992. Weakly nonlinear theory of regular meanders. *Journal of Fluid Mechanics,* 244**,** 257-288.

STRUIKSMA, N. 1983. Point bar initation in bends of alluvial rivers with dominant bed load transport. *TOW Report R657-XVII/W308-part III,* Delft Hydraulics Laboratory, The Netherlands.

STRUIKSMA, N., OLESEN, K. W., FLOKSTRA, C. & DE VRIEND, H. J. 1985. Bed deformation in curved alluvial channels. *Journal of Hydraulic Research,* 23**,** 57-79.

TALMON, A. M., STRUIKSMA, N. & VAN MIERLO, M. C. L. M. 1995. Laboratory measurements of the direction of sediment transport on transverse alluvial-bed slopes. *Journal of Hydraulic Research,* 33**,** 495-517.

VAN DER MEER, C., MOSSELMAN, E., SLOFF, K., JAGER, B., ZOLEZZI, G. & TUBINO, M. 2011. Numerical simulations of upstream and downstream overdeepening. *RCEM2011,* Tsinghua University Press, Beijing, China.

VANZO, D., SIVIGLIA, A., ZOLEZZI, G., STECCA, G. & TUBINO, M. 2011. Interaction between steady and migrating bars in straight channels. *RCEM2011,* Tsinghua University Press, Beijing, China.

ZOLEZZI, G., GUALA, M., TERMINI, D. & SEMINARA, G. 2005. Experimental observations of upstream overdeepening. *Journal of Fluid Mechanics,* 531**,** 191-219.

ZOLEZZI, G. & SEMINARA, G. 2001a. Downstream and upstream influence in river meandering. Part 1. General theory and application to overdeepening. *Journal of Fluid Mechanics,* 438**,** 183-211.

ZOLEZZI, G. & SEMINARA, G. 2001b. Downstream and upstream influence in river meandering. Part 2. Planimetric development. *Journal of Fluid Mechanics,* 438**,** 183-211.

Appendices

Appendix A Background theory

This Appendix gives a brief overview of some empirical and analytical model to predict (alternate) bar properties.

A.1. Empirical models

Ikeda (1982) made an extensive analysis on alternate-bar length and height data. The data analysis in his research was based on both experimental and field data. The data covered a wide range of the following variables:

- $0.13 < F < 1.98$ Froude number
- $1510 < Re < 3.13*10^6$ Reynolds number
- $3.5 < B/D < 60$
- $3.76 < B/D_{50} < 422$

Wavelength

Ikeda found that the wavelength is not dependent on F for F<0.8. In these conditions, the formula of Parker and Anderson (1975) appeared to be quite accurate:

$$L_L = 5\sqrt{\frac{BD}{c_f}} = 5\sqrt{\frac{BDC^2}{g}} \qquad \text{for F<0.8} \qquad \text{(A-1)}$$

For Froude numbers higher than 0.8, the wavelength is observed to be dependent on B/D and d_s. The formula for the wave length in these conditions was based on a dimensionless analysis:

$$\frac{L_L}{B} = 181 c_f \left(\frac{B}{D}\right)^{0.55} = 181 \frac{g}{C^2}\left(\frac{B}{D}\right)^{0.55} \qquad \text{for F< 0.8 and } 4 < \frac{B}{D} < 70 \qquad \text{(A-2)}$$

Bar height

The bar height, H_B, was found to be dependent on the width-to-depth ratio. H_B is defined as the distance between the lowest and highest point of the bed in the cross-section at the lowest depression of a bar unit.

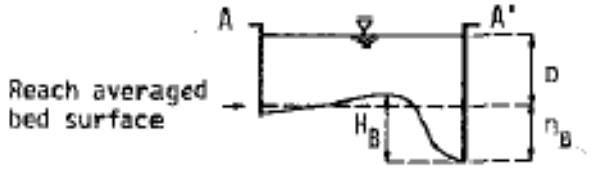

Figure A-1: Definition of H_B (Ikeda, 1982)

The empirical formula yields:

$$\frac{H_B}{D} = 1.61 c_f \left(\frac{B}{D}\right)^{1.45} = 1.61 \frac{g}{C^2}\left(\frac{B}{D}\right)^{1.45} \qquad \text{for F>0.74 and } 4 < \frac{B}{D} < 40 \qquad \text{(A-3)}$$

The possible prediction error for all formulas was estimated by Ikeda in the range of +80% up to -40%. So the formulas have the tendency to overpredict the wave length and bar height.

A.2. Analytical models

A.2.1. Linear models

In the 1960s, it was proposed that alternate bars can be explained by a stability analysis of the mathematical equations for flow and sediment transport. In 1985, two important linear theories were published, which are the base for the present theories. One of these theories, (Blondeaux and Seminara, 1985), assumes that migrating bars in a straight channel, without geometrical perturbations, become non-migrating under resonant conditions. The other classical linear theory was presented by Struiksma et al. (1985). In this theory, it is assumed that alternate bars are generated by a geometrical perturbation, for instance a groyne, change in channel curvature, etc.

In this section, the basics of both linear theories and subsequent researches will briefly be described.

Struiksma et al. (1985)

The basis of the theory developed by Struiksma et al. (1985) are the equations for flow (momentum and continuity) and sediment transport. Subsequently, the simplified equations were linearized by imposing small perturbations, like: $z_b = z_{b,0} + z_b'$, $u = u_0 + u'$, etc. The values for h_0, u_0, v_0, etc. are the zero-order (mean) values for the water depth, streamwise velocity and cross-stream velocity respectively. These can be calculated with Chézy's law.

The solution of the system of linear equations can be derived by considering a harmonic perturbation:

$$z_b^{'} = \hat{z}_b \exp i(kx + k_w y) \qquad \text{(A-4)}$$

In which k is a complex wavenumber in the longitudinal direction and k_w is the real wavenumber in the lateral direction. The real part of k represents the real wave length, whereas the imaginary part represents the damping length.

Subsequently, Struiksma et al. presented a fourth order polynomial for non-migrating, non-amplifying alternate bars:

(A-5)

0

$$(k\lambda_w)^4 y^2 b + (k\lambda_w)^3 y^2 i\left[\left(A\cdot f - 1\right)\frac{\lambda_w}{\lambda_s} - \frac{b}{2}\right] + (k\lambda_w)^2\left[1 + \frac{1}{2}y^2(3A\cdot f - 1)\frac{\lambda_w}{\lambda_s}\right] +$$

In which:

$$(k\lambda_w) i\left[\frac{b-3}{2} - \frac{C^2}{2g}h_0\frac{\lambda_w}{\lambda_s}\right] - \frac{\lambda_w}{\lambda_s} = 0 \quad \text{with} \quad \lambda_w = 2\pi\frac{1}{\pi^2}\left(\frac{B}{h_0}\right)^2 fh_0, \text{ and } \gamma = \frac{1}{\pi}\frac{B}{\lambda_w} \qquad \text{(A-6)}$$

The parameter A denotes a coefficient to take the spiral flow into account, f is the shape factor of grains, b is the degree of non-linearity of the transport formula, the parameter λ_w represents a characteristic length scale for flow adaptations, and λ_s can be seen as a characteristic length scale for bed adaptations. This is clearly explained by Mosselman et al. (2006). A given perturbation is reduced with a factor e (which is about 2.72) after a length of λ_w. Equation (A-5) shows that the longitudinal wave length depends mainly on these two characteristic length scales. The ratio of λ_s to λ_w is called the 'interaction parameter' (Struiksma, 1983).

In the paper of Struiksma et al. (1985), the fourth order polynomial is compared to a more simplified second order polynomial. This second order model was derived by Struiksma (1983), and included (on top of the fourth order polynomial) the following assumptions:

- Secondary flow is neglected
- Streamline curvature is neglected

The second order polynomial reads:

$$(k\lambda_w)^2 + (k\lambda_w) i\left[\frac{b-3}{2} - \frac{\lambda_w}{\lambda_s}\right] - \frac{\lambda_w}{\lambda_s} = 0 \qquad \text{(A-7)}$$

Comparison of models

The two models are compared for the specific conditions in the simulations for this research, see Figure A-2. The real wavenumber is defined as:

$$k_r = \frac{2\pi}{L_p} \qquad \text{(A-8)}$$

In which L_p is defined as the real wave length of the alternate bar. One can see that the prediction of the real wavenumber is quite correlated between the two polynomials for λ_s/λ_w between 0.5-2.2. For higher and lower value than the given interval there is no correlation between the two models. The second order model does not predict a real wavenumber for $\lambda_s/\lambda_w < 0.24$ and $\lambda_s/\lambda_w > 2.52$. The figure shows that the wave length becomes shorter for larger values of the interaction parameter. Because the interaction parameter is proportional to β^2 (Mosselman et al., 2006), the bars are predicted to be shorter for more shallow or wide rivers.

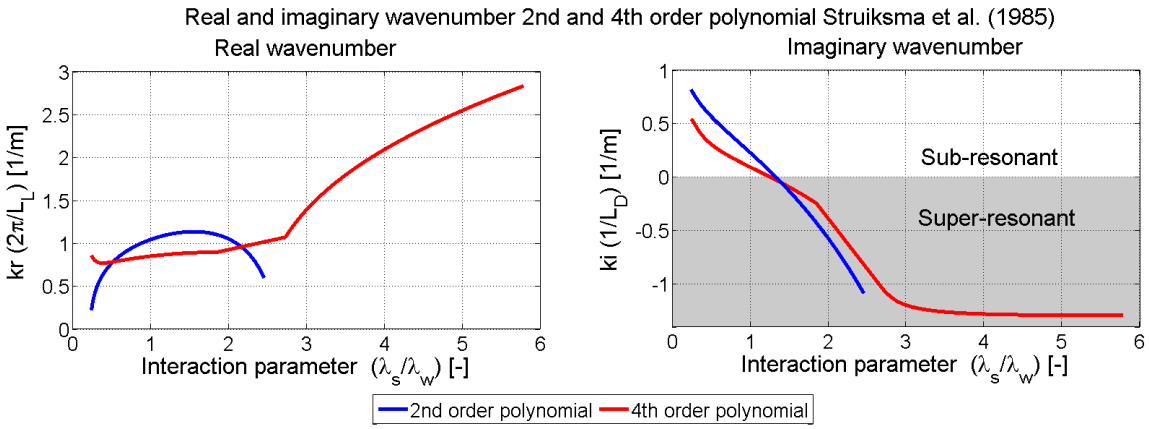

Figure A-2: The real wave and imaginary wavenumber of alternate bars (Struiksma et al., 1985)

The imaginary wavenumber is a measure for the damping length and is defined as:

$$k_i = \frac{1}{L_D} \qquad \text{(A-9)}$$

In which L_D denotes the damping length. In Figure A-2, one can see the prediction of the second and fourth order polynomial of Struiksma et al. In the figure one can see that the imaginary wavenumber is decreasing, or even getting negative for increasing interaction parameter values. Positive damping can be seen as a spatial decrease of bar amplitude. No damping means no spatial decrease nor increase of the bar amplitude. This condition is called 'resonant' by Blondeaux and Seminara (1985). Negative damping can be seen as a spatial increase of bar amplitude. The two graphs are correlated much better for the imaginary wavenumber than for the real wavenumber. Also the prediction of the point of resonance (k_I = 0, L_D =0) is matching. The point of resonance corresponds with λ_s/λ_w = 1.25 according to the fourth order model and 1.33 according to the second order model.

The second order polynomial was used by Van der Meer et al. (2011) to analyse the results from the numerical model. These figures show that the prediction of the point of resonance was not really influenced by the choice for the second order polynomial. The wave length prediction of alternate bars, however, was only reliable for interaction parameter values between 0.5 and 2.2. For lower and higher interaction parameters, the fourth order polynomial should have been used.

Blondeaux and Seminara (1985)

This linear theory is discussed in section 2.3.1 and is used as the base of the analytical model for this research.

A.2.2. (Weakly) non-linear models

No estimation of the final amplitude can be made with linear theories, because these theories assume a linear growth and migration rate. The amplification rate is therefore exponential and the resulting bar height infinite. Non-linear effects cause the amplification rate to be decreased to zero, when the bar has developed itself. Colombini et al. (1987) made a weakly non-linear theory in which they tried to find solutions for alternate-bar patterns near the critical width-to-depth ratio, below which no alternate bars should be formed. The assumed conditions by Colombini et al are:

$$\beta = \beta_c(1+\varepsilon), \quad \lambda = \lambda_c + \lambda_1\varepsilon \qquad \text{(A-10)}$$

In which β_c denotes the critical with to depth ratio (usually not equal to β_{res}), ε is the 'perturbation', which is assumed to be much smaller than 1, λ is the wavenumber of the alternate-bar pattern (π*B/L), λ_c is the wavenumber corresponding with β_c and λ_1 is the perturbation of the wavenumber. It was shown in their paper that also for ε = O(1), the weakly non-linear theory gave quite convergent results.

Colombini et al. (1987) proposed a formula to calculate the alternate-bar height, defined as the difference between the maximum and minimum bed elevation within one bar unit. The calculated alternate-bar height is scaled with the initial water depth. The formula reads:

$$H_{BM\_Colombini} = b_1\sqrt{\frac{\beta-\beta_c}{\beta_c}} + b_2\frac{\beta-\beta_c}{\beta_c} + O\left(\varepsilon^{\frac{3}{2}}\left|h_{eq}\right|^3\right) \qquad \text{(A-11)}$$

The values of b_1 and b_2 are presented in the paper of Colombini et al. (1987), h_{eq} is the equilibrium bar amplitude.

This definition of the bar height differs from the one Ikeda (1982) used, see section A.1. According to Ikeda the following relation can be assumed: $H_{MB} = 1.5H_B$

Appendix B Analytical model

The analytical model of this research is based on the model of Colombini et al. (1987), see section 2.3.2. The model, as proposed in their papers, had to be adjusted to be able to compare its predictions with the observations in the numerical model. The expressions that had to be adjusted are found in this appendix (see section B.1).

In the second part of this appendix (section B.2), the difference in prediction of the analytical model is discussed between a constant Chézy approach and a White-Colebrook approach.

B.1. Derivation

B.1.1. Roughness

In the paper, the roughness prediction is based on the formula of Einstein (1950). In the numerical model, the White-Colebrook relation is used to predict the roughness:

$$C = 18\log\left(\frac{12D}{k_s}\right) = 18\log\left(\frac{12\tilde{D}}{\tilde{k}_s}\right) \qquad \text{(B-1)}$$

$$\tilde{D} = \frac{D}{D_0},\ \tilde{k}_s = \frac{k_s}{D_0} \qquad \text{(B-2)}$$

Important parameters in the analytical formula are:

$$C_D = \frac{1}{c_{f,0}}\frac{\partial c_f}{\partial \tilde{D}},\quad C_T = \frac{\theta_0}{c_{f,0}}\frac{\partial c_f}{\partial \theta} \qquad \text{(B-3)}$$

Dimensionless variables are denoted with a '~'. In these formulas c_f denotes the friction coefficient and θ the Shields parameter. The friction coefficient is defined as:

$$c_f = \frac{g}{C^2} \qquad \text{(B-4)}$$

Now C_D and C_T can be derived:

$$\frac{\partial c_f}{\partial \tilde{D}} = \frac{\partial c_f}{\partial C}\cdot\frac{\partial C}{\partial \tilde{D}} = -2g(C)^{-3}\cdot\frac{18}{\frac{12\tilde{D}}{\tilde{k}_s}\ln(10)}\cdot\frac{12}{\tilde{k}_s} = \frac{-36g}{\tilde{D}\cdot\ln(10)\cdot C^3}$$

$$\rightarrow \frac{\partial c_f}{\partial \tilde{D}} = \frac{-36g}{\ln(10)\cdot C^3}$$

$$C_D = \frac{1}{c_{f,0}}\frac{\partial c_f}{\partial \tilde{D}} = \frac{C^2}{g}\cdot\frac{-36g}{\ln(10)\cdot C^3} = \frac{-36}{\ln(10)\cdot C} \qquad \text{(B-5)}$$

$$\frac{\partial c_f}{\partial \theta} = 0 \rightarrow C_T = 0 \qquad \text{(B-6)}$$

B.1.2. Sediment transport

In the numerical model, the Meyer-Peter Müller formula is used. For the analytical model the dimensionless variant of this formula is needed:

$$\Phi = \frac{s}{D_{50}\sqrt{g\Delta D_{50}}} \rightarrow \tilde{\Phi} = 8\left(\mu\theta - \theta_{cr}\right)^{\frac{3}{2}} \qquad \text{(B-7)}$$

In which Φ denotes the transport parameter, s the sediment transport per m width, μ the ripple factor and θ_{cr} the critical Shields parameter (=0.047). The following parameters are important for the analytical model regarding sediment transport:

$$\Phi_D = \frac{1}{\Phi_0}\frac{\partial \Phi}{\partial \tilde{D}}, \quad \Phi_T = \frac{\theta_0}{\Phi_0}\frac{\partial \Phi}{\partial \theta} \qquad \text{(B-8)}$$

$$\frac{\partial \Phi}{\partial \tilde{D}} = 0 \rightarrow \Phi_D = 0 \qquad \text{(B-9)}$$

$$\Phi_T = \frac{\theta_0}{8\left(\mu\theta - \theta_{cr}\right)^{\frac{3}{2}}} \cdot 8\frac{3}{2}\mu\left(\mu\theta - \theta_{cr}\right)^{\frac{1}{2}} = \frac{3\theta_0\mu}{2\left(\mu\theta - \theta_{cr}\right)} \qquad \text{(B-10)}$$

B.2. Comparison between constant vs depth dependent Chézy value

In the paper of Van der Meer et al. (2011), a constant Chézy roughness value was used. As stated in paragraph 4.2.1.4, it is thought to be more realistic if the roughness is dependent on the water depth. In this research, therefore, the White-Colebrook is used as the relation between roughness height and the Chézy roughness value. In section B.1, the adjustments on the analytical model have been discussed for the implementation of the White-Colebrook relation. The model is also adjusted for the case that constant Chézy values are used, in that case C_D and C_T are 0. In Figure B-1, one can observe the predicted free-bar diagrams for both approaches, according to analytical theory.

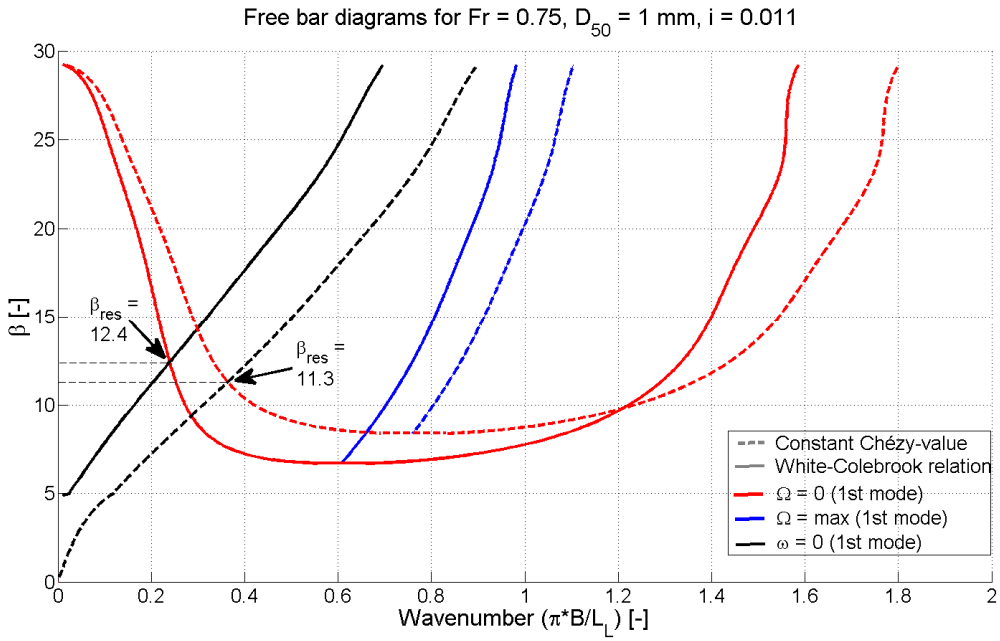

Figure B-1: Influence of roughness definition on analytical model

The diagram shows that:

- β_{res} is larger if a white-Colebrook relation is used, instead of a constant Chézy value.
- The entire diagram is shifted towards shorter bars in the case of a constant Chézy value. This means that non-migrating alternate bars are expected to be shorter in case of a constant Chézy value.

Appendix C Numerical model set-up

This appendix is an addition to chapter 4. The issues regarding wall roughness and viscosity is described in section C.1 and C.2. Section C.3 lists the differences with the numerical model of van der Meer et al. (2011). Section C.4 gives an overview of the characteristics of all the simulations.

C.1. Wall roughness

The walls of the laboratory flume, used by Zolezzi et al. (2005), are made of Plexiglas. In Delft3D, one has the option to adjust the slip condition along closed boundaries and dry grid cells. The three available options are:

- Free slip at the wall: the tangential shear stress is zero
- Partial slip at the wall: the roughness length of the wall has to be specified
- No slip: The tangential (and of course also the normal) velocity is set to zero

The roughness length of Plexiglas is assumed to be in the order of 0.002 mm. The Reynolds stresses near the wall are integrated explicitly, which leads to the following time step restriction:

$$\Delta t \leq \frac{1}{2\upsilon_H\left(\frac{1}{\Delta x^2}+\frac{1}{\Delta y^2}\right)} \qquad \text{(C-1)}$$

If υ_H (horizontal eddy viscosity) is about $3\text{x}10^{-5}$ m^2/s the time step should be smaller than 13 s. So this is not the restrictive time step limitation. However, as explained in paragraph C.2, in the most simulations the horizontal eddy viscosity is 0.01 m^2/s. In that case, the time step should be very small ($\Delta t < 0.04$ s). The applying of wall roughness also leads to more instability in the model.

One of the objectives of this research was to compare the numerical results with laboratory flume experiments. Because the model was based on a laboratory flume, one might expect that wall roughness has a significant effect on the pattern development. The simulations, however, have a large width-to-depth ratio, so the wall effect is thought only to be present locally. Taking into mind the very small time step and the destabilizing effect of a 'partial slip' condition, no wall roughness is taken into account in the simulation for this research.

C.2. Viscosity

The Reynolds stresses in the momentum equations for flow are modelled, using the eddy viscosity concept. The horizontal eddy viscosity is a superposition of three parts (Deltares, 2011):

- Viscosity due to sub grid scale turbulence: ν_{SGS}
- Viscosity due to 3D turbulence: ν_{3D}
- Viscosity due to dispersion for depth averaged simulations: ν_{disp}

In 2D depth averaged simulations, one can choose to calculate the sub grid scale turbulence with a methodology, called Horizontal Large Eddy Simulation (HLES). The contribution of the 3D turbulence has to be added by the user. The contribution due to dispersion has to be added by the user or can be calculated with HLES if the Elders term estimation is enabled.

Hydrodynamic simulation

In this research, the HLES approach is applied together with the Elders term estimation for the dispersion to estimate the horizontal eddy viscosity and horizontal eddy diffusivity. The horizontal eddy viscosity is normally much larger than the vertical eddy viscosity. Because the user defined horizontal eddy viscosity only accounts for the 3D turbulence effect, the specified value should be less than the horizontal eddy viscosity, calculated by the HLES model.

In Table C-1, one can see the values for ν_{SGS} and $\nu_{disp,}$ calculated with HLES, for a simulation without morphology. The user defined background horizontal eddy viscosity is therefore set at $1x10^{-6}$ m^2/s.

Q [l/s]	k_s [m]	Δx [m]	Δy [m]	ν_{SGS} [m^2/s] x10^{-6}	ν_{disp} [m^2/s] x10^{-6}
1.75	0.008	0.20	0.06	1.2	30.8

Table C-1: Viscosity calculated with HLES

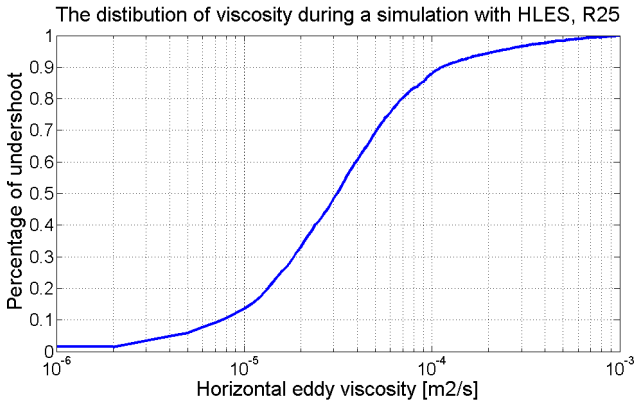

Figure C-1: Cumulative distribution of viscosity during run with HLES, R25

Hydrodynamic simulation (including morphology)

The simulation with HLES is done on a coarse grid, with morphology. During the stage where alternate bars had developed, the distribution of viscosity was as shown in Figure C-1.

The problem is that the simulations turned out to be unstable for this low viscosity-value. Only if the water depth on top of the bars was large enough, the simulation was stable. So for the investigation of small-amplitude bars, the viscosity could be $3*10^{-5}$ m^2/s (median value of Figure C-1). For other simulations the viscosity is set at 0.01, like in the research of Van der Meer et al. (2011).

C.3. Differences with van der Meer et al (2011)

This research is a continuation of the research of Van der Meer et al. (2011). The model in this research is therefore quite similar to the model, used by van der Meer et al. However, some improvements and corrections have been made. They are listed in this paragraph.

Roughness

Van der Meer used a constant Chézy roughness of 22.5. For large-scale rivers, a constant Chézy value is reliable, but for simulation on laboratory scale the roughness should be related to the actual water depth. Therefore a constant Nikuradse roughness height is imposed instead of a constant Chézy value.

Coefficient in transport formula

The simulations of van der Meer were run with a wrong calibration coefficient in the Meyer Peter Muller formula (MPM). The formula in a general form yields:

$$s = \alpha \cdot D_{50} \sqrt{\Delta g D_{50}} \theta^a \left(\mu\theta - \theta_{cr} \right)^b \qquad \text{(C-2)}$$

Were s denotes the sediment transport ($m^3s^{-1}m^{-1}$), Δ the relative density, μ the ripple factor or efficiency factor, θ the Shields parameter, θ_{cr} the critical Shields parameter (0.047), α a calibration coefficient. The parameter a is 0 for MPM and b is 3/2. The calibration coefficient α should be in the order of 8. In the simulations of van der Meer this coefficient was 1. The effect of a higher calibration coefficient is that the bed development will be accelerated with a factor 8. This adjustment does not influence the final bed topography.

Grid

The upstream straight reach of the original model of van der Meer is extended by 24m. The upstream reach in the original model had a length of 12m. This has been done to bring the upstream boundary further away from the bend and to be able to observe the development of bars upstream of the bend.

Viscosity

Van der Meer et al. used a constant horizontal eddy viscosity of 0.01 m^2/s. To investigate the influence of the horizontal eddy viscosity it was varied in this research during the investigation of small-amplitude bar behaviour, see section 5.3.1.

Bed-load submodel scheme

Van der Meer et al. used the 'upwind' scheme to set the bed-load transport at the grid cell faces, see Appendix G. In this research both the 'upwind' and 'central' scheme is used to investigate the influence of this parameter, see chapter 5.

Threshold depth

Van der Meer et al. used a threshold depth of 0.001 m. Below half this threshold depth, the grid cell is set dry. Because the water depth in the model is small, in the order of 0.01 m, the threshold depth in the simulations of this research is set at $1x10^{-5}$ m. The alternate bars are expected to be dried later, than during the simulations of van der Meer et al.

C.4. Simulation characteristics

In Table C-3, one can find the characteristics of the simulations, that were carried out to obtain equilibrium bed topographies (D1_D3D, U3_D3D and R-). In Table C-4, one can find the characteristics of the small-amplitude simulations.

Table C-2:Constant settings for all the simulations in this research

	Variable	Setting
Processes	Secondary flow	on
Physical parameters	Gravity	9.81 m/s^2
	Water density, ρ_w	1000 kg/m^3
	Spiral motion parameter (beta_c)	0.5
	Roughness formula	White-Colebrook
	Calibration coefficient for spiral flow (Espir in Delft3D, E_s)	0.5
	Slip condition	Free
Numerical parameters	Depth specified at:	corners
	Threshold depth	$1x10^{-5}$ m
	Advection scheme for momentum	Cyclic
Morphology	D_{50}	0.001 m
	Transport formula	Meyer-Peter Müller
	μ	0.7
	Formula for bed-slope effect	Koch and Flokstra
	Streamwise bed gradient factor for bed-load transport (α_{bs})	1
	Specific density (ρ_s)	2650 kg/m^3
	Dry bed density	1650 kg/m^3
	ρ_w [kg/m^3]	1000

Table C-3: Characteristics of simulations to obtain equilibrium bed topographies

RunID	Domain	β	k_s [m]	ν_H * [m^2/s]	A_{sh} [-]	α [-]	Δt [s]	Boundary conditions	f_{Morfac}	Morphological updating scheme	DPS **	DPU ***	Initial bed ****	Groyne
D1_D3D	2n	12	0.0162	0.01	4	0.865	0.12	$Q_{P,cell}$-WL	1	'central'	Mean	Mean	Pert.	No
R1	2n	24.3	0.008	0.01	1.9	1	0.6	Q_P-WL	1	'upwind'	Max	Min	Flat	No
R2	3n	24.3	0.008	0.01	1.9	1	0.6	Q_P-WL	1	'upwind'	Max	Min	Flat	No
R3a	2n	24.3	0.008	0.01	1.9	1	0.15	WL-WL	1	'upwind'	Max	Min	Flat	No
R3b	2n	24.3	0.008	0.01	1.9	1	0.15	Q-WL	5	'upwind'	Max	Min	Flat	No
R4	2n	24.3	0.008	0.01	1.9	1	0.6	Q-WL	1	'upwind'	Max	Min	Pert.	No
R5-R9	3n	9.1-21.2	0.009 -0.022	0.01	1.9	1	0.12	Q-WL	1	'central'	Max	Min	Pert.	No
R10-R14	3n	9.1-21.2	0.009 -0.022	0.01	1.9	1	0.12	Q-WL	1	'central'	Max	Min	Pert.	Yes
R15-R19	3n	9.1-21.2	0.009 -0.022	0.01	1.9	1	0.12	Q-WL	1	'upwind'	Max	Min	Pert.	No
R20-R24	3n	9.1-21.2	0.009 -0.022	0.01	1.9	1	0.12	Q-WL	1	'upwind'	Max	Min	Pert.	Yes
R25	2n	24.3	0.008	HLES	1.9	1	0.6	Q-WL	1	'upwind'	Max	Min	Pert.	No
U3_D3D	2n	15	0.0123	0.01	4	1.025	0.12	$Q_{P,cell}$-WL	1	'central'	Mean	Mean	Pert.	No

* HLES means that the viscosity is estimated with a Horizontal Large Eddy Simulation

** DPS is the procedure that sets the depth at the grid cell centre

*** DPU is the procedure that sets the depth at the grid cell face

**** 'Flat' means a uniformly sloping river, with a transversally flat bottom, 'Pert.' means a randomly perturbed bed, with a maximum perturbation amplitude of +/- 0.1 mm

Table C-4: Characteristics of small-amplitude simulations

RunID	Domain	β [-]	k_s [m]	ν_H [m^2/s]	A_{sh} [-]	α [-]	Δt [s]	Morphological updating scheme	DPS **	DPU ***	L_L [m]	h_0 [m]	Mode [-]
S1	3n	24.3	0.008	0.01	1.9	1	0.12	'upwind'	Max	Min	7.5	0.00001	1
S2	3n	24.3	0.008	0.01	1.9	1	0.12	'upwind'	Max	Min	7.5	0.0001	1
S3	3n	24.3	0.008	0.01	1.9	1	0.12	'upwind'	Max	Min	7.5	0.0002	1
S4	3n	24.3	0.008	0.01	1.9	1	0.12	'upwind'	Max	Min	7.5	0.0005	1
S5	3n	24.3	0.008	0.01	1.9	1	0.12	'upwind'	Max	Min	7.5	0.001	1
S6	3n	24.3	0.008	0.01	1.9	1	0.12	'upwind'	Max	Min	7.5	0.002	1
S7	3n	24.3	0.008	0.01	1.9	1	0.12	'central'	Max	Min	30	0.0001	1
S8	3n	24.3	0.008	0.01	1.9	1	0.12	'central'	Max	Min	20	0.0001	1
S9	3n	24.3	0.008	0.01	1.9	1	0.12	'central'	Max	Min	12	0.0001	1
S10	3n	24.3	0.008	0.01	1.9	1	0.12	'central'	Max	Min	7.5	0.0001	1
S11	3n	24.3	0.008	0.01	1.9	1	0.12	'central'	Max	Min	4	0.0001	1
S12	3n	24.3	0.008	0.01	1.9	1	0.12	'central'	Max	Min	2.8	0.0001	1
S13	3n	24.3	0.008	0.01	1.9	1	0.12	'central'	Max	Min	2.3	0.0001	1
S14	3n	24.3	0.008	0.01	1.9	1	0.12	'central'	Max	Min	1.8	0.0001	1
S15	3n	24.3	0.008	0.01	1.9	1	0.12	'central'	Max	Min	1.5	0.0001	1
S16	3n	24.3	0.008	0.01	1.9	1	0.12	'central'	Max	Min	1.3	0.0001	1
S17	3n	24.3	0.008	0.01	1.9	1	0.12	'central'	Max	Min	1	0.0001	1
S18	3n	24.3	0.008	0.01	1.9	1	0.12	'central'	Max	Min	1	0.0001	2
S19	3n	24.3	0.008	0.01	1.9	1	0.12	'central'	Max	Min	1.1	0.0001	2
S20	3n	24.3	0.008	0.01	1.9	1	0.12	'central'	Max	Min	1.2	0.0001	2
S21	3n	24.3	0.008	0.01	1.9	1	0.12	'central'	Max	Min	1.3	0.0001	2
S22	3n	24.3	0.008	0.01	1.9	1	0.12	'central'	Max	Min	1.4	0.0001	2
S23	3n	24.3	0.008	0.01	1.9	1	0.12	'central'	Max	Min	1.5	0.0001	2
S24	3n	24.3	0.008	0.01	1.9	1	0.12	'central'	Max	Min	1.6	0.0001	2
S25	3n	24.3	0.008	0.01	1.9	1	0.12	'central'	Max	Min	1.9	0.0001	2
S26	3n	24.3	0.008	0.01	1.9	1	0.12	'central'	Max	Min	2.3	0.0001	2
S27	3n	24.3	0.008	0.01	1.9	1	0.12	'central'	Max	Min	2.9	0.0001	2
S28	3n	24.3	0.008	0.01	1.9	1	0.12	'central'	Max	Min	3.6	0.0001	2
S29	3n	24.3	0.008	0.01	1.9	1	0.12	'upwind'	Max	Min	30	0.0001	1
S30	3n	24.3	0.008	0.01	1.9	1	0.12	'upwind'	Max	Min	20	0.0001	1
S31	3n	24.3	0.008	0.01	1.9	1	0.12	'upwind'	Max	Min	12	0.0001	1
S32	3n	24.3	0.008	0.01	1.9	1	0.12	'upwind'	Max	Min	7.5	0.0001	1

S33	3n	24.3	0.008	0.01	1.9	1	0.12	'upwind'	Max	Min	4	0.0001	1
S34	3n	24.3	0.008	0.01	1.9	1	0.12	'upwind'	Max	Min	2.8	0.0001	1
S35	3n	24.3	0.008	0.01	1.9	1	0.12	'upwind'	Max	Min	2.3	0.0001	1
S36	3n	24.3	0.008	0.01	1.9	1	0.12	'upwind'	Max	Min	1.8	0.0001	1
S37	3n	24.3	0.008	0.01	1.9	1	0.12	'upwind'	Max	Min	1.5	0.0001	1
S38	3n	24.3	0.008	0.01	1.9	1	0.12	'upwind'	Max	Min	1.3	0.0001	1
S39	3n	24.3	0.008	0.01	1.9	1	0.12	'upwind'	Max	Min	1	0.0001	1
S40	3n	24.3	0.008	0.01	1.9	1	0.12	'upwind'	Max	Min	1	0.0001	2
S41	3n	24.3	0.008	0.01	1.9	1	0.12	'upwind'	Max	Min	1.1	0.0001	2
S42	3n	24.3	0.008	0.01	1.9	1	0.12	'upwind'	Max	Min	1.2	0.0001	2
S43	3n	24.3	0.008	0.01	1.9	1	0.12	'upwind'	Max	Min	1.3	0.0001	2
S44	3n	24.3	0.008	0.01	1.9	1	0.12	'upwind'	Max	Min	1.4	0.0001	2
S45	3n	24.3	0.008	0.01	1.9	1	0.12	'upwind'	Max	Min	1.5	0.0001	2
S46	3n	24.3	0.008	0.01	1.9	1	0.12	'upwind'	Max	Min	1.6	0.0001	2
S47	3n	24.3	0.008	0.01	1.9	1	0.12	'upwind'	Max	Min	1.9	0.0001	2
S48	3n	24.3	0.008	0.01	1.9	1	0.12	'upwind'	Max	Min	2.3	0.0001	2
S49	3n	24.3	0.008	0.01	1.9	1	0.12	'upwind'	Max	Min	2.9	0.0001	2
S50	3n	24.3	0.008	0.01	1.9	1	0.12	'upwind'	Max	Min	3.6	0.0001	2
S51	3n	24.3	0.008	0.01	1.9	1	0.12	'central'	Max	Min	0.7	0.0001	3
S52	3n	24.3	0.008	0.01	1.9	1	0.12	'central'	Max	Min	0.8	0.0001	3
S53	3n	24.3	0.008	0.01	1.9	1	0.12	'central'	Max	Min	0.9	0.0001	3
S54	3n	24.3	0.008	0.01	1.9	1	0.12	'central'	Max	Min	1	0.0001	3
S55	3n	24.3	0.008	0.01	1.9	1	0.12	'central'	Max	Min	1.1	0.0001	3
S56	3n	24.3	0.008	0.01	1.9	1	0.12	'central'	Max	Min	1.2	0.0001	3
S57	3n	24.3	0.008	0.01	1.9	1	0.12	'central'	Max	Min	1.3	0.0001	3
S58	3n	24.3	0.008	0.01	1.9	1	0.12	'central'	Max	Min	1.9	0.0001	3
S59	3n	24.3	0.008	0.01	1.9	1	0.12	'central'	Max	Min	3.8	0.0001	3
S60	3n	24.3	0.008	0.01	1.9	1	0.12	'central'	Max	Min	7.5	0.0001	3
S61	3n	24.3	0.008	0.01	1.9	1	0.12	'upwind'	Max	Min	0.7	0.0001	3
S62	3n	24.3	0.008	0.01	1.9	1	0.12	'upwind'	Max	Min	0.8	0.0001	3
S63	3n	24.3	0.008	0.01	1.9	1	0.12	'upwind'	Max	Min	0.9	0.0001	3
S64	3n	24.3	0.008	0.01	1.9	1	0.12	'upwind'	Max	Min	1	0.0001	3
S65	3n	24.3	0.008	0.01	1.9	1	0.12	'upwind'	Max	Min	1.1	0.0001	3
S66	3n	24.3	0.008	0.01	1.9	1	0.12	'upwind'	Max	Min	1.2	0.0001	3
S67	3n	24.3	0.008	0.01	1.9	1	0.12	'upwind'	Max	Min	1.3	0.0001	3
S68	3n	24.3	0.008	0.01	1.9	1	0.12	'upwind'	Max	Min	1.9	0.0001	3
S69	3n	24.3	0.008	0.01	1.9	1	0.12	'upwind'	Max	Min	3.8	0.0001	3

S70	3n	24.3	0.008	0.01	1.9	1	0.12	'upwind'	Max	Min	7.5	0.0001	3
S71	3n	24.3	0.008	0.001	1.9	1	0.12	'upwind'	Max	Min	7.5	0.0001	1
S72	3n	24.3	0.008	0.001	1.9	1	0.12	'upwind'	Max	Min	4	0.0001	1
S73	3n	24.3	0.008	0.001	1.9	1	0.12	'upwind'	Max	Min	2.8	0.0001	1
S74	3n	24.3	0.008	0.001	1.9	1	0.12	'upwind'	Max	Min	2.3	0.0001	1
S75	3n	24.3	0.008	0.001	1.9	1	0.12	'upwind'	Max	Min	2	0.0001	1
S76	3n	24.3	0.008	0.001	1.9	1	0.12	'upwind'	Max	Min	1.8	0.0001	1
S77	3n	24.3	0.008	0.001	1.9	1	0.12	'upwind'	Max	Min	1.5	0.0001	1
S78	3n	24.3	0.008	0.001	1.9	1	0.12	'upwind'	Max	Min	1.3	0.0001	1
S79	3n	24.3	0.008	0.001	1.9	1	0.12	'upwind'	Max	Min	1	0.0001	1
S80	3n	24.3	0.008	$3x10^{-5}$	1.9	1	0.12	'upwind'	Max	Min	30	0.0001	1
S81	3n	24.3	0.008	$3x10^{-5}$	1.9	1	0.12	'upwind'	Max	Min	20	0.0001	1
S82	3n	24.3	0.008	$3x10^{-5}$	1.9	1	0.12	'upwind'	Max	Min	12	0.0001	1
S83	3n	24.3	0.008	$3x10^{-5}$	1.9	1	0.12	'upwind'	Max	Min	7.5	0.0001	1
S84	3n	24.3	0.008	$3x10^{-5}$	1.9	1	0.12	'upwind'	Max	Min	4	0.0001	1
S85	3n	24.3	0.008	$3x10^{-5}$	1.9	1	0.12	'upwind'	Max	Min	2.8	0.0001	1
S86	3n	24.3	0.008	$3x10^{-5}$	1.9	1	0.12	'upwind'	Max	Min	2.3	0.0001	1
S87	3n	24.3	0.008	$3x10^{-5}$	1.9	1	0.12	'upwind'	Max	Min	1.8	0.0001	1
S88	3n	24.3	0.008	$3x10^{-5}$	1.9	1	0.12	'upwind'	Max	Min	1.5	0.0001	1
S89	3n	24.3	0.008	$3x10^{-5}$	1.9	1	0.12	'upwind'	Max	Min	1.3	0.0001	1
S90	3n	24.3	0.008	$3x10^{-5}$	1.9	1	0.12	'upwind'	Max	Min	1	0.0001	1
S91	3l	24.3	0.008	0.01	1.9	1	0.12	'central'	Max	Min	1	0.0001	2
S92	3l	24.3	0.008	0.01	1.9	1	0.12	'central'	Max	Min	1.1	0.0001	2
S93	3l	24.3	0.008	0.01	1.9	1	0.12	'central'	Max	Min	1.2	0.0001	2
S94	3l	24.3	0.008	0.01	1.9	1	0.12	'central'	Max	Min	1.3	0.0001	2
S95	3l	24.3	0.008	0.01	1.9	1	0.12	'central'	Max	Min	1.4	0.0001	2
S96	3l	24.3	0.008	0.01	1.9	1	0.12	'central'	Max	Min	1.5	0.0001	2
S97	3l	24.3	0.008	0.01	1.9	1	0.12	'central'	Max	Min	1.6	0.0001	2
S98	3l	24.3	0.008	0.01	1.9	1	0.12	'central'	Max	Min	1.8	0.0001	2
S99	3l	24.3	0.008	0.01	1.9	1	0.12	'central'	Max	Min	0.7	0.0001	3
S100	3l	24.3	0.008	0.01	1.9	1	0.12	'central'	Max	Min	0.8	0.0001	3
S101	3l	24.3	0.008	0.01	1.9	1	0.12	'central'	Max	Min	0.9	0.0001	3
S102	3l	24.3	0.008	0.01	1.9	1	0.12	'central'	Max	Min	1	0.0001	3
S103	3l	24.3	0.008	0.01	1.9	1	0.12	'central'	Max	Min	1.1	0.0001	3
S104	3l	24.3	0.008	0.01	1.9	1	0.12	'central'	Max	Min	1.2	0.0001	3
S105	3l	24.3	0.008	0.01	1.9	1	0.12	'central'	Max	Min	1.3	0.0001	3
S106-S126	3n	10-19.5	0.011 -	0.01	1.9	1	0.12	'central'	Max	Min	8.5-10	0.0001	1

			0.02											
S127-S142	3n	14-17	0.012	-	0.01	1.9	1	0.12	'upwind'	Max	Min	8.5-10	0.0001	1
			0.014											
S143-S157	3n	12-17	0.012	-	0.005	1.9	1	0.12	'central'	Max	Min	8.5-10	0.0001	1
			0.017											
S143-S157	3n	10-17	0.012	-	0.001	1.9	1	0.12	'central'	Max	Min	8.5-10	0.0001	1
			0.02											
S143-S157	3n	10-14	0.012	-	$6x10^{-5}$	1.9	1	0.12	'central'	Max	Min	8.5-10	0.0001	1
			0.014											
S173	3n	24.3	0.008		0.01	1.9	1	0.12	'central'	Max	Min	7.5	0.0001	1
S174	3n	24.3	0.008		0.01	1.9	1	0.12	'central'	Max	Min	7.5	0.008	1

* HLES means that the viscosity is estimated with a Horizontal Large Eddy Simulation

** DPS is the procedure that sets the depth at the grid cell centre

*** DPU is the procedure that sets the depth at the grid cell face

Appendix D Visual observations of simulations

The following two simulations are described in this section:

- R1
- R3a

The characteristics of these simulations can be found in

RunID	Domain	β	Boundary conditions	k_s [m]	ν_H [m^2/s]	A_{sh} [-]	Morphological updating scheme	Initial bed
R1	2n	24.3	Q_P-WL	0.008	0.01	1.9	'upwind'	Flat
R3a	2n	24.3	**WL-WL**	0.008	0.01	1.9	'upwind'	Flat

Table D-1: Characteristics of simulation R1 and R3a, see Table C-3 in Appendix C for more information

D.1. Visual observation R1

The development of bars in R1 can be separated in three stages:

1. 0 h <t< 4 h: Bars (mainly first-mode bars) start to develop at the curvature discontinuities (entrance and exit of the bend), see Figure D-1. The scour hole upstream of the bend propagates slowly in the upstream direction, with a visually estimated propagation speed of 0.6 m/h. At the upstream boundary some higher-mode bars are developing and propagating in the downstream direction, see Figure D-2. The propagation speed of the bar front is about 9 m/h, whereas the migration speed of an individual bar is about 1.5 m/h. The bars in the front of the pattern are the most recently generated and therefore less developed, which results in a lower height.

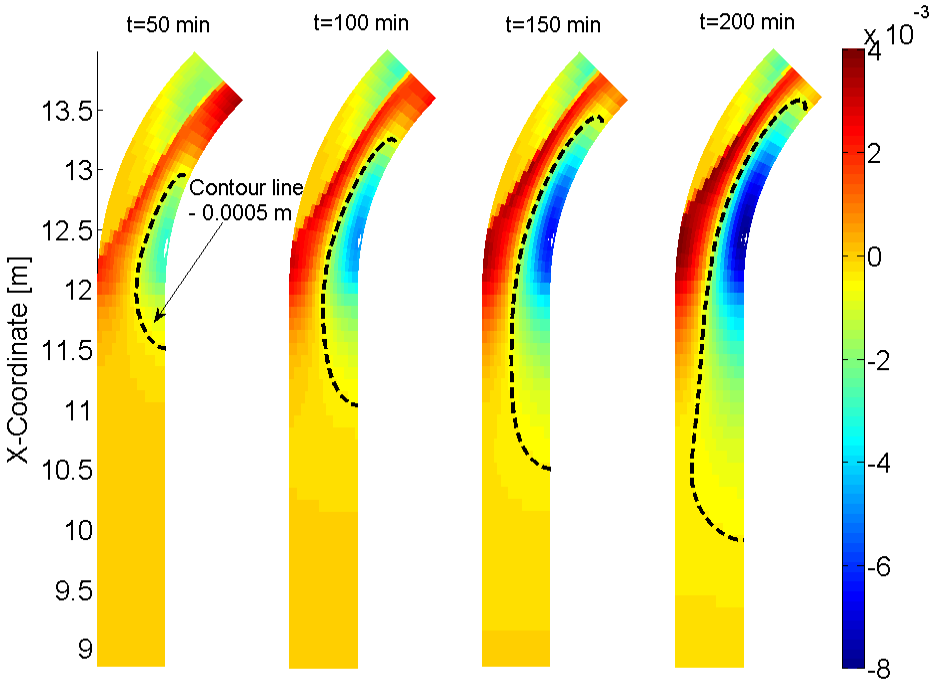

Figure D-1: Development of alternate bar at bend entrance in stage 1

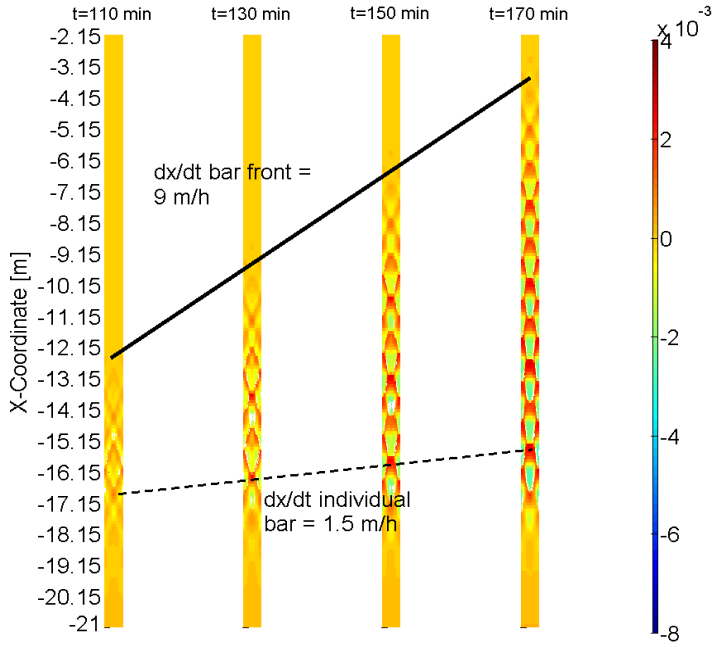

Figure D-2: Development of bar at upstream boundary

2. 4 h <t< 12.5 h: The higher-mode bars, caused by the upstream boundary, are reaching the entrance of the bend. The harmonic mode of the bars, upstream of the bend, start to decrease. At the end of the stage, over the entire straight reach alternate bars are present.

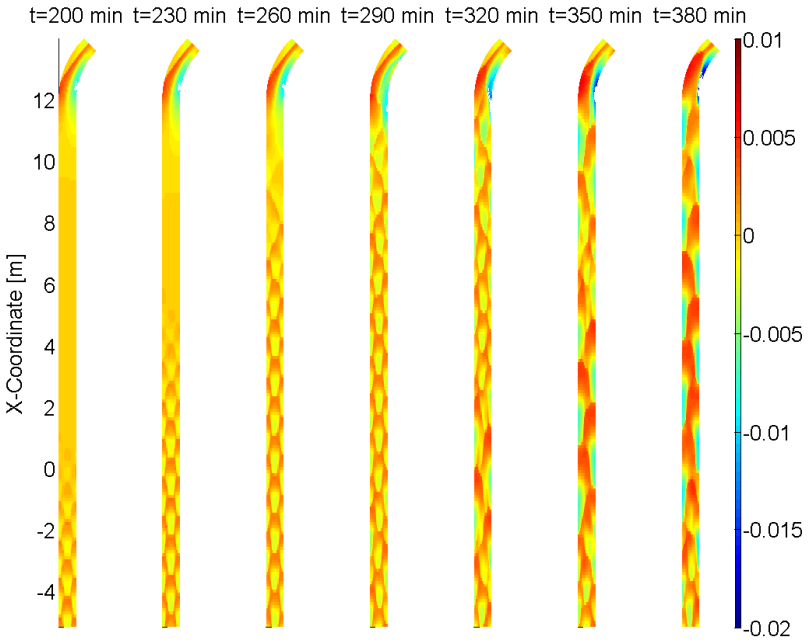

Figure D-3: Development of first-mode bars at entrance of the bend at stage 2

3. 12.5 h <t< 28.5 h: Both upstream and downstream alternate bars are present. At t=12.5 the most upstream alternate bar becomes dry. The top of the bar, therefore, has no interaction anymore with the flow and becomes non-migrating. Afterwards also the alternate bars downstream of this dried bar are dried, see Figure D-4.

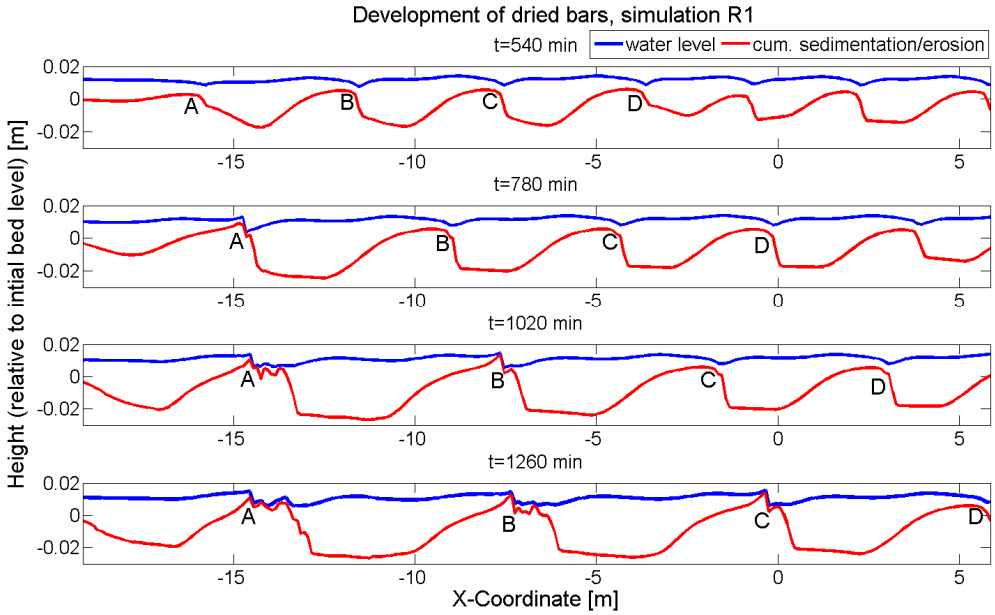

Figure D-4: Drying of alternate-bar peaks during stage 3

4. t>28.5 h: After about 28.5 hours of simulation the bed is in equilibrium. Still some small changes can be observed, but the bed is relatively steady.

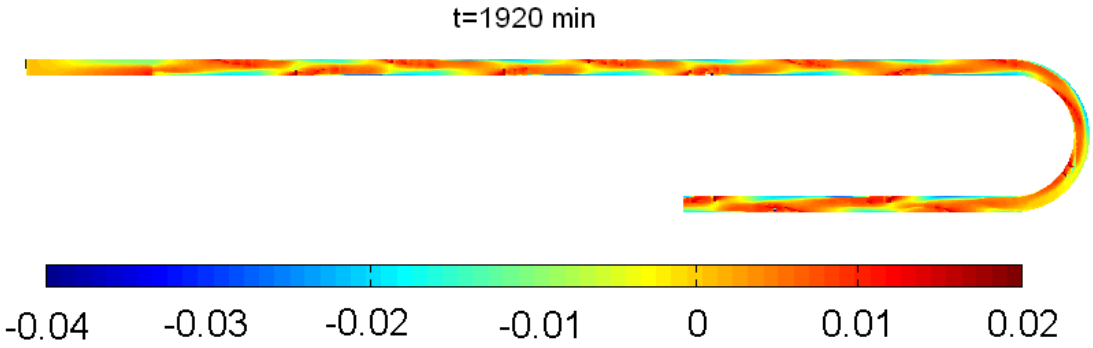

Figure D-5: Equilibrium alternate-bar pattern

D.2. Visual observations R3a

Also the development of bars in R3a can be separated in two stages (between brackets the period of the stage is stated):

1. 0 h <t< 12 h: In Figure D-6, one can see the development of the bed at the end of stage 1 and the beginning of stage 2. Like in Figure D-1, the area of influence propagates during stage 1 in the upstream direction (see the plots of t=550 min and t=650 min).

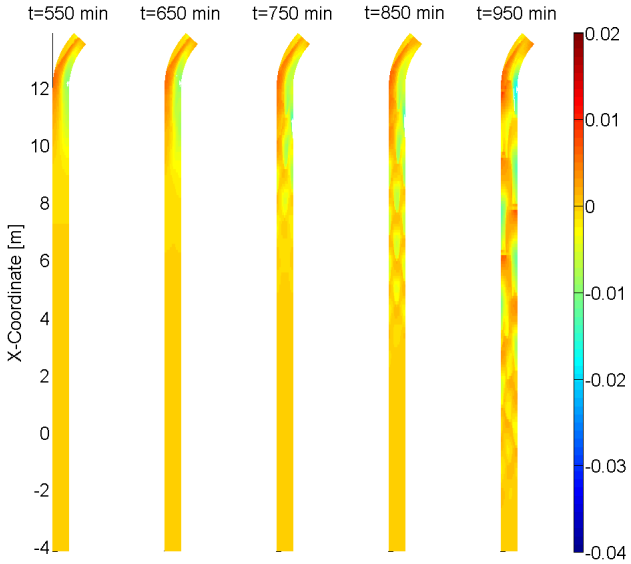

Figure D-6: Cum. sedimentation/erosion R3a stage 1

2. 12 h <t< 24 h: In Figure D-7, one can see that after 500 minutes of simulation (blue line) hardly any harmonics are present. At t= 600 min one can see the start of higher-mode bar development around X=13 m. The figure also shows that the higher-mode bars are not created by the upstream boundary (between X=2 m and X=6 m, no wiggle can be

seen). At t=700 min the higher-mode bars are also created more downstream of X=13 m.

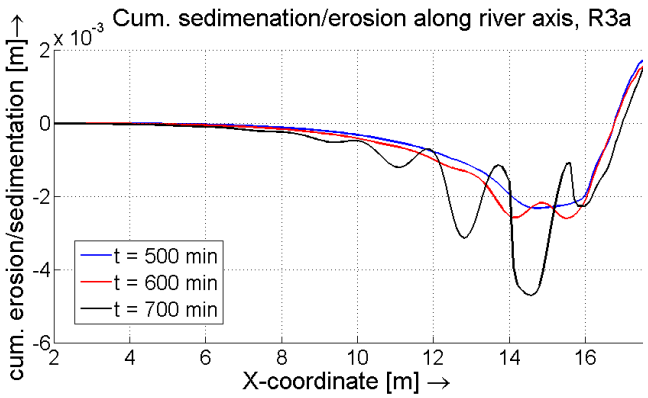

Figure D-7: Cum. sedimentation/erosion R3a at river axis (t = 500, 600 and 700 min)

Figure D-7 shows the development of alternate bars over time. At t = 700 min second-mode bars are present at the edge of the area of bend influence. After 1440 minutes of simulation, over the entire upstream reach, alternate bars have build up. The bars are still moving and increasing their amplitude and wave length. In Figure D-8, one can see that some bars are almost dried. At the moment that the water depth upon the bar is very low, the migration rate decreases. After a while the top of the bar is lowered again. This mechanism results in a strange and quite random alternate-bar pattern, in paragraph D.3 this mechanism is in detail investigated.

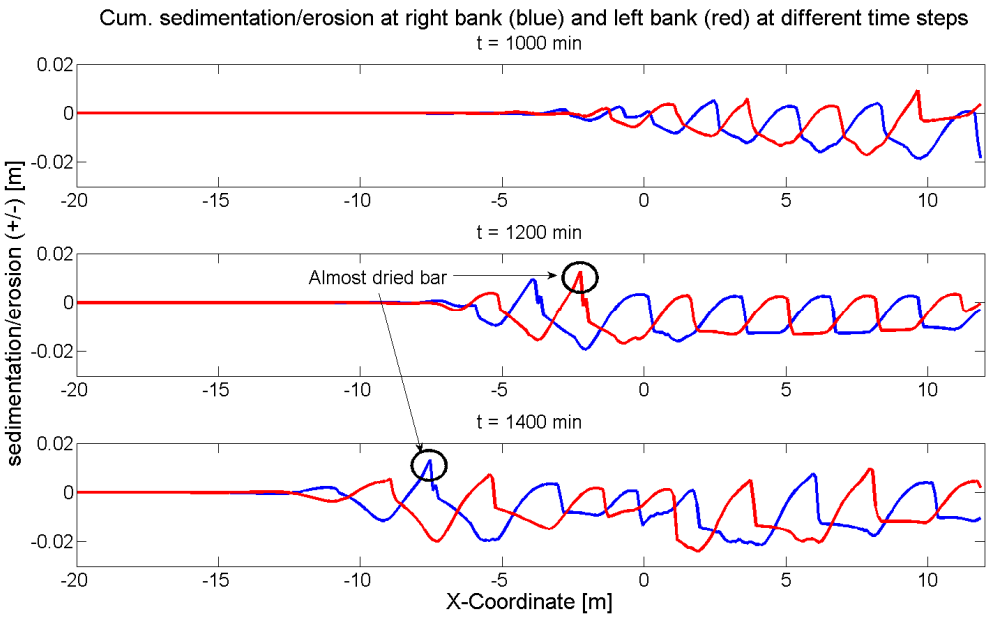

Figure D-8: Cum. Sedimentation/erosion at right and left bank at different time steps

D.3. Explanation of strange peaks R3a

The development of an alternate-bar peak is shown in detail in Figure D-9. It is shown that after 1111 min the alternate bar looks natural, see the upper subplot for the sedimentation/erosion plot. The maximum Froude number is 0.9 at that moment. About 20 minutes later (purple line), the Froude number has increased to 1. The bed-load transport decreased, so sedimentation took place. The top of the alternate bar is lifted in a short time. At t=1171 min the flow is unstable and the Froude number has increased to 1.2. The water depth under super-critical flow is below the critical depth, which can be seen in the fourth subplot of Figure D-9. Because of continuity, the velocity has increased and therefore also the bed-load transport. The increase of bed-load transport led to erosion at the alternate-bar top, which can be seen in the upper subplot. The red curve is only 1 minute after the blue one. In a short time, the sharp top is eroded again and the alternate bar has again a natural shape.

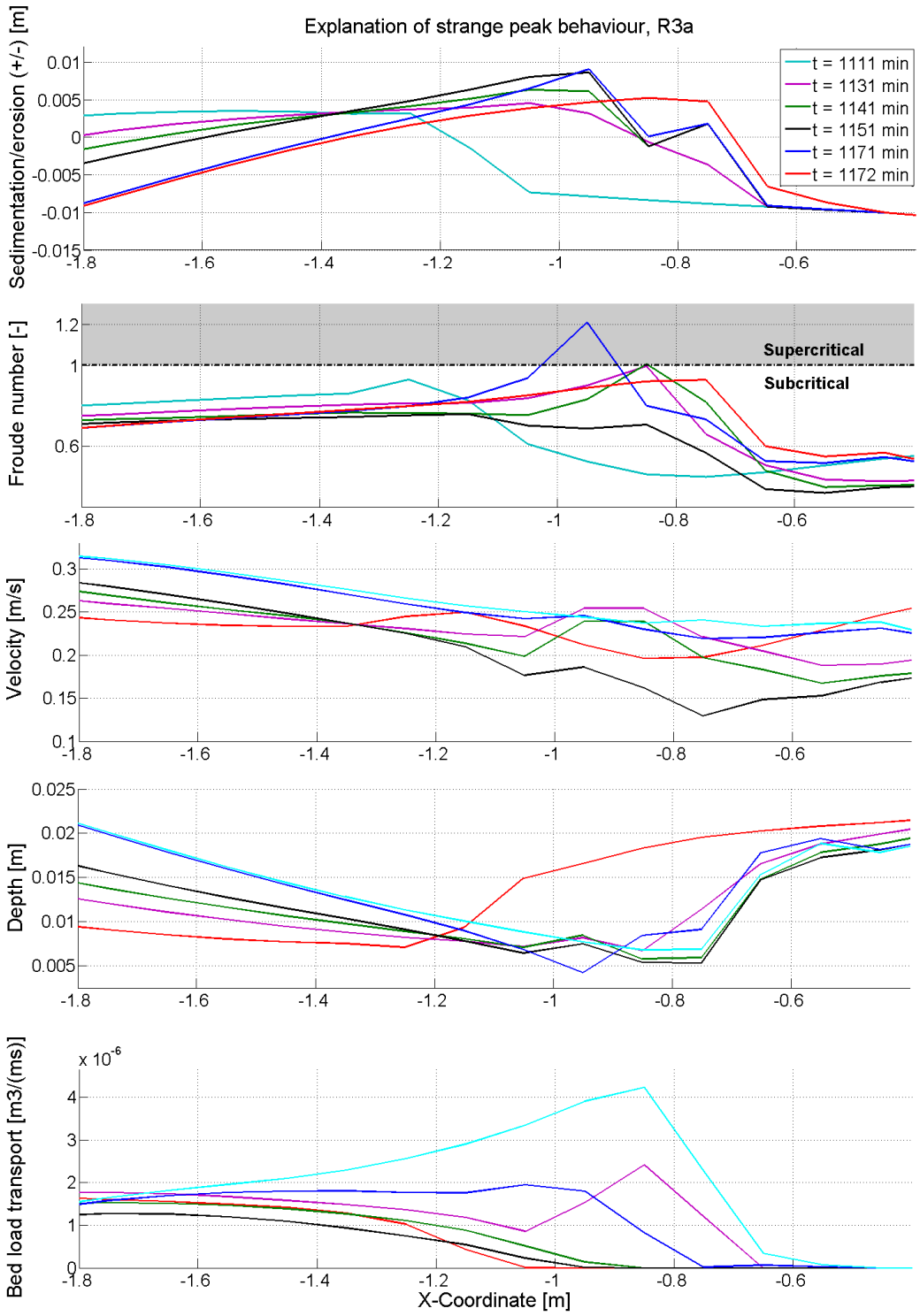

Figure D-9: Peak development in detail

Appendix E Fourier Transforms

In this appendix, the equations behind the Fourier transforms are briefly discussed. Also attention is paid to the accuracy of the Fourier analysis. Section E.2 explains the occurrence of wiggles in some plots of the "power" spectrum versus time.

E.1. Theory

The basic idea behind Fourier transforms is that any function can be represented by a summation of sine and cosine functions, with different resolution. This way of transforming is therefore very interesting for this research, because with this tool the harmonics, present in the bed level, can be found. Because the data to be analysed consists of a finite number of data points, the discrete variant of the Fourier transforms will be used in this research. First the transform in one dimension will be explained. Suppose that the data consists of a vector of N samples. The values at the data points are f(x). The transform is given by the following formula:

$$F(u)=\sum_{x=0}^{N-1} f(x)\cdot e^{\frac{-i2\pi u_f x}{N}} \qquad \text{(E-1)}$$

Or

$$F(u)=\sum_{x=0}^{N-1} f(x)\cdot\left(\cos\left(\frac{2\pi u_f x}{N}\right)-i\sin\left(\frac{2\pi u_f x}{N}\right)\right) \qquad \text{(E-2)}$$

In which u_f denotes the resolution variable. $F(u_f)$ usually contains complex numbers. The resolution, corresponding with a certain resolution variable, can be calculated as follows:

$$resolution(u)=\frac{u_f \cdot f_s}{U} \qquad \text{(E-3)}$$

Where f_s is the sample resolution. If for example every meter 5 data points are measured, then the sample resolution is 0.2. Capital U denotes the length of the vector u_f. In order to analyse $F(u_f)$, the following characteristics are relevant:

- Power spectrum: The "power" of the spectrum can be obtained by multiplying $F(u_f)$ with its conjugation. The "power" of a spectrum is a measure of the "energy" per harmonic component.
- Amplitude spectrum: The amplitude can be obtained by taking the absolute value of $F(u_f)$. This spectrum shows the amplitude of the harmonics which are present in the original signal.
- Phase spectrum: Because $F(u_f)$ consists of real and imaginary numbers, the phase of a certain component can be calculated as follows:

$$\text{Phase spectrum}\,(u_f) = \tan^{-1}\left(\frac{real(F(u_f))}{imaginary(F(u_f))}\right) \qquad \text{(E-4)}$$

$F(u_f)$, the "power" spectrum and the amplitude spectrum are always symmetric around the Nyquist resolution. This is the largest resolution, which can be found with the Fourier Transform. The Nyquist resolution is related to the sample frequency: fs/2. The lowest resolution which can be represented by Fourier analysis is equal to 1/(sample length). For this research special attention is paid to the first mode, which has a transverse wave length of two times the channel width. To be able to analyse this mode the bed level data is mirrored around the bank. To test how many times the transverse data has to be multiplied, the harmonic sin(2π/50*x) is analysed on a grid of 25*10 (x and y, respectively). If the data is not mirrored, the error with respect to the frequency output of the Fourier transform is in the order of 30%, see Figure E-1. If the transverse data is mirrored on such a way that the transverse length of the data is 8 times the original, the error is reduced to 0%. To get reliable results the bed level data for this research is mirrored on such a way that the analysed data has a length in the transverse direction which is 8 times the length of the original output of Delft3D.

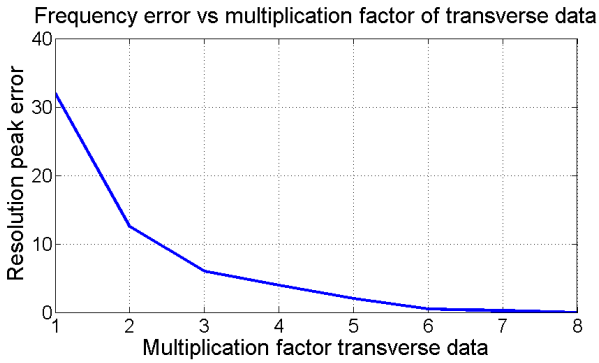

Figure E-1: Resolution error of first mode vs multiplication factor for transverse data

In two dimensions, which is needed for this research, the transform yields (given that the f(x,y) consists of M by N samples):

$$F(u,v)=\sum_{y=0}^{M-1}\sum_{x=0}^{N-1} f(x,y)\cdot e^{\frac{-i2\pi v_f y}{N}}\cdot e^{\frac{-i2\pi u_f x}{N}} \qquad \text{(E-5)}$$

In order to reduce computation time, the Fast Fourier Transform (FFT) algorithm is used. This algorithm uses a special kind of decomposition to reduce the calculations. The output of the FFT is the same as for other Fourier Transform logarithms.

E.2. Explanation of wiggles

In many plots of the "power" of a certain harmonic versus time, one can see that the curve includes some wiggles, see for example Figure 6-9 and Figure 6-10. The wiggles can be explained by the fact that the alternate bars are moving, whereas the sections are fixed. This will be shown for one example. Taken is the wiggle of the total "power" at section 1 during simulation R1 for 1400 min <t< 1550 min, see Figure 6-10.

In Figure E-2 the wiggles is shown in detail. At t = 1440 min the "power" has a local maximum. After that time, the "power" decreases, till it reaches a local minimum at t=1510 min.

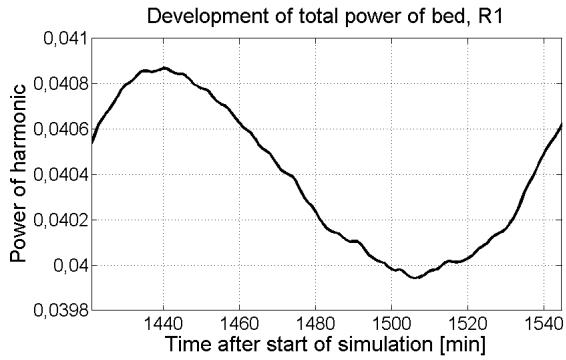

Figure E-2: Total "power" of bed in section 1, R1 1400 min < t < 1550 min

In Figure E-3, one can see the "power" of the bed, summed up in the transverse direction, for section 1 (boundaries are given by the black dotted lines). One can see that the "power" is not uniform in the longitudinal direction. Because the bars are migrating in this period, the "power" in section 1 is fluctuating. The total "power" of section 1 increases if the inflowing "power", at X = 8 m, is larger than the out flowing "power", at X=12 m. In Figure E-3, one can see that for t=1440 min, P_{in} and P_{out} are equal, which means, no increase or decrease of "power", as long as the internal production of "power" is zero. At t = 1475, 35 min later, P_{out} is larger than P_{in}, so the total "power" should decrease, if production is absent, etc.

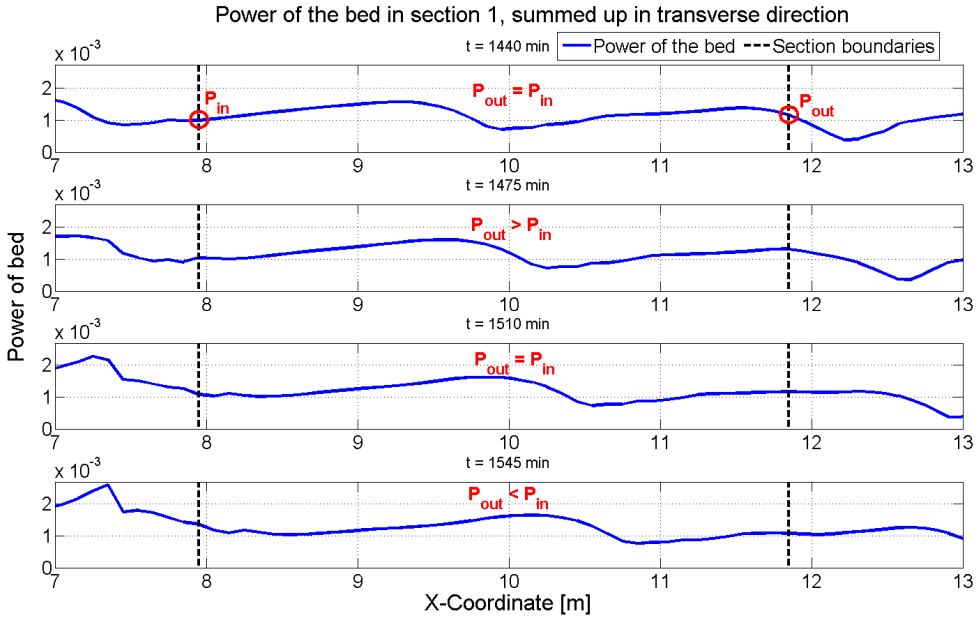

Figure E-3: Power of the bed (summed up in the transverse direction), R1

The import of "power" through the boundaries (P_{in} – P_{out}) is shown in Figure E-4. It can be clearly observed that the local maximum and minimum of Figure E-2 is corresponding with the time at

which the import of “power” switches sign. This reveals that the wiggle is mainly caused by differences in import of “power”, and not by internal production of “power”. So the wiggle is not the result of an amplification of the alternate-bar amplitude, but is a result of the fact that the bars are migrating. If the section length would be equal to the wave length of the alternate bars, or a multiple of it, no wiggles would occur.

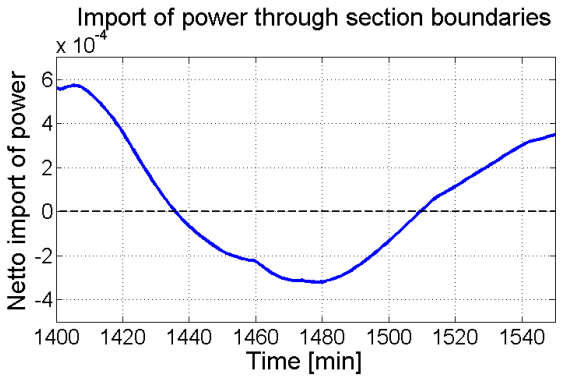

Figure E-4: Import of “power” through boundaries, R1, section 1

Appendix F Determining the point of resonance

The procedure to find the resonance point is illustrated in Figure F-1. Each data point (triangle, or square) represents a simulation with a specific discharge and initial alternate-bar wave length. The triangles show the observed direction of migration, the squares represent the simulations in which no migration was observed. The colour red means decay, whereas green means growth of the alternate bar. The lines in the figure are estimated, based on all the simulations. Subsequently the β_{res} can be found. In the case of a horizontal eddy viscosity of 0.01 m^2/s and the 'central' method for bed-load transport, the β_{res} is found to be 15.4.

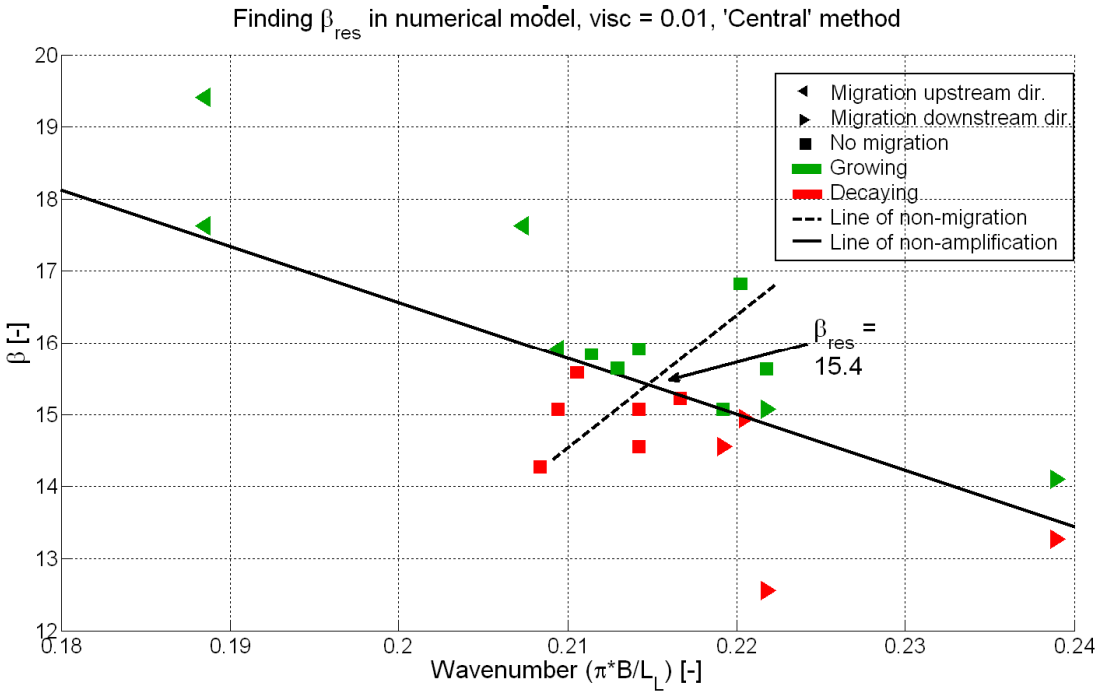

Figure F-1: Finding β_{res} with Delft3D, eddy viscosity = 0.01 m^2/s , 'central' method

The same procedure is used to find the resonance point in case of the 'upwind' method for bed-load transport, see Figure F-2. The β_{res} in this case is slightly lower (β_{res} = 15.1) than was the case with the 'central' method.

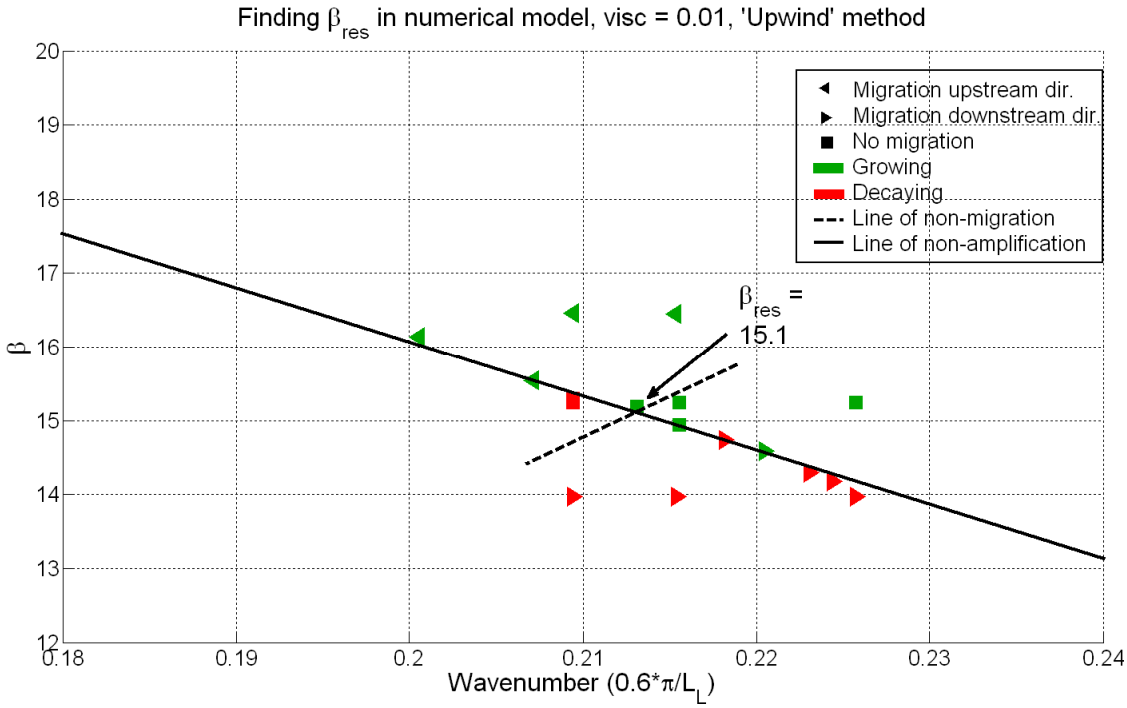

Figure F-2: Finding βres with Delft3D, eddy viscosity = 0.01 m2/s, 'upwind' method

Appendix G Numerical analysis

This appendix is an addition on chapter 5. First, the way numerical diffusion is introduced in the simulation will be explained (section G.1). Then the influence of the horizontal eddy viscosity on the amplification rate of small-amplitude bars, as observed in section 5.3.1, is explained.

G.1. Numerical diffusion

To calculate the hydrodynamic and morphodynamic variables, like water depth, flow velocity, bed-load transport, Delft3D uses a staggered grid, see Figure G-1. The model is divided in continuity cells. The water depth is defined in the centre of the continuity cells, the velocity is calculated at the call faces, and the depth is defined at the grid vertices. To explain the bed level updating procedure a flow in positive x-direction and y-direction is assumed.

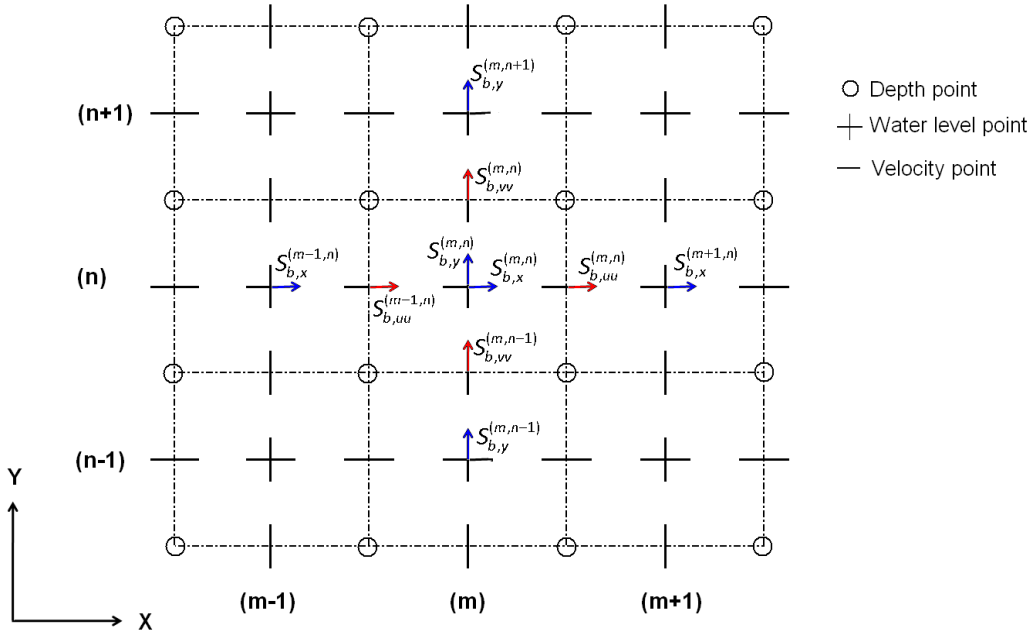

Figure G-1: Bed-load transport on staggered grid, red arrows at the cell face, blue arrows at the cell centre

At the end of each computational time step, the bed needs to be updated. This is done by computing the in- and output of sediment at the grid cell faces.

$$\Delta_{SED}^{(m,n)} = \frac{\Delta t \cdot f_{Morfac}}{A^{(m,n)}} \left(S_{b,uu}^{(m-1,n)} \Delta y^{(m-1,n)} - S_{b,uu}^{(m,n)} \Delta y^{(m,n)} + S_{b,vv}^{(m,n-1)} \Delta x^{(m,n-1)} - S_{b,vv}^{(m,n)} \Delta x^{(m,n)} \right) \quad \text{(G-1)}$$

To calculate the input of sediment at a grid cell face, the bed-load transport needs to be known at the grid cell face. In Delft3D, the bed-load transport is calculated at the grid cell centre, so an interpolation technique is needed. Two options are available: 'upwind' and 'central'. If the 'upwind'

procedure is used, the bed-load transport at the grid cell face is equal to the bed-load transport at the grid cell centre, immediately 'upwind' of the cell face:

$$S_{b,uu}^{(m,n)} = S_{b,x}^{(m,n)}$$
$$S_{b,vv}^{(m,n)} = S_{b,y}^{(m,n)} \qquad \textit{upwind procedure} \qquad \text{(G-2)}$$

If the 'central' procedure is used, the bed-load transport at the cell face is taken as the average of the bed-load transports at the 'upwind' and downwind cell centre:

$$S_{b,uu}^{(m,n)} = \frac{1}{2} S_{b,x}^{(m,n)} + \frac{1}{2} S_{b,x}^{(m+1,n)}$$
$$S_{b,vv}^{(m,n)} = \frac{1}{2} S_{b,y}^{(m,n+1)} + \frac{1}{2} S_{b,y}^{(m,n)} \qquad \textit{central procedure} \qquad \text{(G-3)}$$

The 'upwind' scheme introduces numerical diffusion. The numerical diffusion is necessary to be able to use an explicit time integration of the bed level updating procedure. The 'central' scheme is more accurate, but introduces oscillations, which can lead to instability.

The general effect of upwinding can be shown by looking at the bed-load transport distribution over a hand-made alternate-bar pattern, see Figure G-2. In the figure, one sees the bed level (right axis) and the bed-load transport for the simulation with the 'upwind' scheme (dotted line) and the 'central' scheme (solid line). The bed-load curve for the 'upwind' scheme is in front of the one for the 'central' scheme, the shift is in this case 0.05 m. This shift is dependent on the longitudinal grid size, and amounts dx/2.

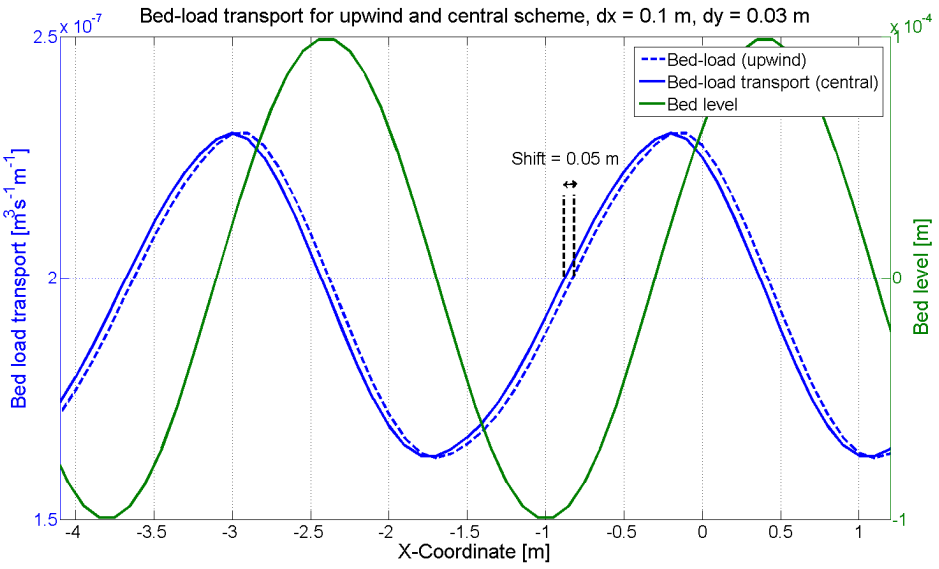

Figure G-2: Effect of upwinding

G.2. Influence of eddy viscosity on small-amplitude bars

The influence of the horizontal eddy viscosity on the behaviour of small-amplitude bars, as observed in section 5.3.1, can be considering the continuity equation for sediment.

Sediment transport can be seen as a function of the depth averaged velocity:

$$s = m \cdot u^b \qquad \text{(G-4)}$$

$$\frac{\partial s}{\partial x} = \frac{\partial}{\partial x}\left(m \cdot u^b\right) = m\frac{\partial (u^b)}{\partial x} \qquad \text{(G-5)}$$

$$b = \frac{3}{1 - \frac{0.047}{\psi}},\ \psi = \mu\theta \qquad \text{(G-6)}$$

In which m is a constant, and b is the degree of non-linearity. In this case (C = 21.75 $m^{1/2}/s$, u ≈ 0.2475 m/s, μ =0.7), b ≈ 7.5. So the sediment transport and therefore also ds/dx are strongly dependent on the depth averaged velocity.

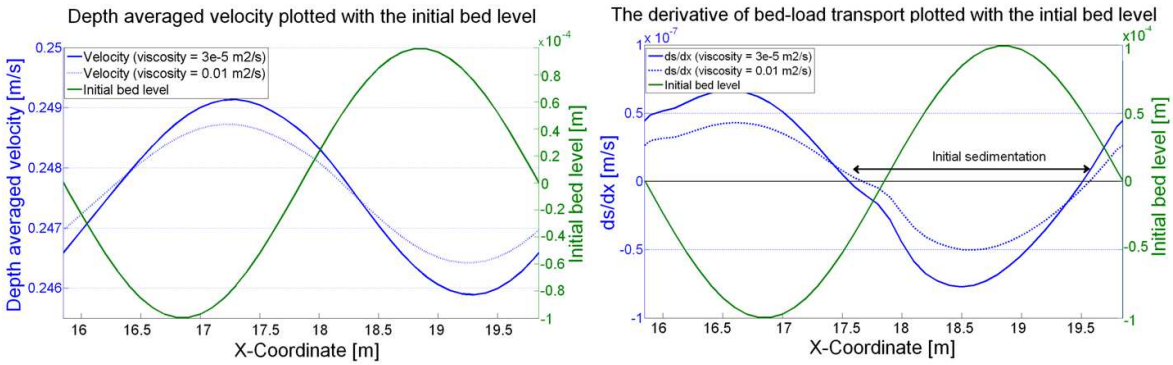

Figure G-3: Velocity (left) and bed-load transport derivative (right) distribution over an alternate bar for different values of v_H

If v_H is large, a certain perturbation will be smeared out over a larger area, as will be the case with a smaller value for v_H. So simulations with a lower v_H will have larger velocity perturbations, as can be seen in Figure G-3 (left). In the right part of the figure, one can see the distribution of ds/dx over the alternate bar. Sedimentation will occur if ds/dx is negative. One can see that for the simulation with v_H = 3e-5 m^2/s, ds/dx is more negative at the bar top as for v_H = 0.01 m^2/s, which results in a larger sedimentation/amplification rate for v_H = 3e-5 m^2/s.

Appendix H Development of bed topography spectrum

This appendix discusses the development of the bed level spectrum in the case of no boundary disturbance and in the case that the inflowing discharge is randomly perturbed.

The spectrum of a bed topography can be analysed with Fourier Transforms, see Appendix E. The development of the bed topography is analysed for two simulations: The first simulation (R1) has a perturbed upstream discharge input, the second simulation (R3a) has no upstream perturbation. For a visual description of both simulations one is referred to Appendix D.

H.1. Hypothesis

Linear theory represents the alternate-bar pattern solely with a first transverse mode. But in reality the alternate-bar mode does not have an exact first-mode shape, see Figure H-1.

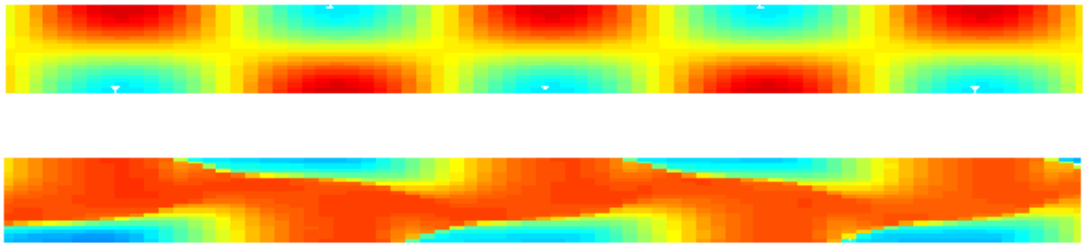

Figure H-1: First mode bar shape (top), versus a natural alternate-bar shape (down)

Many authors have analysed the equilibrium bed topography of alternate-bar patterns and discovered that all alternate-bar patterns roughly have the same composition. The fundamental harmonic is called the 1-1 harmonic mode, which means first mode in the longitudinal direction and first mode in the transverse direction. The wavelength, corresponding with the first mode in the longitudinal direction, is based on the peak in spectral analysis. Seminara and Tubino (1992) discovered that the fundamental harmonic represents about 15-30% of the total “energy” of the bed.

Apart from the fundamental harmonic, second-mode harmonics were also present in most alternate-bar patterns. This second-mode harmonic was observed by Zolezzi et al. (2005), Colombini and Tubino (1990), Seminara and Tubino (1992), and various other authors. Seminara and Tubino (1992) observed that the total “energy” of the second-mode harmonics in axial and the radial direction (2-2, 0-2, 2-0) is in the order of one third of the “energy” represented by the fundamental harmonic.

It is expected that the non-migrating bed topography matches the observations of the mentioned authors. The development of the composition is not investigated in detail before.

H.2. Composition in case of boundary disturbance

The main characteristics of the simulation, analysed in this section, can be found in Table H-1.

RunID	Domain	β	Boundary conditions	k_s [m]	ν_H [m^2/s]	A_{sh} [-]	Morphological updating scheme	Initial bed
R1	2n	24.3	Q_P-WL	0.008	0.01	1.9	'upwind'	Flat

Table H-1: Characteristics of simulation with boundary disturbance (R1) , see Table C-3 in Appendix C for more information

The development of the alternate-bar pattern in divided in four stages, a thorough description can be found in Appendix D. Here only a short description will be given:

- Stage 1: During this period no disturbance has reached the bend.
- Stage 2: This stage begins when the first disturbance reaches the bend.
- Stage 3: This stage begins when the first bar is dried and becomes non-migrating.
- Stage 4: This stage begins when at the entire upstream reach non-migrating alternate bars are present.

H.2.1. Development

In Figure H-2, one can see the development of "power" ("energy") of the harmonics in the bed in section 1.

Stage 1

During stage 1, no higher-mode disturbance reached the bend, so only a first and zero mode harmonic were present, see also Figure H-3. The zero mode harmonic can be explained by the fact that during stage 1 the bed upstream of the bend was in total lowered by the scour. The presence of the first-mode bar can be explained by the fact that at the outer part of the channel some accretion occurred, while at the right part of the channel the velocity was higher and therefore the bed was lowered by erosion.

Stage 2

The total "power" of the bed is quite constant during stage 2. It can be thought that before any bar top was dried, an equilibrium bed topography existed. Also the relative "power" of the harmonics was quite constant at the end of stage 2, see Figure H-3. The wiggles in the figures can be explained by the fact that the bars are still migrating, whereas the sections are spatially fixed. This is more explained in detail in Appendix E.

Stage 3

The increase of total "power" during stage 3 is probably related to the drying of bars, which are located more upstream. Later also bars downstream of the first dried bar became dry. Stage 3 also ends when the bar in section 1 is dried. Although the absolute "power" of the bed is increasing during stage 3, the relative "power" of the harmonic remains quite constant. The composition of the

alternate-bar pattern is in equilibrium, whereas the "power" of the alternate-bar pattern is not in equilibrium yet.

Stage 4

From that moment on that all alternate bars became dry, the bars became non-migrating, because there is no interaction between the bar top and the flow. This can be seen in both figures, the composition of the bed was also in equilibrium.

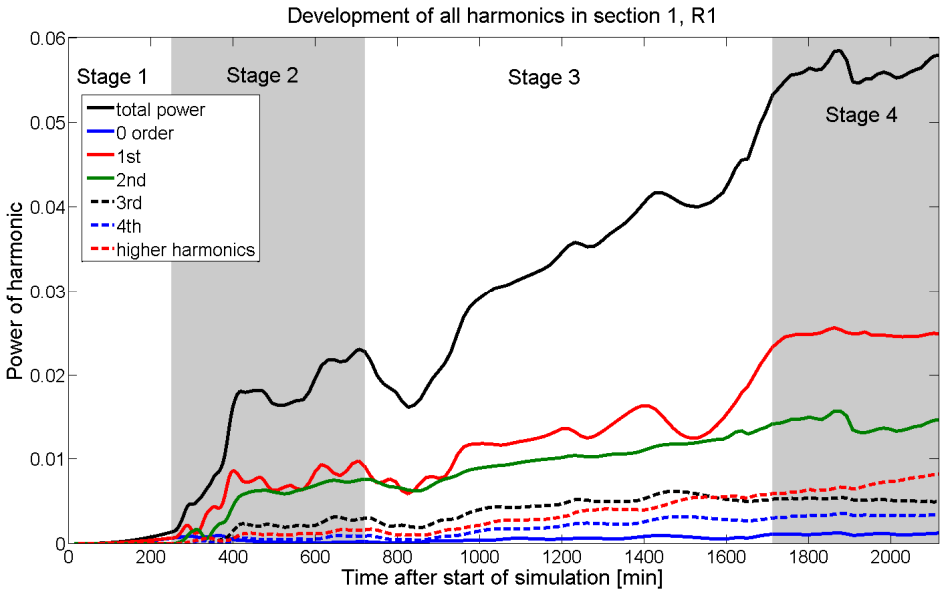

Figure H-2: Absolute "power" of harmonics in bed at section 1

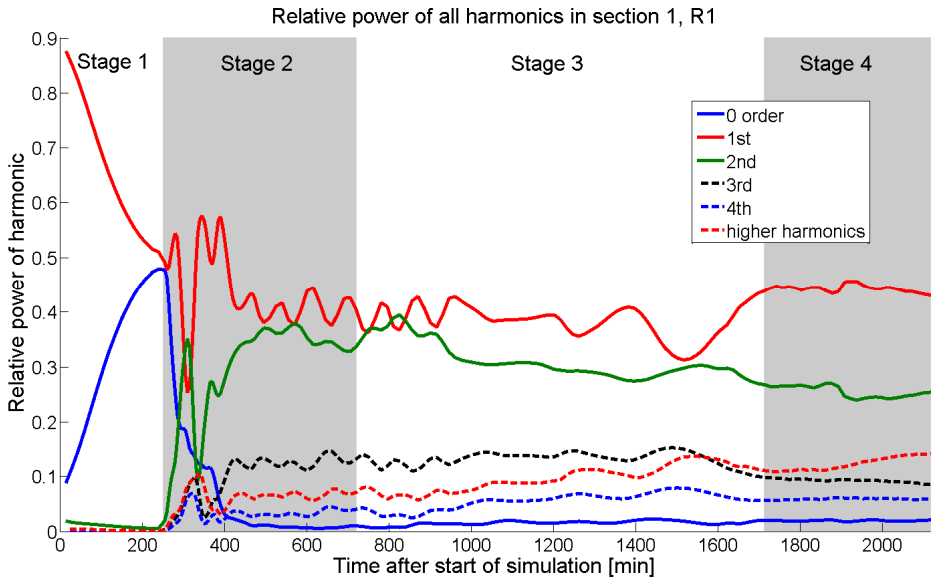

Figure H-3: Relative "power" of harmonics in bed at section 1

Explanation for second-mode harmonic

The second-mode harmonic, which has the second largest contribution in the "power" spectrum during stage 3 and 4, can be seen as a 'central' deposit. Bed material is transported from the side walls to the middle of the flume. This can be seen by longitudinally averaging the bed. This is done at t=2150 min for -4 m <X< 10.5 m, see Figure H-4. This section included exactly two alternate-bar wave lengths, so a valid averaging could be done. The calculated amplitude of the 0-2 harmonic (zero mode in longitudinal and second mode in the transverse direction), at t=2150, has a magnitude of 0.0095 m, which represents the curve in Figure H-4 very well. The difference between the top of the 'bell shape' and the lowest points near the walls is about 0.019 m, which is twice the computed amplitude of the 0-2 harmonic.

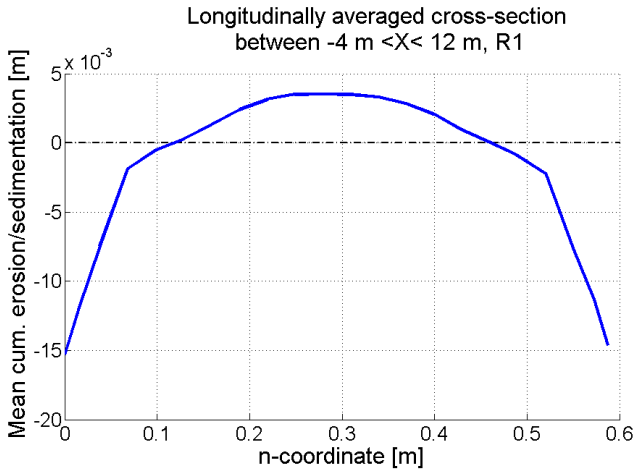

Figure H-4: Longitudinally averaged cross-section between -4 m <X< 12 m, R1

H.2.2. Equilibrium state

The sedimentation erosion data at t=35 hours is analysed with Fast Fourier Transforms. The maximum resolution in y direction, which can be analysed with Fourier analysis, is 5 m^{-1}. In x direction the maximum resolution is 16.6 m^{-1}. The largest part of the "energy" of the bed is related to low frequency harmonics. The "power" spectrum of the sedimentation erosion data is shown in Figure H-5. In this figure, only 1% of the entire frequency domain is taken into account, but it represents 75% of the entire "energy" in the sedimentation/erosion data. The figure shows that mainly three harmonics (represented by the peaks) are present in the bed. The characteristics of the main harmonic modes can be seen in Table H-2.

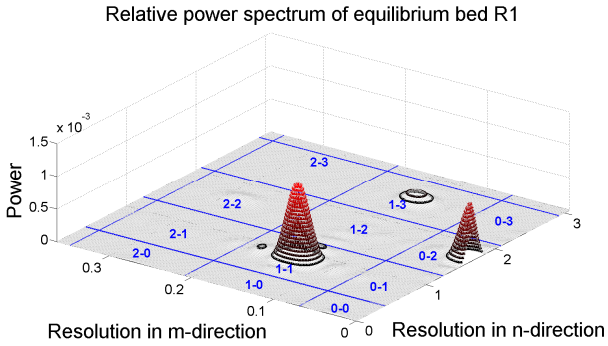

Harmonic	L_T * [m]	L_L [m]	h [mm]	Rel. "power" [%]
1-1	1.2	7.0	19.9	35
0-2	0.6	∞	9.8	14
1-3	0.4	7.0	8.8	5

Figure H-5: Power spectrum of bed level of Run 70, for t=35h;
Table H-2: Characteristics of the three main peaks in R1, at t=144h

The peak of the 1-1 harmonic mode represents 35% of the total "power". This corresponds roughly with the observation of Seminara and Tubino (1992) in which they observed that usually 15-30% of the total "energy" corresponds with the ' fundamental' harmonic.

Contrary to Colombini and Tubino (1990), the 2-2 harmonic in R1 contained little "energy". The total "energy" of the 2-2, 0-2 and 2-0 harmonics is about 14%, which is about one-third of the fundamental harmonic "energy".

H.3. Composition without boundary disturbance

The main characteristics of the simulations, analysed in this section, can be found in Table H-3.To be able to make a simulation without boundary disturbance both an upstream and downstream water level boundary had to be used. If a Q-WL boundary would have been used, a perturbation would always be present at the inflow boundary. Later I discovered that this perturbation is caused by the fact that the DPS (depth at grid cell centre) was set at 'MAX' and the DPU (depth at grid cell face) at 'MEAN'. The consequence of this is that the first grid cell (just outside the computational domain) has the same bed level as the second grid cell (just inside the computational domain), so a uniform situation cannot be created. The simulation is continued till the moment that the backwater curve reached the upstream boundary (at t = 24 h). Then the upstream water level boundary was replaced by a discharge boundary (R3b), to find the equilibrium bed topography.

RunID	Domain	β	Boundary conditions	k_s [m]	ν_H [m^2/s]	A_{sh} [-]	Morphological updating scheme	Initial bed
R3a	2n	24.3	**WL-WL**	0.008	0.01	1.9	'upwind'	Flat
R3b	2n	24.3	**Q-WL**	0.008	0.01	1.9	'upwind'	**End R3a ***

Table H-3: Characteristics of simulations without boundary disturbance (R3a continued with R3b) , see Table C-3 in Appendix C for more information

The development of the alternate-bar pattern in R3a is divided in two stages, a thorough description can be found in 0. Here only a short description will be given:

- Stage 1: During this period a scour hole developed upstream of the bend. This hole propagates in the upstream direction.
- Stage 2: This stage starts when higher-mode bars were created at the upstream edge of the scour hole.

H.3.1. Development (R3a)

In Figure H-6, one can see the development of the principle harmonics in the bed level for section 1.

Stage 1

During stage 1 (t < 700 min) the "power" spectrum consists equally of zero and first-mode harmonics. This can be understood by the fact that a part of section 1 was still quite uniform in the transverse direction, whereas the part near the bend already had a distinct alternate-bar shape. The absolute "power" development and relative "power" development during this stage is comparable to stage 1 of the simulation with disturbance, see H.2.1.

Stage 2

At the beginning of stage 2, the second mode starts to grow significantly. Also higher-mode harmonics appear in the bed. After t = 1100 minutes, the relative "power" of all harmonics remains quite constant. The absolute "power" is still increasing in that period. So at the end of simulation R3a, the bed is not steady, but the composition is in equilibrium. The first and second-mode

harmonic both take 35% of the total "energy" into account, the third harmonic 15%, the fourth harmonic 5%, the zero mode harmonic 1% and the rest (9%) is related to higher harmonics.

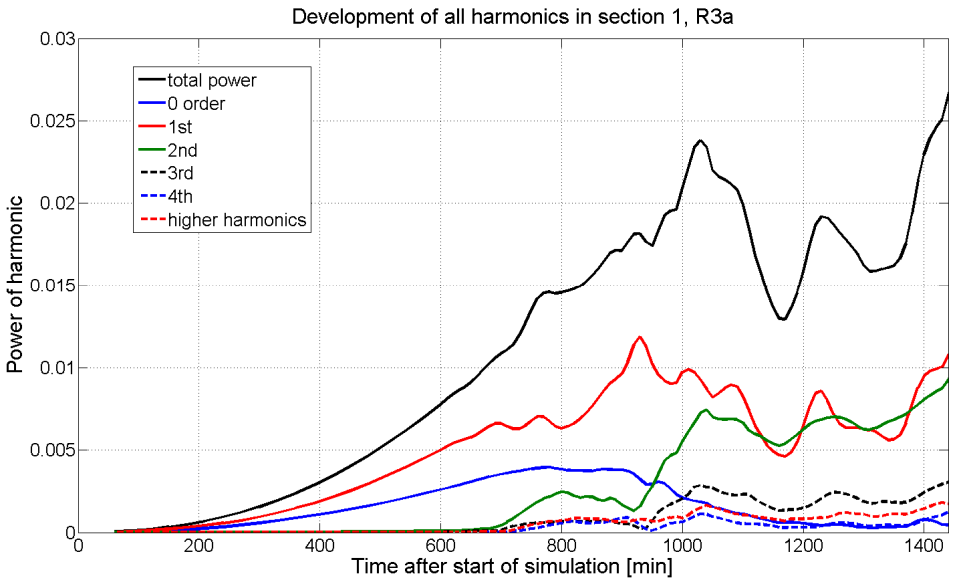

Figure H-6: Development of all harmonics in section 1

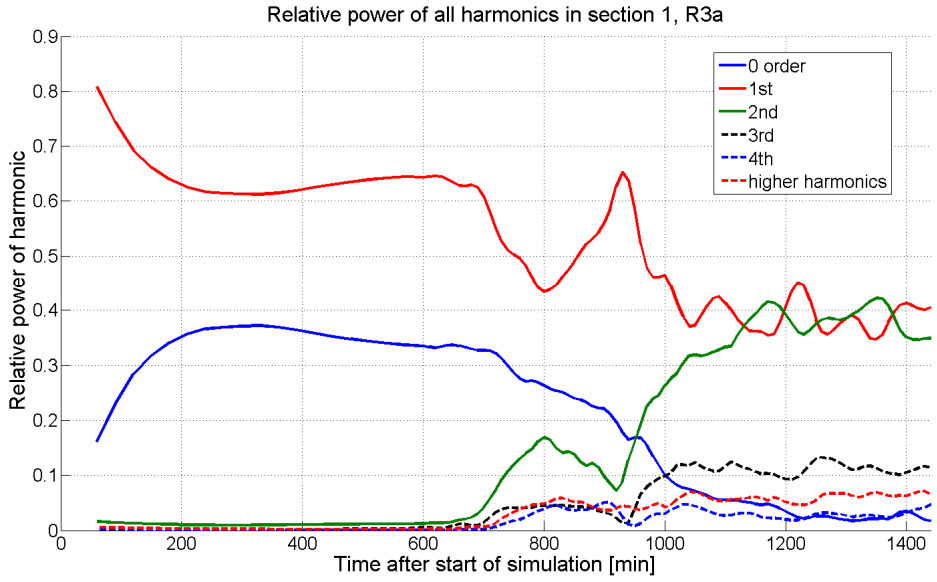

Figure H-7: Development of relative "power" harmonics

H.3.2. Equilibrium state

As explained in before, R3a is continued with an upstream discharge boundary after 24 hours of simulation (just before the backwater curve reached the upstream boundary). The equilibrium state of this simulation is briefly analysed.

The largest part of the "energy" of the bed is related to low resolution harmonics. The "power" spectrum of the sedimentation erosion data is shown in Figure H-8. In this figure, only 1% of the entire resolution domain is taken into account, but it represents 76% of the entire "energy" in the sedimentation/erosion data. The figure shows that mainly three harmonics (represented by the peaks) are present in the bed. The characteristics of these peaks can be seen in Table H-4.

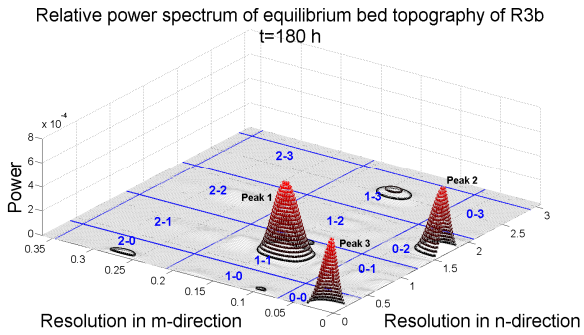

Harmonic	L_T* [m]	L_L [m]	h [mm]	Rel. "power" [%]
1-1	1.2	7.0	18.3	26
0-2	0.6	∞	8.6	13
0-0	∞	∞	5.1	9

Figure H-8: Power spectrum of bed level of R3b, for t=180 h, -14 m < X < 12 m
Table H-4: Characteristics of the three main peaks in R3b at t=180h

The "power" within the 1-1 section in Figure H-8 corresponds with this alternate-bar mode. Remarkable is the presence of a peak in the 0-0 area. This peak corresponds with a uniform deposit in both transverse and the longitudinal direction. From this peak it can be concluded that there has been a net nonzero sediment flux. This nonzero sediment flux occurred during simulation R3a, in which the incoming bed-load transport was larger than the bed-load transport at the downstream boundary, see Figure H-9.

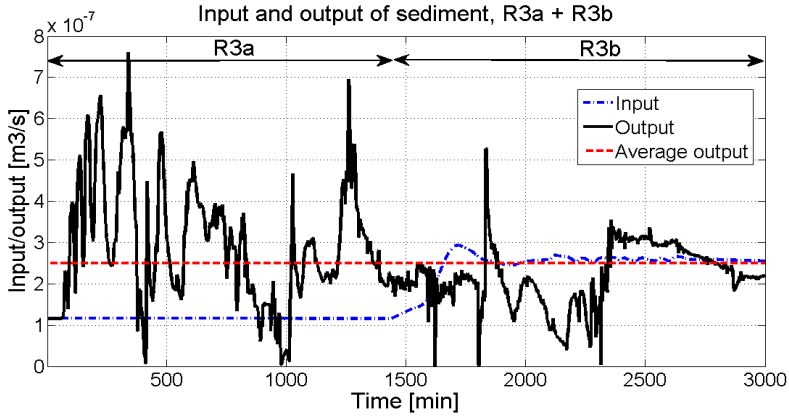

Figure H-9:Input and output of sediment, simulation R3a and R3b

H.4. Conclusions

The following conclusions can be drawn according to the development of the bed composition:

- The relative composition of the harmonics of the bed reaches equilibrium before the (absolute "power" of the) bed itself is in equilibrium
- In the simulations a temporary equilibrium was established before any bar was dried

- The alternate-bar mode mainly consists of a first-mode transverse bar (25 – 35% of the total “energy”) and a longitudinally uniform ‘central’ deposit (13-14 % of the total “energy”), like observed by Zolezzi et al. (2005), Colombini and Tubino (1990), Seminara and Tubino (1992), and various other authors.

Appendix I Development of wave length

This appendix discusses the development of wave length and the interaction between wave length and bar amplitude, for the simulation with boundary disturbance (R1). The main characteristics of the simulation, analysed in this section, can be found in Table I-1.

RunID	Domain	β	Boundary conditions	k_s [m]	v_H [m^2/s]	A_{sh} [-]	Morphological updating scheme	Initial bed
R1	2n	24.3	Q_P-WL	0.008	0.01	1.9	'upwind'	Flat

Table I-1: Characteristics of simulation with boundary disturbance (R1), see Table C-3 in Appendix C for more information

The development of the alternate-bar pattern in divided in four stages, a thorough description can be found in Appendix D. Here only a short description will be given:

- Stage 1: During this period no disturbance has reached the bend
- Stage 2: This stage begins when the first disturbance reaches the bend.
- Stage 3: This stage begins when the first bar is dried and becomes non-migrating.
- Stage 4: This stage begins when at the entire upstream reach non-migrating alternate bars are present.

I.1. Hypothesis

Fujita and Muramoto (1985) and Lanzoni (2000) observed during laboratory experiments that initially the wave length developed and then the amplitude of the alternate bar. This will be tested for the numerical simulation.

I.2. Development of wavelength

The peak of the "power" spectrum of the first-mode transverse harmonic is moving in time, see Figure I-1. These "power" spectra are made for the section -4 m <X< 12 m. The length of this section is 16m. The maximum observed wave length of the alternate-bar pattern is in the order of 7 m. The section is therefore more than twice the maximum observed wavelength. The possible error of wave length prediction is therefore less than 5%, see Figure E-1 in Appendix E. One can see that the wave length increase between t=500 min and t=700 min (stage 2) is quite low. The same can be seen for t=1700 min to t=2100 min (stage 4). For 1100 min < t <

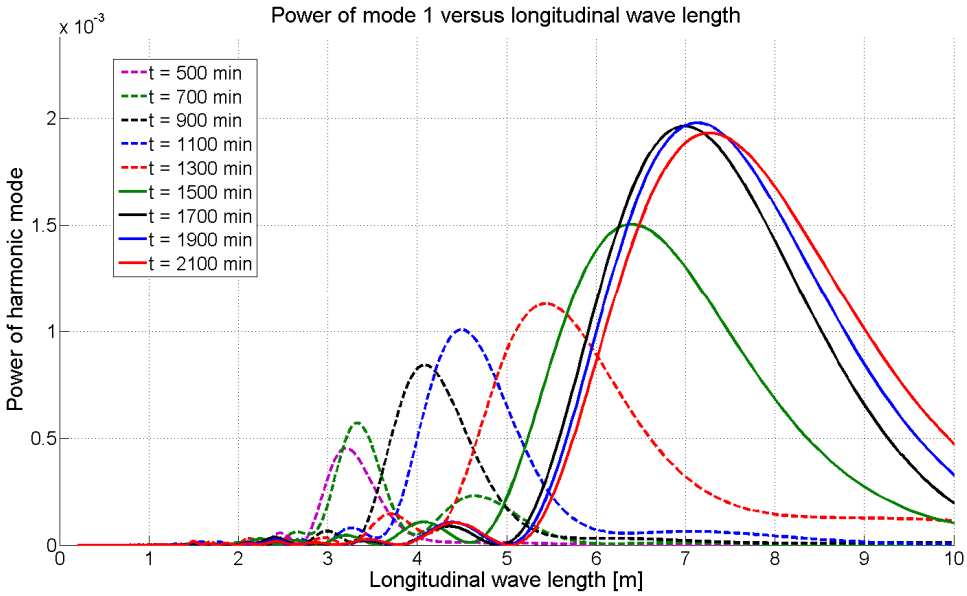

Figure I-1: Power spectra of first-mode harmonic for different times, R1, -4 m <X< 12 m

1700 min the peaks are moving quite a lot, the wave length increase is therefore high. The peaks of these spectra are corresponding with the main wave length for the first-mode transverse harmonic. The wave length, corresponding with the peaks, is plotted against time in Figure I-2. Before t=350 min no clear peak in the "power" spectrum was visible, therefore the data is extrapolated between t=0 min and t= 350 min (red dotted line). The wave length is indeed quite constant during stage 2. A temporary equilibrium solution is reached just before a bar was dried. This was also shown in Appendix H by conducting a spectral analysis of the bed.

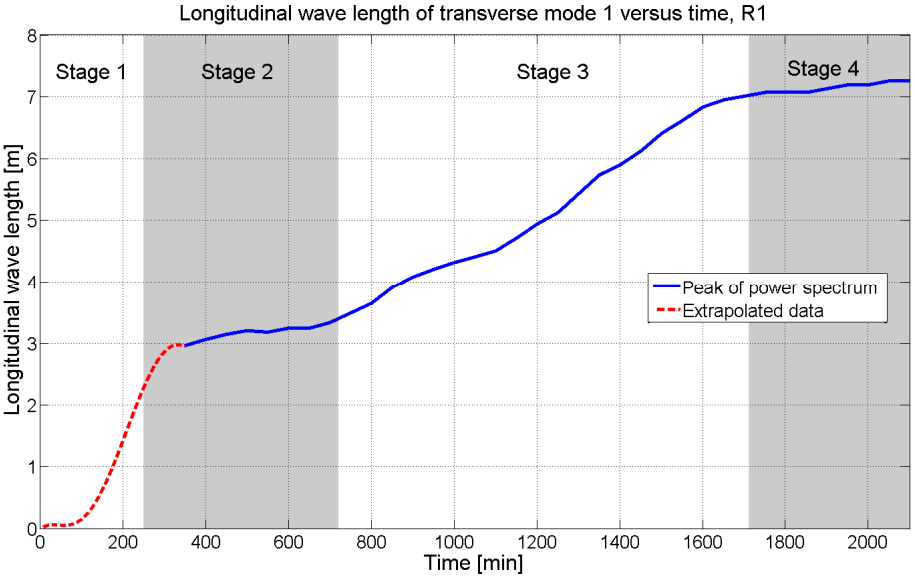

Figure I-2: Development of longitudinal wave length of first transverse mode, R1, -4 m <X< 12 m

The relative wave length development (L/L_{eq}) is plotted against the relative amplitude development (h/h_{eq}), see Figure I-3. In which the subscript 'eq' denotes the wave length or wave amplitude under

equilibrium conditions. The figure shows an upward concave relation between wave length development and wave amplitude development. When 60% of the wave length is already developed, only about 25% of the amplitude is developed. In the wave length development range of 60%-80%, the amplitude increases from 25%-90%. This complies with the observations of Fujita and Muramoto (1985) and Lanzoni (2000). In short, one can state that the bed first selects the wave length and then the amplitude.

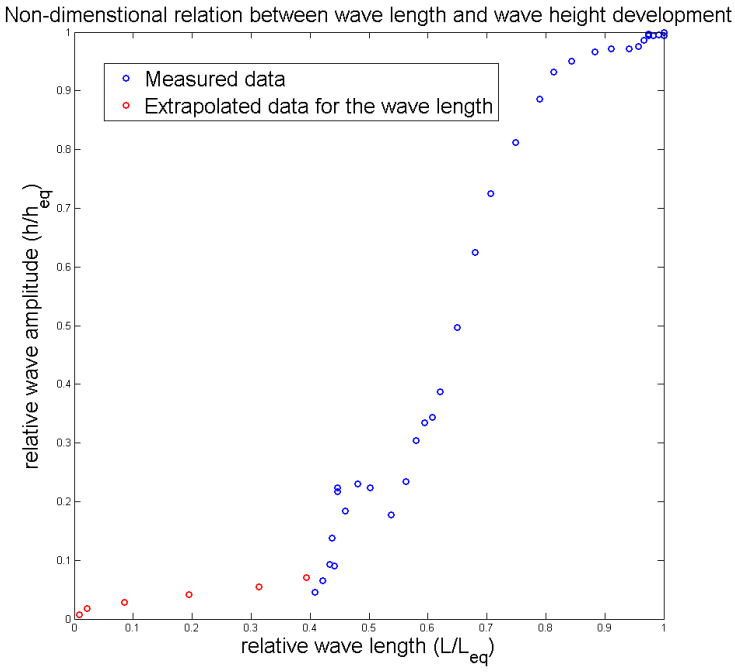

Figure I-3: Non-dimensional relation between wave length and wave height development

I.3. Conclusions

The following conclusions can be drawn according to the development of wave length and period:

- An equilibrium wave length is established before any alternate bar is dried.
- In agreement to the observations of Fujita and Muramoto (1985) and Lanzoni (2000), the bed first selects the wave length of the alternate-bar pattern and then the amplitude of the alternate-bar pattern.